VELOCITY-DEPENDENT DARK MATTER ANNIHILATION FROM SIMULATIONS, AND

3D MODELING OF THE INTERSTELLAR MEDIUM OF THE MILKY WAY

A Dissertation

by

ERIN NICOLE PICCIRILLO

Submitted to the Graduate and Professional School of
Texas A&M University
in partial fulfillment of the requirements for the degree of

DOCTOR OF PHILOSOPHY

Chair of Committee,	Louis Strigari
Committee Members,	Bhaskar Dutta
	Rupak Mahapatra
	Samiran Sinha
	James Harding
Head of Department,	Grigory Rogachev

May 2023

Major Subject: Physics

ABSTRACT

This dissertation is composed of two main research topics: velocity-dependent dark matter (DM) annihilation from simulations, and 3D modeling of the interstellar medium of the Milky Way (MW). The former has been my focus of research for the last four years, and has resulted in the three papers discussed in this dissertation. We have performed numerical calculations of $\mathcal{J}$-factors using hydrodynamical simulations of galaxies from the Auriga and APOSTLE simulations. My first project involves calculations of velocity-dependent line-of-sight $\mathcal{J}$-factors for the smooth DM halo component of MW-like galaxies. We also determine that the DM relative velocity distribution can be modeled using a Maxwell-Boltzmann distribution. My second project includes the velocity-dependent annihilation radiation from DM substructure, or subhalos, within the Auriga simulations. My third project focuses on the velocity-dependent DM annihilation from dwarf spheroidal (dSph) analogues within the APOSTLE simulations. In my fourth project, we are currently working to extend this research to examine the velocity-dependent $\mathcal{J}$-factors of the Andromeda galaxy (M31). We hope to compare these $\mathcal{J}$-factors to the extended γ-ray emission detected from M31. Another project that I am working on involves creating a 3D model of the interstellar radiation field (ISRF) of the MW. We plan for this model to include large-scale structures, such as spiral arms and the bar, as well as details of the stellar and dust distribution in the MW. My contribution to the project is a 3D completeness model of OB stars in *Gaia* DR3.

DEDICATION

I dedicate this dissertation to my children, who inspire me to improve myself every day.

ACKNOWLEDGMENTS

CONTRIBUTORS AND FUNDING SOURCES

Contributors

Funding Sources

NOMENCLATURE

DM	Dark Matter
DMO	Dark Matter Only
MW	Milky Way Galaxy
M31	Andromeda Galaxy
dSph	Dwarf Spheroidal
APOSTLE	A Project Of Simulating The Local Environment
EAGLE	Evolution and Assembly of GaLaxies and their Environments
Au#	Auriga Halo Number
AP-L#	APOSTLE Level 1 or 2
NFW	Navarro-Frenk-White Profile
MB	Maxwell-Boltzmann
GCE	Galactic Center Excess
ISM	Interstellar Medium
ISRF	Interstellar Radiation Field
CR	Cosmic Ray
OB	Type O and B Stars
Tycho-Gaia Astrometric Solution	TGAS
c	Speed of Light
G	Gravitational Constant
r, R	Radius
m, M	Mass
N	Number of particles or subhalos

V	Volume
ρ	Density
$\mathbf{x}$	Position Vector
$\mathbf{v}$	Velocity Vector
$f(\mathbf{x}, \mathbf{v})$	Phase-Space Function
P	Probability Distribution
$\mathcal{J}$	$\mathcal{J}$-factor
$\mathcal{J}_s$	Effective $\mathcal{J}$-factor
$\sigma_A v_{\mathrm{rel}}$	Annihilation Cross Section
μ_n	n-th Moment of the Relative Velocity Distribution
κ	Kurtosis
ϵ	Softening Length
L	Annihilation Luminosity
F	Annihilation Flux
V_{max}	Maximum Circular Velocity
R_{max}	Radius at which V_{max} Occurs

TABLE OF CONTENTS

ix

LIST OF FIGURES

LIST OF TABLES

1. INTRODUCTION AND LITERATURE REVIEW[*]

In this section I will provide an introduction to the material covered in this dissertation and discuss the background literature that pertains the MW, dSphs, M31, DM annihilation, simulations used in my research, and the interstellar medium.

1.1 The Milky Way

The MW is a barred spiral galaxy, in which our solar system is located about 8 kpc from the Galactic center. The total mass of the MW is estimated to be about $1.29 \times 10^{12} M_\odot$ [8], however much of the mass of the MW is composed of DM. The DM density at the Solar location is estimated to be about 0.35 GeV cm^{-3} [9]. Extended rotation curves of galaxies provide the most compelling evidence for the existence of large quantities of DM on galactic scales. Their detailed shapes provide invaluable insight regarding the spacial structure of the DM halo. Analytic calculations and simulations both suggest that the density profiles of DM halos may contain useful information regarding the cosmological parameters of the Universe. The DM halos of MW-like galaxies can be well approximated by a Navarro-Frenk-White (NFW) density profile [10]. The distribution of DM throughout the MW provides our motivation to examine MW-like galaxies in DM simulations.

1.2 dSph Galaxies

A dSph galaxy is a small galaxy with very little dust and an older stellar population. They are spheroidal in shape and can be found in the Local Group as companion galaxies to the MW and M31. There are 9 dSphs that we consider to use in our search for analogues in the simulated galaxies: Canes Venatici I, Carina, Draco, Fornax, Leo I, Leo II, Sculptor, Sextans, and Ursa Minor (see table 4.1).

dSphs have been found to be dominated by DM, and the typical stellar mass-to-light ratios for

---

dSph stellar populations are in the range $\sim 1 - 3$ [11]. The large presence of DM and proximity to the MW makes dSphs ideal candidates in which to study DM annihilation.

1.3 M31

The Andormeda galaxy (M31) is a barred spiral galaxy, and is the nearest large galaxy to the MW. Observational evidence for DM in M31 comes from measurements of its rotational velocity curve [12, 13]. These observations provide coarse-grained properties of the DM distribution near the central regions of the halo where the galaxy resides. With the existing data, the fine-grained structure of DM and its distribution outside of the galaxy is primarily inferred from simulated halos. Within the standard cosmological paradigm, M31's DM halo is expected to extend well beyond the galactic disk, and it is also expected to contain a large amount of substructure. Due to its mass and proximity, the detection sensitivity of M31 to DM searches with γ-rays is competitive with the MW dSph galaxies, particularly if the signal is sufficiently boosted by substructures. M31 is predicted to be the brightest extragalactic source of DM annihilation [14, 15], which motivates our study of DM annihilation radiation from M31.

1.4 DM annihilation

Indirect DM searches aim to identify Standard Model (SM) particles that are produced when DM particles annihilate with one another in astronomical environments. Electrons, neutrinos, and photons are stable SM particles that experiments are able to detect. The flux of SM particles from a system depends on the strength of the annihilation cross section, and the phase-space distribution of DM within the system. The astrophysical dependence of the annihilation rate is encapsulated in a quantity typically denoted in the literature as the $\mathcal{J}$-factor.

For DM particles with mass $\sim 10 - 1000$ GeV, the strongest bounds on the DM annihilation cross section have been obtained through observation of dwarf galaxies by gamma-ray observations such as the Fermi-LAT [16, 17, 18]. Combining the limits from all dwarf galaxies with high-quality stellar kinematic data, these bounds reach the cosmologically-motivated thermal relic cross section regime over this entire mass range. For higher values of the DM mass, $\gtrsim 1$ TeV, the leading bounds

come from observations of dwarf galaxies by H.E.S.S. [19] and HAWC [20]. Bounds over this entire mass range may also be obtained from the inner MW galaxy, though contamination from astrophysical sources make these bounds more difficult to interpret [21].

All these strong bounds on the DM annihilation cross section assume that the cross section is dominated by the velocity independent, s-wave component, and is therefore independent of velocity. If the annihilation cross section is velocity dependent, as in the cases of p-wave, d-wave, or Sommerfeld models, the $\mathcal{J}$-factor must account for this velocity dependence by incorporating the full DM velocity distribution [22, 23, 24, 25, 26, 27, 28, 29, 30, 31, 32, 33]. Cross section limits from dwarf spheroidal galaxies have been extended to these velocity-dependent models for the aforementioned annihilation channels [27, 31]. These constitute the most stringent limits on velocity-dependent models. In addition to these bounds from dwarf galaxies, there have been initial explorations of the impact of velocity-dependent DM annihilation on the signal from the Galactic center [26, 34], and from DM subhalos [6].

The above studies of velocity-dependent DM annihilation rely on simplified analytic models for the DM phase space distribution. While convenient because of their analytic properties, these simplified models need to be tested against the corresponding DM distribution of MW-like galaxies extracted from cosmological simulations of galaxy formation. We perform the first analysis of the $\mathcal{J}$-factor in velocity-dependent annihilation cross section models using state-of-the-art simulations of MW-like galaxies. For our study, we use the Auriga magneto-hydrodynamical simulations of galaxy formation [35], as well as the APOSTLE hydrodynamical simulations [36, 37]. We focus on the expected signal from the MW galaxy, for the first time determining the DM relative velocity distribution from cosmological simulations. From this distribution we determine the velocity-dependent $\mathcal{J}$-factors for p-wave, d-wave and Sommerfeld annihilation cross section models.

1.5 Simulations

In my research we utilize two different sets of hydrodynamical simulations from the Auriga [35] and the APOSTLE [38, 37] projects, which I discuss in this section.

The Auriga simulations [35] include a suite of thirty magneto-hydrodynamical zoom simula-

tions of isolated MW mass halos, selected from a 100^3 Mpc^3 periodic cube (L100N1504) from the EAGLE project [39, 40]. The simulations were performed using the moving-mesh code Arepo [41] and a galaxy formation subgrid model which includes star formation, feedback from supernovae and active galactic nuclei, metal-line cooling, and background UV/X-ray photoionisation radiation [35]. The cosmological parameters used for the simulations are from Planck-2015 [42] measurements: $\Omega_m = 0.307$, $\Omega_b = 0.048$, $H_0 = 67.77\,\mathrm{km\,s^{-1}\,Mpc^{-1}}$. In chapter 2 we use the standard resolution level (Level 4) of the simulations with DM particle mass, $m_{\mathrm{DM}} = 3 \times 10^5\,\mathrm{M_\odot}$, baryonic mass, $m_b = 5 \times 10^4\,\mathrm{M_\odot}$, and Plummer equivalent gravitational softening of $\epsilon = 370$ pc [43, 44]. In chapter 3 we use the high resolution level (Level 3) of the simulations with DM particle mass, $m_{\mathrm{DM}} = 5 \times 10^4\,\mathrm{M_\odot}$, baryonic mass, $m_b = 6 \times 10^3\,\mathrm{M_\odot}$, and Plummer equivalent gravitational softening length of $\epsilon = 184$ pc [43, 44].

The APOSTLE simulations [38, 37] use the same code as the EAGLE project [39, 40] with the EAGLE reference model Ref-L100N1504 calibration, applied to zoom simulations of Local Group analogue systems, which contain two MW-mass halos. The EAGLE simulations use a modified version of the P-GADGET3 Tree SPH code [45], the ANARCHY version of SPH [39, 46], and a galaxy formation subgrid model that includes metal-line cooling, photoionisation, star formation, and feedback from star formation and active galactic nuclei. The cosmological parameters are from WMAP-7: $\Omega_m = 0.272$, $\Omega_b = 0.0455$, $h = 0.704$. In chapter 2 we use twelve APOSTLE volumes simulated at similar resolution to EAGLE Recal-L025N0752, which we refer to as AP-L2 (i.e. Level 2 or medium resolution). At this resolution, the DM particle mass, $m_{\mathrm{DM}} \simeq 5.9 \times 10^5\,\mathrm{M_\odot}$, the initial gas particle mass, $m_g \simeq 1.3 \times 10^5\,\mathrm{M_\odot}$, and $\epsilon = 308$ pc. In chapter 4 and chapter 5, we use five APOSTLE volumes simulated at the highest resolution available, which we refer to AP-L1 (i.e. Level 1 or high resolution). In each of these five volumes, we choose one MW-like halo and one M31-like halo and select all of the self-bound substructures (subhalos) within the virial radius of the halos for further study. The DM particle mass at this resolution is $m_{\mathrm{DM}} \simeq 5 \times 10^4\,\mathrm{M_\odot}$, the initial gas particle mass is $m_g \simeq 1.0 \times 10^4\,\mathrm{M_\odot}$, and the maximum physical softening length is $\epsilon = 134$ pc.

All simulated halos have a dark-matter-only (DMO) counterpart which share the same initial conditions as the hydrodynamical runs, but galaxy formation processes are ignored and all the particles are treated as collisionless. I shall refer to halos in the hydrodynamical simulations as either the Auriga or APOSTLE halos and to those in the DMO simulations as DMO halos.

1.6 The Interstellar Medium

The interstellar medium (ISM) and the processes that occur within it are crucial in shaping the evolution of galaxies. The collapse of massive gas clouds composed of H_2 and heavier elements leads to the formation of stars. As stars evolve along the main sequence, the radiation they emit is absorbed and re-emitted by dust in the ISM, affecting the astrochemical distribution and balance between molecular, atomic, and ionized hydrogen. Supernova (SN) explosions at the final stage of evolution of massive stars accelerate cosmic rays (CRs), which in turn ionize the gas in the ISM and influence the galactic nucleosynthesis and star formation rate (SFR).

CR propagation in the ISM and the feedback effects with the other ISM components is a complex and fundamental problem in modern astrophysics. The CRs are subject to various energy losses due to their interactions with the other components of the diffuse ISM: the interstellar gas, radiation and magnetic fields. SN create turbulent magnetic fields, which affect the propagation and escape of CRs from a galaxy. CRs also generate turbulence and drive galactic winds, resulting in outflows of material enriching circumgalactic space. In the case of star-forming galaxies, the energy density in the radiation and magnetic fields, CRs, and turbulent motions of the interstellar gas are similar, so all of these components influence the others.

How all these pieces fit together to produce what we observe is still a mystery. Modern galaxy evolution simulations have included some of these processes [47, 48, 49, 50, 51, 52, 53, 54]. However, the simulations are calibrated to observations, e.g., the γ-ray luminosity vs. infrared (IR) luminosity/SFR relation in the MW and nearby galaxies [55], and are reliant on prescriptions for the sub-grid physics and assumed properties for the ISM. Without additional input on the ISM, the galaxy evolution modeling efforts are at an impasse on how to properly include CRs into the current frameworks.

2. VELOCITY-DEPENDENT $\mathcal{J}$-FACTORS FOR ANNIHILATION RADIATION FROM COSMOLOGICAL SIMULATIONS[*]

We determine the DM pair-wise relative velocity distribution in a set of MW-like halos in the Auriga and APOSTLE simulations. Focusing on the smooth halo component, the relative velocity distribution is well-described by a Maxwell-Boltzmann (MB) distribution over nearly all radii in the halo. We explore the implications for velocity-dependent DM annihilation, focusing on four models which scale as different powers of the relative velocity: Sommerfeld, s-wave, p-wave, and d-wave models.

2.1   Selection of MW-Like Galaxies

In this section we discuss our selection of MW-like galaxies. We select MW-like analogues from the Auriga and APOSTLE simulations using the following criteria: the virial mass, stellar mass, and rotational velocity curve [56, 57]. We obtain 10 Auriga level 3 halos and 6 APOSTLE level 2 halos.

Simulated *MW-like* galaxies are usually selected by their virial mass alone. However, to make accurate predictions for the DM distribution throughout the galaxy it is important to apply some additional criteria to select a MW analogue. Here, we specify the criteria we use for selecting MW analogues in the Auriga and APOSTLE simulations.

The Auriga halos have a virial mass of $M_{200} = [0.93 - 1.91] \times 10^{12} \, \mathrm{M_\odot}$ [35], which agrees with the observed MW halo mass estimates (see ref. [58] and references therein). We select the MW analogues by the following criteria introduced in refs. [56, 57]: (i) the stellar mass[1] of the simulated galaxy falls within the 3σ range of the observed MW stellar mass, $4.5 \times 10^{10} < M_*/\mathrm{M_\odot} < 8.3 \times 10^{10}$ [59], and (ii) the rotation curves of the simulated halos fit well the observed MW

---

[1]The stellar masses of both the Auriga and APOSTLE halos are calculated from the stars within a spherical radius of 30 kpc from the Galactic center.

rotation curve obtained from ref. [60]. As detailed in ref. [57], with these criteria we obtain a total of 10 MW-like Auriga halos. The virial and total stellar masses of these 10 Auriga halos are listed in table 2.1.

Halo Name	M_{200} $[\times 10^{12}\,\mathrm{M}_\odot]$	$M_\star$ $[\times 10^{10}\,\mathrm{M}_\odot]$
Au2	1.91	7.65
Au4	1.41	7.54
Au5	1.19	6.88
Au7	1.12	5.27
Au9	1.05	6.20
Au12	1.09	6.29
Au19	1.21	5.72
Au21	1.45	8.02
Au22	0.93	6.10
Au24	1.49	7.07
AP-V1-1-L2	1.64	4.88
AP-V6-1-L2	2.15	4.48
AP-S4-1-L2	1.47	4.23
AP-V4-1-L2	1.26	3.60
AP-V4-2-L2	1.25	3.20
AP-S6-1-L2	0.89	2.41

Table 2.1: The virial and stellar masses of the Auriga and APOSTLE MW-like halos, labeled by "Au-Halo Number" and "AP-Volume Number-Halo Number-Resolution Level", respectively. Reprinted with permission from ref. [2].

The AP-L2 simulations include an initial set of 24 MW-mass halos. Since the stellar masses of the halos in the APOSTLE simulations are slightly smaller than those expected for MW-mass halos [61], we slightly relax the criterion on the stellar mass to find the APOSTLE MW-like galaxies. In particular, we select the simulated galaxies with stellar mass in the range of $2.4 \times 10^{10} < M_*/\mathrm{M}_\odot < 8.3 \times 10^{10}$, and a rotation curve which agrees with the observed MW rotation curve [60]. With these criteria, we obtain a total of 6 MW-like AP-L2 halos. The virial and stellar masses of these halos are listed in table 2.1.

2.2 Properties of MW Analogues

In this section we discuss the properties of our sample of MW analogues, with a specific focus on the DM density profiles and the relative velocity distributions. Our determination of the DM relative velocity distribution is the first of its kind for MW analogues in cosmological simulations. Our analysis is also the first characterization of the DM velocity distribution at locations inside and outside of the Solar position. All prior studies have focused on the velocity distribution in the solar neighborhood and explored the implications for direct DM detection experiments [57, 56, 62, 63, 64].

2.2.1 DM Density Profiles

The predicted DM annihilation signal and the $\mathcal{J}$-factor are sensitive to the DM density profile, so it is important to understand the behavior of these profiles in our MW analogues. To determine the DM density profiles, we assume the halos to be spherically symmetric. This has been shown to be a good assumption for halos in hydrodynamic simulations [65], since baryons make the DM distribution more spherical in the central parts compared to the distribution obtained from DMO simulations [66, 67, 68, 69, 70].

The sphericity of the halos can be directly checked in our simulations. We compute the inertia tensor of the DM particles within four different radii: 2, 8, 20, and 50 kpc from the Galactic center, in Auriga and APOSTLE MW-like halos and their DMO counterparts. The sphericity is defined as $s = c/a$, where c and a are respectively the smallest and largest axes of the ellipsoid obtained from the inertia tensor. For a perfect sphere, $c = a$ and $s = 1$. We find that for the Auriga MW-like halos the sphericities at 2, 8, 20, and 50 kpc are in the range of $s(2 \text{ kpc}) = [0.66 - 0.89]$, $s(8 \text{ kpc}) = [0.72 - 0.86]$, $s(20 \text{ kpc}) = [0.71 - 0.88]$, and $s(50 \text{ kpc}) = [0.63 - 0.87]$, respectively. As expected, the sphericities are systematically lower for the DMO counterparts, in which $s(2 \text{ kpc}) = [0.63 - 0.88]$, $s(8 \text{ kpc}) = [0.58 - 0.80]$, $s(20 \text{ kpc}) = [0.56 - 0.69]$, and $s(50 \text{ kpc}) = [0.49 - 0.70]$. For the APOSTLE MW-like halos, we find $s(2 \text{ kpc}) = [0.80 - 0.90]$, $s(8 \text{ kpc}) = [0.69 - 0.88]$, $s(20 \text{ kpc}) = [0.73 - 0.85]$, and $s(50 \text{ kpc}) = [0.71 - 0.91]$, while for their

8

DMO counterparts, $s(2\,\mathrm{kpc}) = [0.75 - 0.79]$, $s(8\,\mathrm{kpc}) = [0.60 - 0.75]$, $s(20\,\mathrm{kpc}) = [0.54 - 0.75]$, and $s(50\,\mathrm{kpc}) = [0.53 - 0.78]$.

We extract the spherically-averaged DM density profiles from the mass enclosed in consecutive spherical shells of different widths from the Galactic center, containing 2,000 DM particles within each shell. Our choice of 2,000 DM particles per shell optimizes the calculation time of the $\mathcal{J}$-factors discussed in section 2.3. In order to calculate accurately the DM density profile, it is important to choose the location of the halo center carefully. We determine the center of each halo using the shrinking sphere method [43]. This is an iterative technique in which we start by calculating the center of mass of the DM particles within the virial radius, and then recursively shrink the radius of the sphere. At each step of the iteration the center of the halo is reset to the last computed barycenter and the radius of the sphere is reduced by 5%. This process continues until 1000 DM particles are contained within the sphere.

A second issue which is important in determining the DM density profile is the resolution limit. The thorough resolution study of ref. [43] suggests a convergence radius at which the integrated mass is converged within $\sim 10\%$, i.e. the so-called *Power radius*, R_{P03}, based on the two-body relaxation timescale of the DM particles. The criterion can be written as:

$$0.6 \leq \frac{\sqrt{200}}{8} \sqrt{\frac{4\pi\rho_{\mathrm{crit}}}{3m_{\mathrm{DM}}}} \frac{\sqrt{N}}{\ln N} R_{\mathrm{P03}}^{3/2}, \tag{2.1}$$

where N is the number of particles with mass m_{DM} enclosed within R_{P03}, and $\rho_{\mathrm{crit}} = 3H^2/8\pi G$ is the critical density [71]. For the cosmological parameters used in the simulations, we have $\rho_{\mathrm{crit}}(z = 0) = 127.49\ \mathrm{M_\odot\ kpc^{-3}}$ and $137.58\ \mathrm{M_\odot\ kpc^{-3}}$ for Auriga and APOSTLE simulations, respectively. Solving eq. (2.1) for each of the halos in the DMO simulations, we find the Power radius to be in the range of $R_{\mathrm{P03}} = [1.14 - 1.29]$ kpc and $R_{\mathrm{P03}} = [1.41 - 1.59]$ kpc for the Auriga and APOSTLE DMO simulations, respectively. The concept of numerical convergence is less clear in simulations containing baryons. For halos in the hydrodynamic simulations, we calculate the Power radius using only the DM particles and multiplying their mass by a factor of $\Omega_m/\Omega_{\mathrm{DM}}$,

9

which corresponds to a halo entirely made of DM particles. We find that the Power radius is in the range of $R_{\mathrm{P03}} = [0.94 - 1.07]$ kpc and $R_{\mathrm{P03}} = [1.33 - 1.45]$ kpc for Auriga and APOSTLE MW-like halos, respectively. The average Power radius is $R_{\mathrm{P03}} = 0.98$ kpc and 1.41 kpc for the 10 Auriga and 6 APOSTLE MW-like halos, respectively.

Using the methodology described above, figure 2.1 shows the DM density profiles for our MW analogues in the Auriga (left panel) and APOSTLE (right panel) simulations. As expected, at large radii, there is essentially complete agreement between the DM density profiles of the DMO and the hydrodynamic simulations. At small radii, inside the expected location of the Solar circle, the trend is for the halos in the hydrodynamic simulations to have steeper profiles compared to the DMO. This is a result of the contraction of the DM halo as a response to the presence of baryons in the inner parts of the halo [72, 73]. The steepening of the hydrodynamic profiles compared to their DMO counterparts is more pronounced for the Auriga halos compared to the APOSTLE halos. This is due to the smaller stellar masses of the APOSTLE halos, which leads to less contraction of the halos in APOSTLE compared to Auriga. For comparison, the best fit Navarro–Frenk–White (NFW) profile for the Auriga halo Au2 in the left panel and APOSTLE halo AP-V4-1-L2 in the right panel are shown as dashed black curves in figure 2.1.

2.2.2 Relative Velocity Distributions

We now determine the DM pair-wise velocity distributions, to which we refer in what follows as the DM relative velocity distributions. We begin by establishing our notation. Define $f(\mathbf{x}, \mathbf{v})$ such that $f(\mathbf{x}, \mathbf{v}) \, d^3\mathbf{x} \, d^3\mathbf{v}$ is the mass of DM particles within a phase space volume $\mathbf{x} + d^3\mathbf{x}$ and $\mathbf{v} + d^3\mathbf{v}$. The position vector $\mathbf{x}$ and the velocity vector $\mathbf{v}$ are defined in the rest frame of the galaxy. In these expressions and those below, bold-face quantities represent vectors with components given by the three spatial and velocity components of a DM particle. At a position $\mathbf{x}$ in the halo, we write the probability distribution of DM velocities as

$$P_{\mathbf{x}}(\mathbf{v}) = \frac{f(\mathbf{x}, \mathbf{v})}{\rho(\mathbf{x})}, \tag{2.2}$$

10
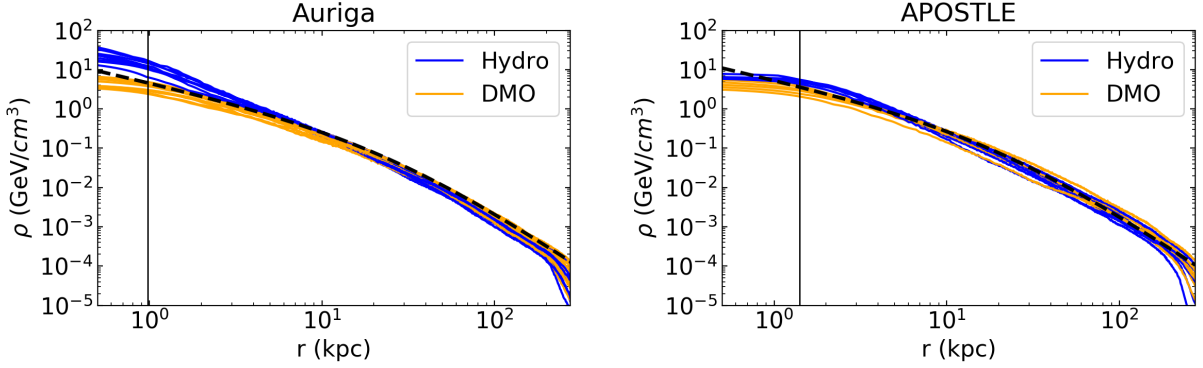
Figure 2.1: DM Density profiles for the Auriga (left panel) and APOSTLE (right panel) MW-like halos (blue) and their DMO counterparts (yellow). The dashed black curves specify the best fit NFW profile for Auriga halo Au2 in the left panel and APOSTLE halo AP-V4-1-L2 in the right panel. The vertical lines mark the average Power radius for the Auriga and APOSTLE MW-like halos in the left and right panels, respectively. Reprinted with permission from ref. [2].

where the DM density at $\mathbf{x}$ is normalized as

$$\rho(\mathbf{x}) = \int f(\mathbf{x}, \mathbf{v}) d^3 \mathbf{v}. \tag{2.3}$$

At a position $\mathbf{x}$, we are interested in the probability that a DM particle 1 has velocity $\mathbf{v}_1$ in the range $\mathbf{v}_1 + d^3 \mathbf{v}_1$ times the probability that a DM particle 2 has velocity $\mathbf{v}_2$ in the range $\mathbf{v}_2 + d^3 \mathbf{v}_2$,

$$P_\mathbf{x}(\mathbf{v}_1) d^3 \mathbf{v}_1 P_\mathbf{x}(\mathbf{v}_2) d^3 \mathbf{v}_2. \tag{2.4}$$

The individual particle velocities may be written in terms of the center-of-mass velocity, $\mathbf{v}_{\text{cm}}$, and the relative velocity, $\mathbf{v}_{\text{rel}} \equiv \mathbf{v}_2 - \mathbf{v}_1$, as $\mathbf{v}_1 = \mathbf{v}_{\text{cm}} + \mathbf{v}_{\text{rel}}/2$ and $\mathbf{v}_2 = \mathbf{v}_{\text{cm}} - \mathbf{v}_{\text{rel}}/2$. Using the fact that the magnitude of the jacobian of the transformation $d^3 \mathbf{v}_1 d^3 \mathbf{v}_2 \rightarrow d^3 \mathbf{v}_{\text{cm}} d^3 \mathbf{v}_{rel}$ is unity, and integrating over $\mathbf{v}_{\text{cm}}$, we then obtain a general expression for the distribution of relative velocities at a position $\mathbf{x}$,

$$P_\mathbf{x}(\mathbf{v}_{\text{rel}}) = \int P_\mathbf{x}(\mathbf{v}_1 = \mathbf{v}_{\text{cm}} + \mathbf{v}_{\text{rel}}/2) P_\mathbf{x}(\mathbf{v}_2 = \mathbf{v}_{\text{cm}} - \mathbf{v}_{\text{rel}}/2) \, d^3 \mathbf{v}_{\text{cm}}. \tag{2.5}$$

11

To calibrate our expectations, it is useful to review the prediction for the relative velocity distribution in the case of a pure Maxwellian halo. For Maxwellian halos, at any point in the halo, the DM velocity distribution, f, is Gaussian in all three velocity components, with a dispersion in each direction given by σ. The distribution of velocities is then given by the Standard Halo Model (SHM) [74], which is the simplest and most commonly adopted model to describe the DM halo. In the SHM, the DM halo is assumed to be spherical and isothermal, and this leads to an isotropic Maxwell-Boltzmann velocity distribution with a most probable speed of $\sqrt{2}\sigma$. In this case, the relative velocity distribution, $P_{\mathbf{x}}(\mathbf{v}_{\mathrm{rel}})$, is also a Maxwellian distribution, but with a one dimensional relative velocity dispersion of $\sqrt{2}\sigma$ [25].

The velocity vectors of the simulation particles are determined with respect to the center of each halo. In each spherical shell, we resolve the velocity vectors into three components then subtract the components of the velocities in this basis, being careful to avoid double counting. We then take the modulus of the components of the pairwise relative velocities, which provides an estimate of $P_{\mathbf{x}}(\mathbf{v}_{\mathrm{rel}})$ in each radial shell.

Notice that the relative velocity modulus distribution, $P_{\mathbf{x}}(|\mathbf{v}_{\mathrm{rel}}|)$, is related to the relative velocity distribution, $P_{\mathbf{x}}(\mathbf{v}_{\mathrm{rel}})$, by

$$P_{\mathbf{x}}(|\mathbf{v}_{\mathrm{rel}}|) = v_{\mathrm{rel}}^2 \int P_{\mathbf{x}}(\mathbf{v}_{\mathrm{rel}})\, d\Omega_{\mathbf{v}_{\mathrm{rel}}}, \tag{2.6}$$

where $d\Omega_{\mathbf{v}_{\mathrm{rel}}}$ is an infinitesimal solid angle along the direction $\mathbf{v}_{\mathrm{rel}}$. In each radial shell, $P_{\mathbf{x}}(|\mathbf{v}_{\mathrm{rel}}|)$ is normalized to unity, such that

$$\int P_{\mathbf{x}}(|\mathbf{v}_{\mathrm{rel}}|)\, dv_{\mathrm{rel}} = 1 \tag{2.7}$$

and therefore we have $\int P_{\mathbf{x}}(\mathbf{v}_{\mathrm{rel}})\, d^3\mathbf{v}_{\mathrm{rel}} = 1$.

In figure 2.2 we show the DM relative velocity modulus distribution in the Galactic rest frame for an example MW-like Auriga halo and its respective DMO counterpart. For both halos, we show the speed distributions in radial shells near the Galactic center, near the Solar circle, and at two radii well beyond the Solar circle (i.e. 20 and 50 kpc from the Galactic center). The solid blue
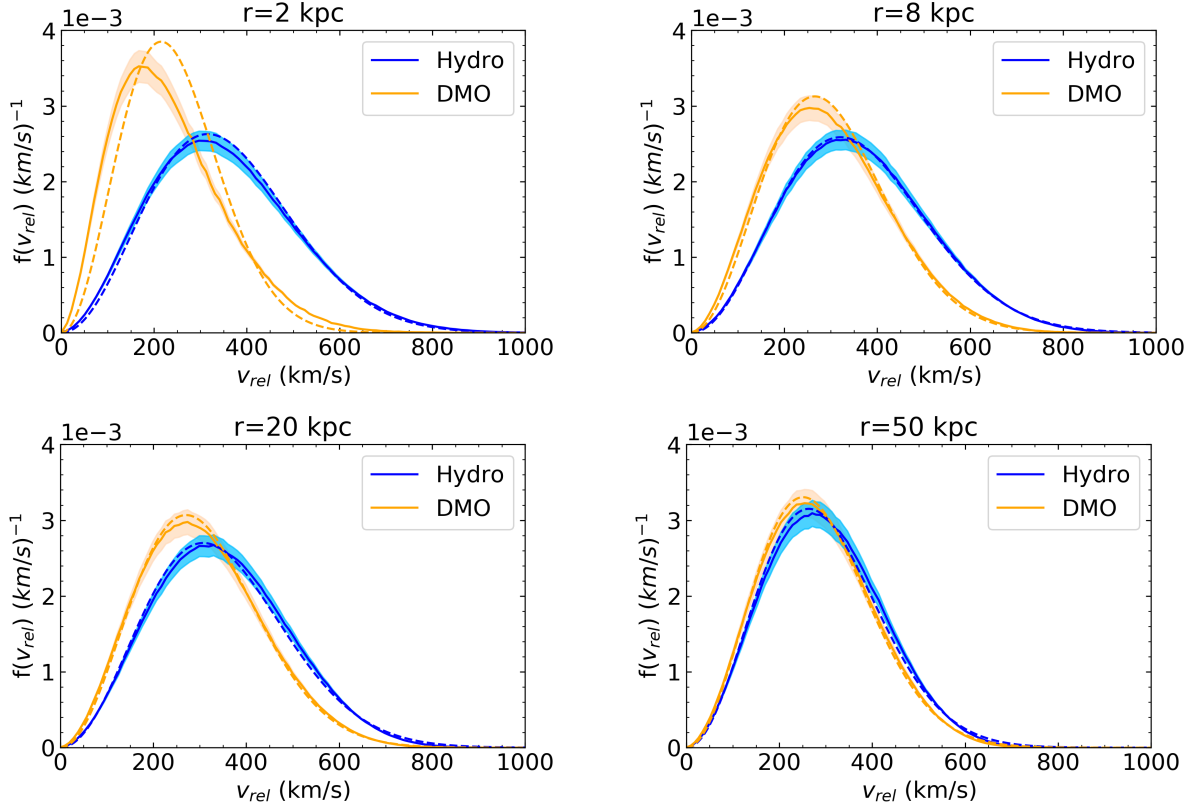
Figure 2.2: Modulus of the DM relative velocity distributions in the Galactic rest frame for an example Auriga MW-like halo (blue) and its DMO counterpart (yellow). Each panel shows the distributions at a different Galactocentric radius. The solid curves specify the mean relative speed distributions, while the shaded bands specify the 1σ Poisson errors. The dashed curves represent the corresponding best fit Maxwell-Boltzmann distribution. Reprinted with permission from ref. [2].

(orange) curves show the mean speed distribution for the Auriga (DMO) halo, while the shaded bands specify the 1σ Poisson error in the speed distributions.

The method used to define the spherical shells for calculating the density profiles produces varying radial boundaries from halo to halo. In order to effectively compare the relative velocity distributions of different halos at the same radius, we redefine the spherical shells to have fixed radial width progressing outward from the Galactic center. Each spherical shell has radial width of 0.1 kpc, with the number of particles in each shell in the range of $[486 - 3304]$. The spherical shells of fixed radial width are only used in the calculations shown in figures 2.2 and 2.4 (also see

figure B.1).

As we can see from figure 2.2, including baryons in the simulations results in an increase of the DM relative speed distributions at all radii. This increase is more pronounced in the inner galaxy, and is due to the deepening of the galaxy's gravitational potential when baryons are included in the simulations. This result is consistent with the local DM speed distributions of MW-like galaxies extracted from other hydrodynamic simulations [57, 62, 56, 63, 64].

Next, we compare the DM relative speed distributions at each radii with a Maxwellian distribution (dashed colored curves in figure 2.2). For each halo in the hydrodynamic and DMO simulations, we find the best fit Maxwellian speed distribution, $f(v) \propto v^2 \exp(-v^2/v_0^2)$, where v_0 is the best fit peak speed. For the halos in the hydrodynamic simulations, the relative speed distributions are very close to the Maxwellian model at all radii, with an agreement becoming increasingly better as we move further away from the Galactic center. For the DMO halos, the agreement with the Maxwellian model is not as good as is for the hydrodynamic case, though again the agreement gets better at radii further away from the Galactic center. Deviations from the Maxwellian distribution for the DMO halos at small radii are not surprising, since the DM density profiles deviate from the isothermal r^{-2} profile in the central regions of the DMO halos [75]. Additionally, the velocity anisotropy of the DMO halos at all radii leads to further deviations from the isotropic Maxwellian distribution.

In all cases, the DM relative speed distribution at small radii is shifted to smaller relative speeds as compared to the Maxwellian distributions, while at large radii there is a shift to larger relative speeds compared to the Maxwellian. We explore the origins of the shapes of these distributions in the following section. To understand how good the fit is to the Maxwell-Boltzmann distribution, in Appendix A we present the χ^2/dof for all halos at several different radii.

To explore the halo-to-halo variation in the DM relative speed distributions of the Auriga MW-like halos, we first examine their rotation curves. The circular velocities for two example Auriga halos (Au2 and Au22) are shown in figure 2.3. The total circular velocity of each halo is $v_c(r) = \sqrt{GM(<r)/r}$, where $M(< r)$ is the total mass (DM, stars, and gas) enclosed in a sphere of
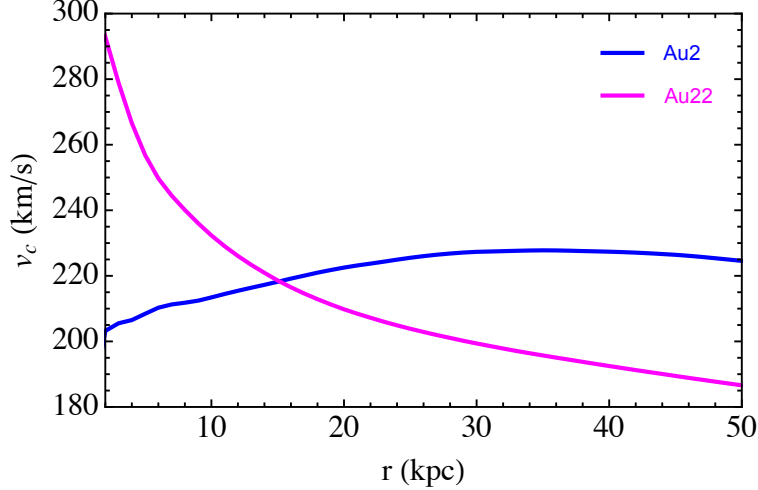
Figure 2.3: Circular velocity of the two Auriga halos Au2 (blue) and Au22 (magenta) as function of Galactocentric radius. Reprinted with permission from ref. [2].

Galactocentric radius r. In figure 2.4, we show the relative velocity modulus distributions for the same two halos. These halos have the smallest and largest peak speeds in the radial shell centered at 2 kpc. The four panels show the relative speed distributions of the two halos at different Galactocentric radii. As we move from 2 kpc to 50 kpc from the Galactic center, the relative speed distributions of Au22 is strongly shifted to smaller speeds, while that of Au2 does not show a significant change. This behavior can be understood from the rotation curves of the two halos, shown in figure 2.3. The circular velocity of Au2 changes slightly with Galactocentric distance, while that of Au22 decreases significantly as we move from 2 kpc to larger radii.

Notice that to extract the relative DM velocity distributions, we calculate the average distribution in each radial shell. We have verified the spherically average velocity distributions we obtained are consistent with those obtained by splitting each radial shell into 8 sections divided evenly about the azimuthal direction of the halo's principal axes. We have also checked our results against a more local method for computing the relative DM velocity distributions, using only the nearest neighbors of each particle. Choosing reasonable aperture sizes to find the neighbors of each particle in each radial shell, we find that the relative velocity distributions and $\mathcal{J}$-factors are not significantly affected. The difference in all the results of this dissertation when using this local
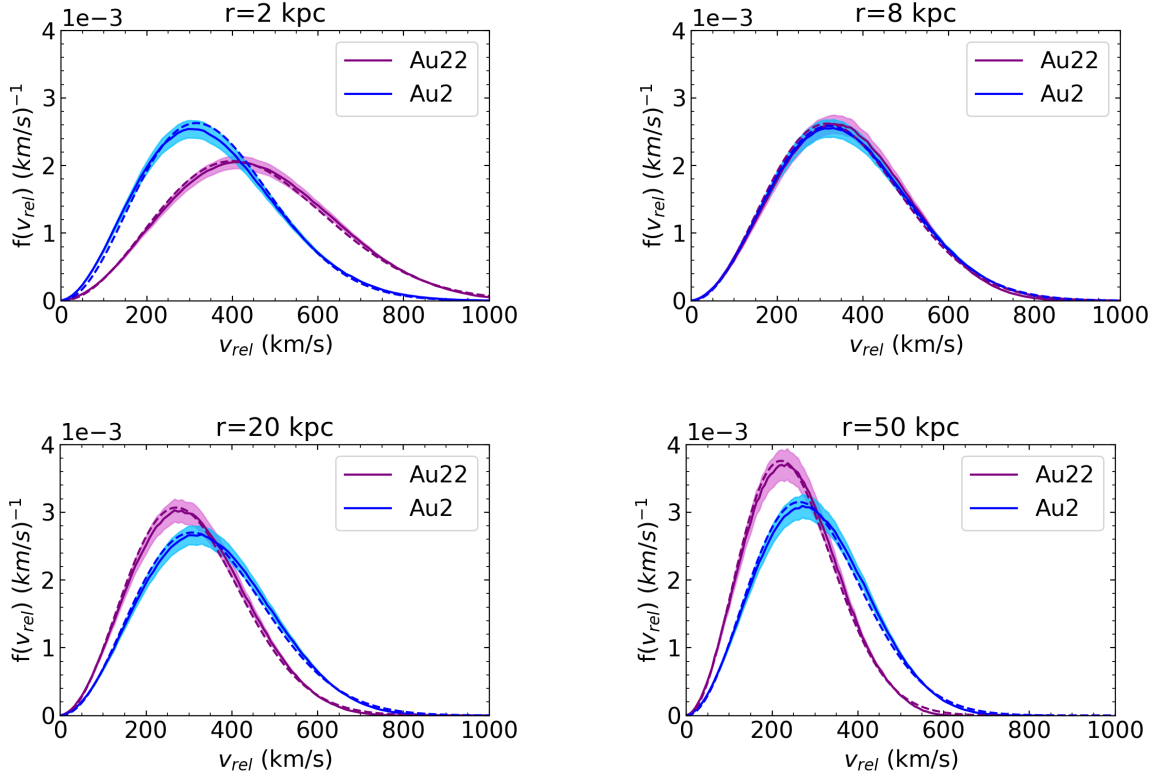
Figure 2.4: Modulus of the DM relative velocity distribution for the two Auriga MW-like halos that have the smallest (Au2, blue) and largest (Au22, magenta) peak speeds at 2 kpc. The modulus velocity distributions for the two halos are shown at the same radii as in figure 2.2. Reprinted with permission from ref. [2].

nearest neighbors method compared to using all particle pairs is at the order of $\sim 10\%$.

2.3 $\mathcal{J}$-factors

Having determined the DM density profiles and the relative velocity distributions for the MW-like halos, we are now in position to determine the velocity-dependent $\mathcal{J}$-factors. In this section, we lay out the formalism for calculating the $\mathcal{J}$-factors for each of the annihilation cross section models that we consider. In the formulae presented below, our notation closely follows that of ref. [25].

2.3.1 Annihilation Rate

We begin by defining σ_A, the DM annihilation cross section to any set of Standard Model particles. The number density of DM particles at position $\mathbf{x}$ is $\rho(\mathbf{x})/m$, where m is the DM particle mass. The flux of DM particles is given by the product of the number density and the modulus of the relative velocity, $v_{\text{rel}} \equiv |\mathbf{v}_{\text{rel}}| = |\mathbf{v}_1 - \mathbf{v}_2|$. Multiplying the flux by the DM annihilation cross section and the number density of target DM particles, we obtain the annihilation rate in a volume element dV at the position $\mathbf{x}$ in the halo as

$$\frac{d\Gamma}{dV} = \left[\frac{\rho(\mathbf{x})}{m}\right]^2 \int d^3\mathbf{v}_{\text{rel}} P_{\mathbf{x}}(\mathbf{v}_{\text{rel}})(\sigma_A v_{\text{rel}}). \tag{2.8}$$

We note that the standard definition of the annihilation cross section averaged over the relative velocity distribution is then,

$$\langle \sigma_A v_{\text{rel}} \rangle(\mathbf{x}) = \int d^3\mathbf{v}_{\text{rel}} P_{\mathbf{x}}(\mathbf{v}_{\text{rel}})(\sigma_A v_{\text{rel}}), \tag{2.9}$$

which in general depends on spatial location $\mathbf{x}$.

To determine the annihilation rate, as above we take the DM halo as spherically symmetric. We define a solid angle centered on the Galactic center, r as the distance from the Galactic center to a point in the halo, R_0 as the distance from the Sun to the Galactic center, ℓ as the distance from the Sun to a point in the halo (i.e. line of sight), and Ψ as the opening angle between the line of sight ℓ and the direction towards the Galactic center. The radial distance from the Galactic center to a point in the halo can then be expressed as $r^2(l, \Psi) = l^2 + R_0^2 - 2lR_0 \cos\Psi$. The annihilation rate along the line of sight is then proportional to

$$\mathcal{J}_s(\Psi) = \int d\ell \frac{\langle \sigma_A v_{\text{rel}} \rangle}{(\sigma_A v_{\text{rel}})_0} [\rho(r(\ell, \Psi))]^2. \tag{2.10}$$

which, following ref. [31], we define as the effective $\mathcal{J}$-factor. With this definition, the quantity $(\sigma_A v_{\text{rel}})_0$ is defined as the component of the annihilation cross section that is independent of the

17

relative velocity.

2.3.2 DM Annihilation Models

In the often-studied case in which $\sigma_A v_{\text{rel}}$ does not depend on the relative velocity, eq. (2.10) is simply proportional to the integral of the square of the density along the line-of-sight, $\mathcal{J} \propto \int \rho^2 d\ell$. More generally, $\sigma_A v_{\text{rel}}$ does depend on the relative velocity; in this case eq. (2.10) must be evaluated for the given velocity dependence.

To account for this velocity dependence, we will make the replacement relative to the above definition and parameterize the annihilation cross section in the general form, $\sigma_A v_{\text{rel}} \rightarrow \sigma_A v_{\text{rel}} = (\sigma_A v_{\text{rel}})_0 \, S \, (v_{\text{rel}}/c)$, with $S \equiv (v_{\text{rel}}/c)^n$. We examine the following possibilities: $n = -1$ (Sommerfeld-enhanced annihilation), $n = 0$ (s-wave annihilation), $n = 2$ (p-wave annihilation), and $n = 4$ (d-wave annihilation). These models may be realized for different assumptions for the nature of DM and the new physics that mediates their annihilation [31]. Examining these possibilities in the context of eq. (2.8), we see that the different cross section models correspond to different velocity moments of the relative velocity distribution,

$$\langle \sigma_A v_{\text{rel}} \rangle(\mathbf{x}) \propto \int \mathrm{d}^3 \mathbf{v}_{\text{rel}} P_{\mathbf{x}}(\mathbf{v}_{\text{rel}}) v_{\text{rel}}^n \equiv \mu_n(\mathbf{x}), \tag{2.11}$$

where μ_n is the n-th moment of the relative velocity distribution, $P_{\mathbf{x}}(\mathbf{v}_{\text{rel}})$. Examining eq. (2.11) we may then attach a physical meaning to the velocity-averaged annihilation cross section for each of the models. In the case of the s-wave, the annihilation rate is simply proportional to the DM density squared at a given position. For the case of Sommerfeld models, eq. (2.11) is proportional to the inverse moment of the relative velocity distribution, while for the s-wave, p-wave, and d-wave models, eq. (2.11) corresponds to the zeroth, 2nd, and 4th moments, respectively.

The effective $\mathcal{J}$-factor in eq. (2.10) can then be written as

$$
\begin{aligned}
\mathcal{J}_s(\Psi) &= \int d\ell \int d^3\mathbf{v}_{\mathrm{rel}} P_\mathbf{x}(\mathbf{v}_{\mathrm{rel}}) \left(\frac{v_{\mathrm{rel}}}{c}\right)^n [\rho(r(\ell, \Psi))]^2 \\
&= \int d\ell \, [\rho(r(\ell, \Psi))]^2 \left(\frac{\mu_n(\mathbf{x})}{c^n}\right).
\end{aligned}
\tag{2.12}
$$

Therefore, depending on the particle physics model considered, the effective $\mathcal{J}$-factor depends on different moments of the relative velocity distribution.

We can look at each moment more closely. In the case of the p-wave, the integral

$$
\mu_2(\mathbf{x}) \equiv \int d^3\mathbf{v}_{\mathrm{rel}} v_{\mathrm{rel}}^2 P_\mathbf{x}(\mathbf{v}_{\mathrm{rel}})
\tag{2.13}
$$

is the square of the intrinsic relative velocity dispersion of the system at a given $\mathbf{x}$. This provides a measure of the disordered motion of the relative velocities about $\mathbf{x}$. In the case of the d-wave model, it is useful to first define the following quantity

$$
\kappa(\mathbf{x}) = \frac{\int d^3\mathbf{v}_{\mathrm{rel}} v_{\mathrm{rel}}^4 P_\mathbf{x}(\mathbf{v}_{\mathrm{rel}})}{\left[\int d^3\mathbf{v}_{\mathrm{rel}} v_{\mathrm{rel}}^2 P_\mathbf{x}(\mathbf{v}_{\mathrm{rel}})\right]^2} = \frac{\mu_4(\mathbf{x})}{(\mu_2(\mathbf{x}))^2},
\tag{2.14}
$$

which is motivated from the general statistical definition of kurtosis. In the case of a Maxwell-Boltzmann distribution, we have $\kappa = 1.667$. Eq. (2.14) is useful because it is strongly dependent on the more extreme tails of the relative velocity distribution. For smaller κ the components of the velocity distribution are more strongly peaked near the mean value of the respective Gaussians, while for larger κ, the velocity components are more (symmetrically) broadly distributed relative to a Gaussian. As we discuss below, this has important implications for the determination of the $\mathcal{J}$-factors in these models.

2.4 Results

We now move on to determining the $\mathcal{J}_s$-factors for each of the MW-like halos, under the assumptions of the different annihilation cross section models discussed above.

Figure 2.5 shows the $\mathcal{J}_s$-factors as a function of the angle Ψ for all four cross section models for the Auriga and APOSTLE halos. Here we consider only the smooth halo component, so that all particles that are associated with subhalos of the main halo have been excluded. The ten Auriga MW-like halos, along with their DMO counterparts are shown in the left panel, while in the right panel we show the six APOSTLE MW-like halos and their DMO counterparts. At small angles, but still large enough to correspond to radii larger than the resolution limit, the clear trend in both simulations is for the $\mathcal{J}_s$-factors of the halos in the hydrodynamic simulations to be systematically larger than those of their DMO counterparts. This behavior is primarily attributed to the contraction of the DM density profiles due to the baryons in the inner parts of the halo, as seen in figure 2.1. As discussed before, in the APOSTLE halos, the contraction of the density profiles is smaller due to their smaller stellar masses, compared to Auriga halos. Hence, the difference between the $\mathcal{J}_s$-factors of the halos in the DMO and hydrodynamic simulations are also smaller.

Though the higher density of the halos in the hydrodynamic simulations at small radii provides a simple explanation for why the $\mathcal{J}_s$-factors are larger in the hydrodynamic case for all models, it is interesting to note the relative change in the $\mathcal{J}_s$-factor between the halos in the hydrodynamic simulations and their DMO counterparts for each model. Examining figure 2.5, we see that the largest relative change occurs when going from the DMO to the hydrodynamic case for the d-wave model. On the other hand, the smallest relative change occurs for the Sommerfeld model. The larger relative increase in the $\mathcal{J}_s$-factor for the d-wave is a reflection of the fact that the $\mathcal{J}_s$-factor in this case scales as the fourth moment of the relative velocity dispersion. To appreciate quantitatively the effect of the various velocity scalings, in figure 2.6, we show the ratios of the $\mathcal{J}_s$-factors of each model relative to the s-wave value.

Figure 2.7 shows the relative velocity moments for the Auriga MW-like halos, for the p-wave, d-wave and Sommerfeld models. The bottom right panel of figure 2.7 shows the kurtosis, as defined in eq. (2.14). As discussed above, the fourth moment is more sensitive to the small, but manifest differences in the tails of the relative velocity distribution as compared to a Maxwell-Boltzmann distribution. Comparing figures 2.5 and 2.7, we see that the scatter in the moment can be directly
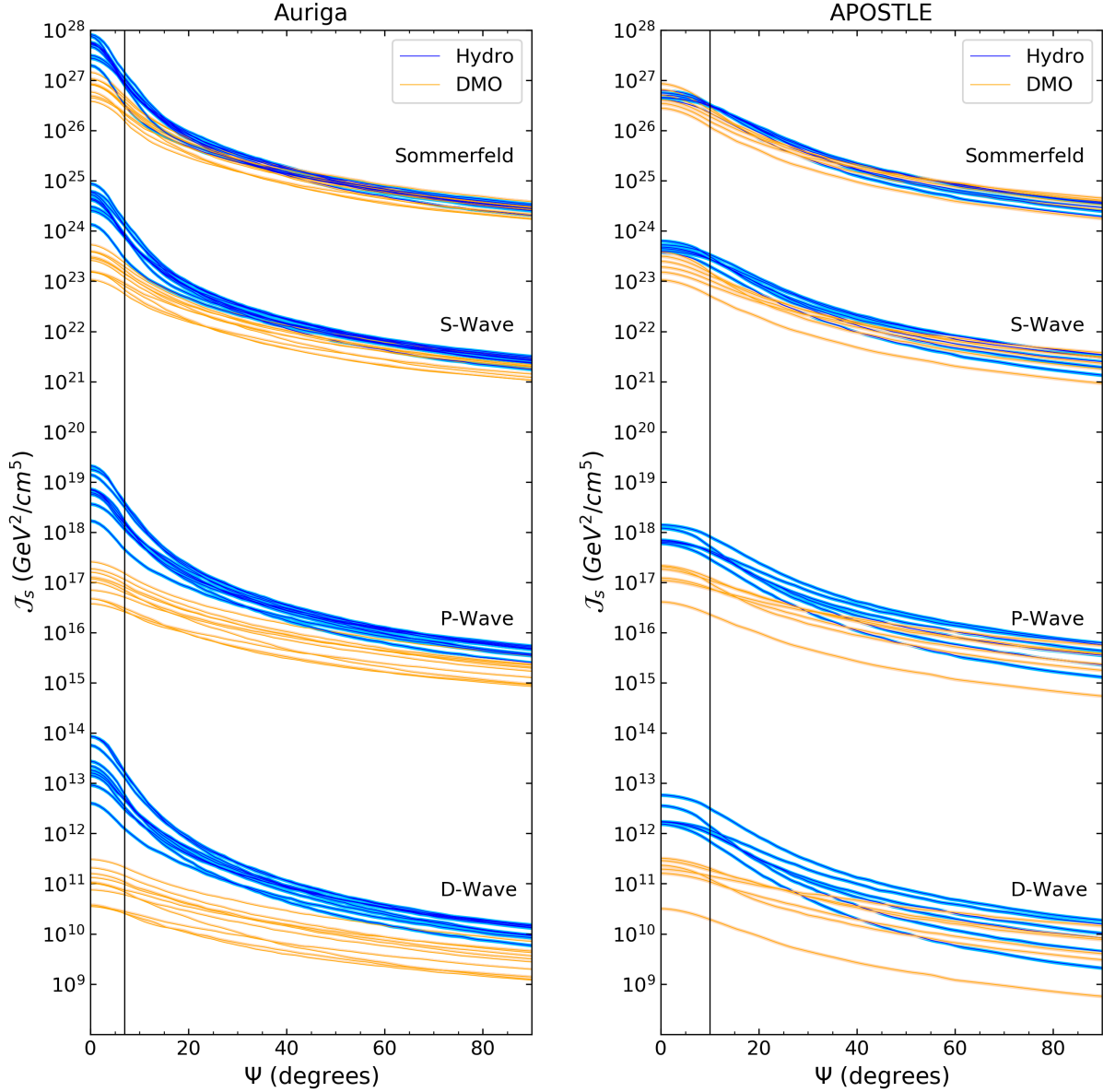
Figure 2.5: $\mathcal{J}_s$-factors for the different velocity-dependent models for Auriga (left panel) and APOSTLE (right panel) simulations. For each model, we show the $\mathcal{J}_s$-factors for the ten MW-like halos in the hydrodynamic simulations (blue) and their DMO counterparts (yellow). The black vertical lines specify the angle Ψ corresponding to the average Power radius for the Auriga and APOSTLE MW-like halos in the left and right panels, respectively. Reprinted with permission from ref. [2].

translated over to the scatter in the J-factor in each case.

In addition to the shift in the $\mathcal{J}_s$-factor itself, it is important to quantify the scatter in this

21
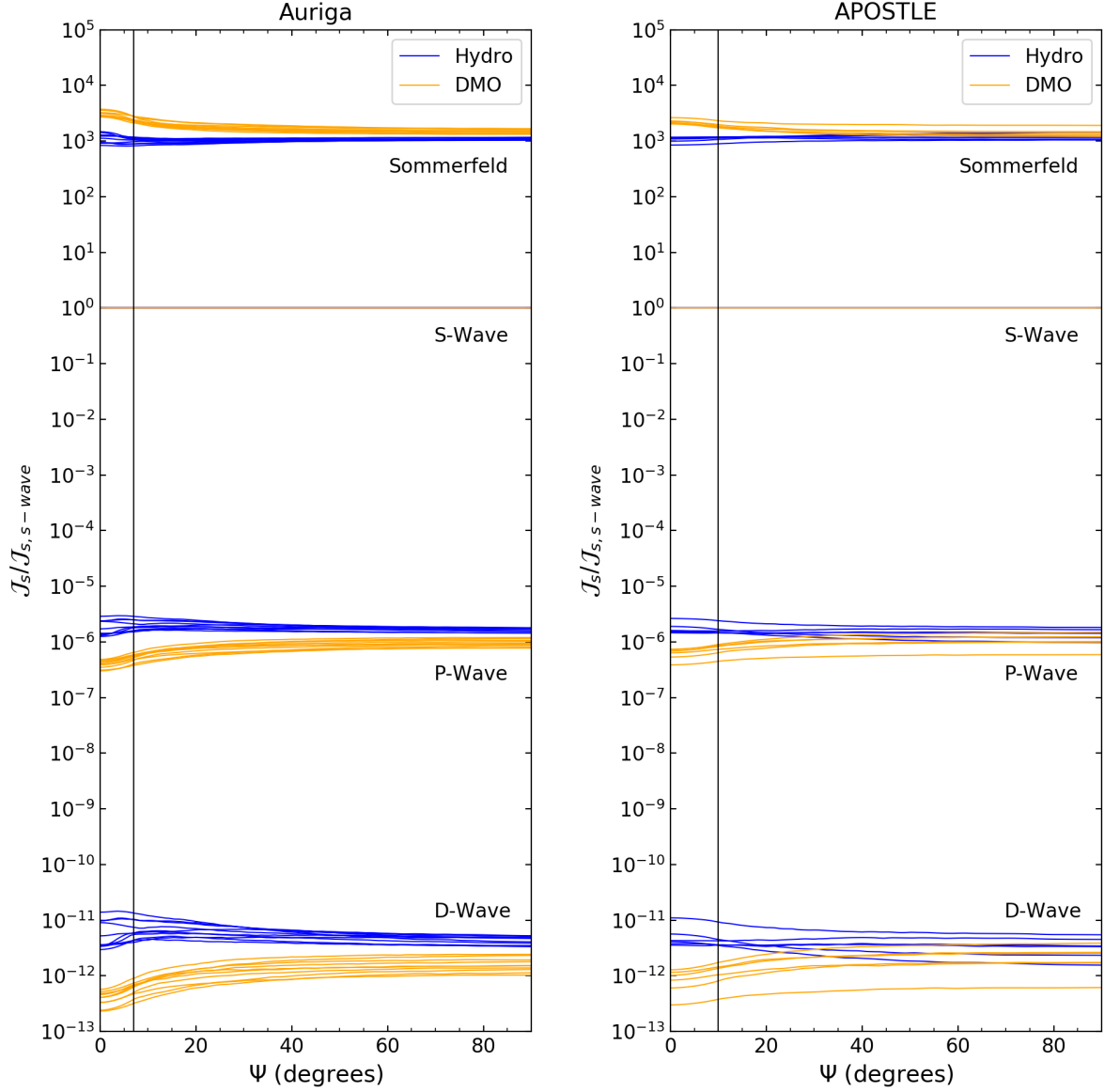
Figure 2.6: $\mathcal{J}_s$-factors as in figure 2.5, only plotted as a ratio relative to the s-wave value. Reprinted with permission from ref. [2].

quantity amongst the ten MW-like halos. Similar to the above, we find that the largest scatter is in the $\mathcal{J}_s$-factor of the d-wave model, and the smallest scatter is in the Sommerfeld model. In the case of the d-wave, this is again a result of the sensitivity of the $\mathcal{J}_s$-factor to the tails of the velocity distribution in these models. The integrand of the relative velocity moment, which in this case scales as $v_{\rm rel}^4 f(v_{\rm rel})$, exhibits a significant halo-to-halo scatter at the highest $v_{\rm rel}$, while at the lowest
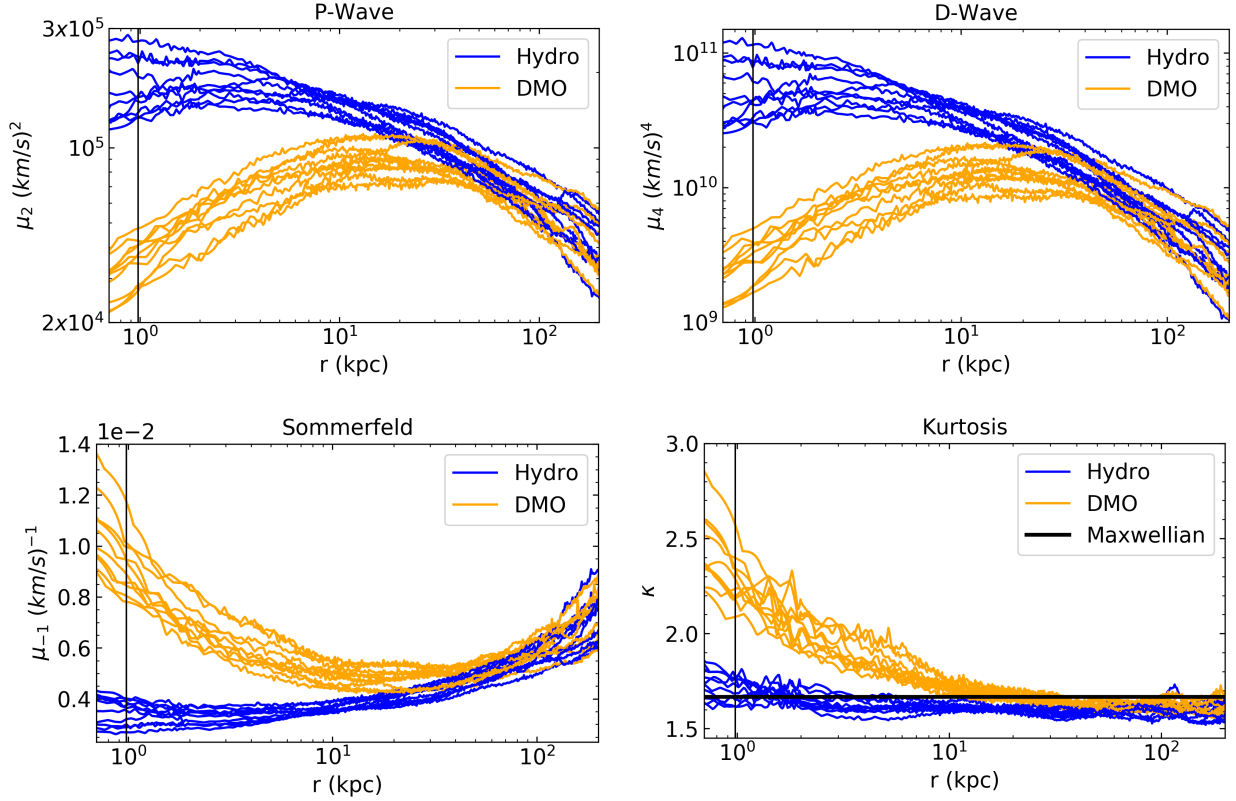
Figure 2.7: Velocity moments of the relative velocity distribution for the ten Auriga MW-like halos and their DMO counterparts. The panels are: Second moment (top left), Fourth moment (top right), inverse moment (bottom left). The bottom right panel shows the fourth moment divided by the square of the second moment, with the black horizontal line indicating this quantity for the Maxwell-Boltzmann relative velocity distribution. The black vertical lines specify the average Power radius of the Auriga halos. Reprinted with permission from ref. [2].

$v_{\rm rel}$, this integrand is nearly identical for all halos. At the other extreme for the Sommerfeld model there is significantly less scatter in the inverse moments, as shown in figure 2.7 for the Auriga halos. In this case the integrand of the velocity moments scales as $f(v_{\rm rel})/v_{\rm rel}$, and the scatter in this integrand at the largest $v_{\rm rel}$ is much less than for the d-wave case. In addition, at low $v_{\rm rel}$, the scatter in the integrand increases, partially compensating for the scatter at high $v_{\rm rel}$. Together, these effects combine to make the halo-to-halo scatter for the Sommerfeld model the smallest amongst our cross section models.

The features in the relative velocity distributions explain the relative differences between the

$\mathcal{J}_s$-factor of the halos in the hydrodynamic simulations and their DMO counterparts for a given annihilation cross section model. More generally, in all cases we find that the scaling of the $\mathcal{J}_s$-factors with angle is essentially entirely driven by the DM density profiles, and that this scaling depends very weakly on the characteristics of the DM relative velocity distributions. This can be best quantified by considering different lines-of-sight through a halo, which correspond to different values of Ψ, and averaging the DM density and the velocity dispersion along each line-of-sight. Figures 2.8 and 2.9 show the average DM density and velocity dispersion of the ten Auriga halos, respectively, against their average $\mathcal{J}_s$-factor, with each point in this plane representing a different value of Ψ. We see from figure 2.8 that for each cross section model, the average density correlates with the average $\mathcal{J}_s$-factor, while from figure 2.9, there is minimal correlation with the average velocity dispersion in each case. This implies that, even for velocity dependent models, understanding the systematics in the DM density is the most important factor in determining the $\mathcal{J}_s$-factor.

We reiterate that the analysis of this dissertation has focused on determining the $\mathcal{J}$-factors for the smooth halo component. The contribution from DM subhalos bound to the host galaxy is expected to boost the $\mathcal{J}$-factor for each annihilation model. For halos in the hydrodynamic simulations and assuming s-wave annihilation, the boost factor from resolved subhalos is expected to be small, corresponding for $\lesssim 1\%$ increase over the smooth halo contribution [76]. While determining the boost factor for velocity-dependent models is beyond the scope of our current analysis, we can roughly estimate the increase in density due to subhalos by including the particles bound to subhalos[2] in our calculations, and determining the spherically-averaged density and velocity distributions. With the subhalos included, we find at most $\sim 20\%$ increase in the $\mathcal{J}_s$-factors, which is manifest at values of Ψ near the resolution limit of our simulations. This justifies our approach of focusing on the smooth halo, and indicates that the inclusion of subhalos leads to only a small increase in the $\mathcal{J}$-factors over the scales that we consider.

---

[2]More precisely, DM particles bound to subhalos belonging to the same *friends-of-friends* [77] group as the main halo are included, with a dimensionless linking length of 0.2 times the mean interparticle spacing.
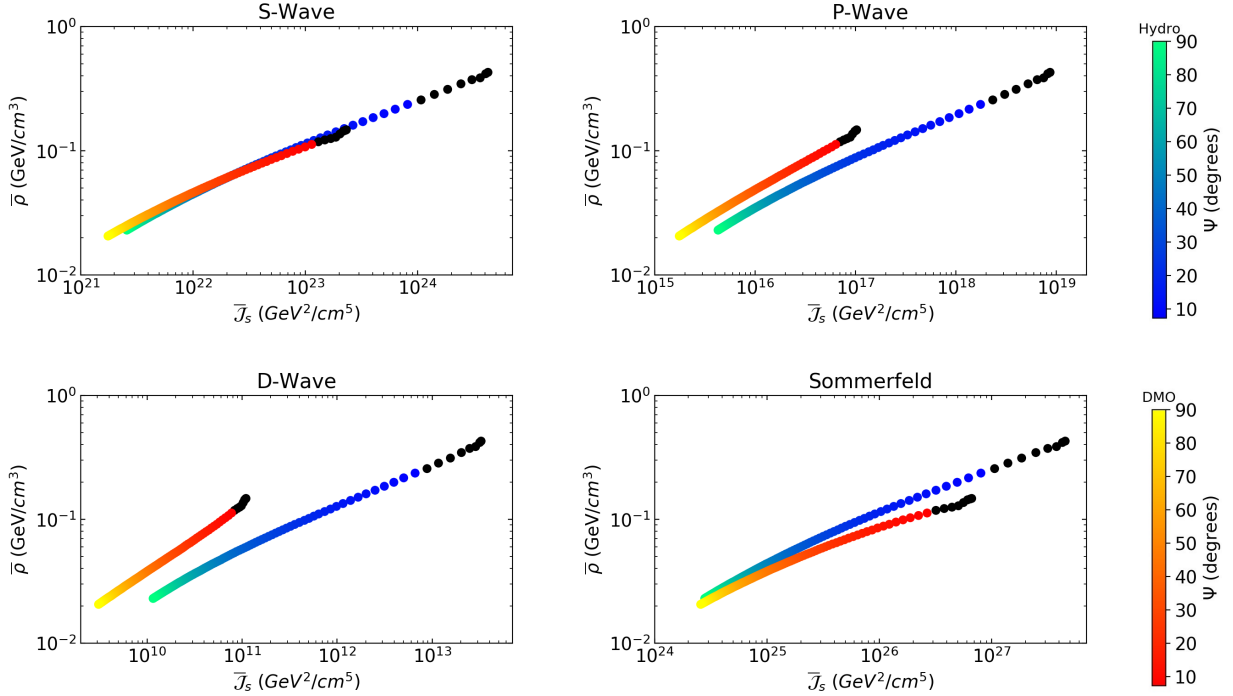
Figure 2.8: Correlation between the DM density and $\mathcal{J}_s$-factor for Auriga halos (green to blue colored points) and their DMO counterparts (yellow to red colored points). Each point represents the average of the density and $\mathcal{J}_s$-factors over all the halos ($\bar{\rho}$ and $\bar{\mathcal{J}}_s$, respectively), along a line-of-sight at a given angle Ψ. The color bars on the right indicate the values of the angle from the galactic center. Angles start from $\simeq 10$ degrees, as angles at lower radii are below the resolution limit (specified by black points on the plots). Each panel shows this correlation for a different cross section model. Reprinted with permission from ref. [2].

2.5   Discussion and Conclusions

In this dissertation we have performed the first study of the DM relative velocity distribution of Milky Way-like halos, using the Auriga and APOSTLE cosmological simulations. We find that the DM pair-wise relative velocity distribution at nearly all radii in the halos is consistent with the Maxwell-Boltzmann distribution. This agreement is particularly good for the simulations that include baryons. For the corresponding DMO-simulations, the agreement with the Maxwell-Boltzmann distribution is good, though there are some notable deviations, particularly at small radii as the center of the halo is approached.

We have explored the implications for velocity-dependent DM annihilation, focusing on the

Figure 2.9: Same as figure 2.8, except for the average velocity dispersion, $\bar{\sigma}$, instead of the density. Note that while figure 2.8 uses log-log axes, the data in this figure is presented on semi-log axes. Reprinted with permission from ref. [2].

Sommerfeld ($1/v$), s-wave (v^0), p-wave (v^2), and d-wave (v^4) models. We generally show that the $\mathcal{J}$-factors scale as the moments of the relative velocity distribution, and that the halo-to-halo scatter is largest for d-wave, and smallest for Sommerfeld models.

Our results indicate that in velocity-dependent models, the $\mathcal{J}$-factor is strongly correlated with the DM density in the halo, and is very weakly correlated with the velocity dispersion. This implies that if the DM density in the Milky Way can be robustly determined, one can accurately predict the DM annihilation signal, without the need to identify the DM velocity distribution in the Galaxy.

In calculating the $\mathcal{J}$-factors for velocity-dependent models, we have neglected the impact of DM substructure within the Milky Way-like galaxies. The effect of substructure has been explored for s-wave models in several previous studies [78, 76], which indicate that the corrections for substructure are small, at least at the resolution limits of present simulations. It is possible that boost factors can be significant for extrapolations down to $\sim$ Earth-mass subhalos, in particular

for Sommerfeld-enhanced models. Accurately calculating the boost factors for velocity-dependent models required determining the concentration-mass relation for subhalos [79] and their velocity distribution, and understanding how to extrapolate these beyond the resolution limit of the simulations. We leave this topic as a subject for future study.

The results we have presented will be important in guiding searches for velocity-dependent DM annihilation, for example with Fermi-LAT data or with future data from higher-energy gamma-ray instruments. Though p-wave and d-wave annihilation may be realized in simple models [80, 81, 82], due to the sensitivity of these instruments, for the simplest models bounds on p-wave [83, 31] and d-wave [31] cross sections are much larger than those for thermal relic DM. Bounds may be improved upon by considering more unique astrophysical environments, for example the supermassive black hole at the center of the Milky Way [34]. The phenomenology becomes richer for multi-state DM, such that Sommerfeld boosts can enhance the p-wave component and suppress the s-wave component [84]. The results we have presented provide the most realistic approach available to providing robust constraints on these velocity-dependent models with astrophysical systematics incorporated.

3. VELOCITY-DEPENDENT ANNIHILATION RADIATION FROM DM SUBHALOS IN COSMOLOGICAL SIMULATIONS*

We use the suite of MW-like galaxies in the Auriga [35] simulations to determine the contribution to annihilation radiation from DM subhalos in three velocity-dependent DM annihilation models: Sommerfeld, p-wave, and d-wave models. We compare these to the corresponding distribution in the velocity-independent s-wave annihilation model.

In this work we use the high resolution level (Level 3) of the Auriga simulations with DM particle mass, $m_{\mathrm{DM}} = 5 \times 10^4 \ \mathrm{M_\odot}$, baryonic mass, $m_b = 6 \times 10^3 \ \mathrm{M_\odot}$, and Plummer equivalent gravitational softening length of $\epsilon = 184$ pc [43, 44]. For the analysis in this work, we consider DM particles bound to the smooth halo component as well as DM particles bound to subhalos, as identified by the SUBFIND algorithm [85]. These simulations can resolve subhalos of mass greater than $\sim 10^6 \ \mathrm{M_\odot}$, which contain at least 20 DM particles. We also extrapolate our results to subhalos with mass lower than that of the resolution limit of the simulations.

3.1 Properties of DM Subhalos

In this section, we discuss the dynamical properties of the DM subhalos that are most important for our analysis. We focus specifically on the DM density profiles, the maximum circular velocities, and the DM relative velocity distributions. These properties are then used in the subsequent sections to calculate the DM annihilation luminosity from each subhalo.

3.1.1 Density Profiles

For each subhalo, we obtain the spherically-averaged DM density profile from the DM mass contained within spherical shells centered on the center of potential of each subhalo as determined by SUBFIND. The number of DM particles per subhalo varies greatly between subhalos, with the minimum number being 20 DM particles. Thus, we use variable bin widths,
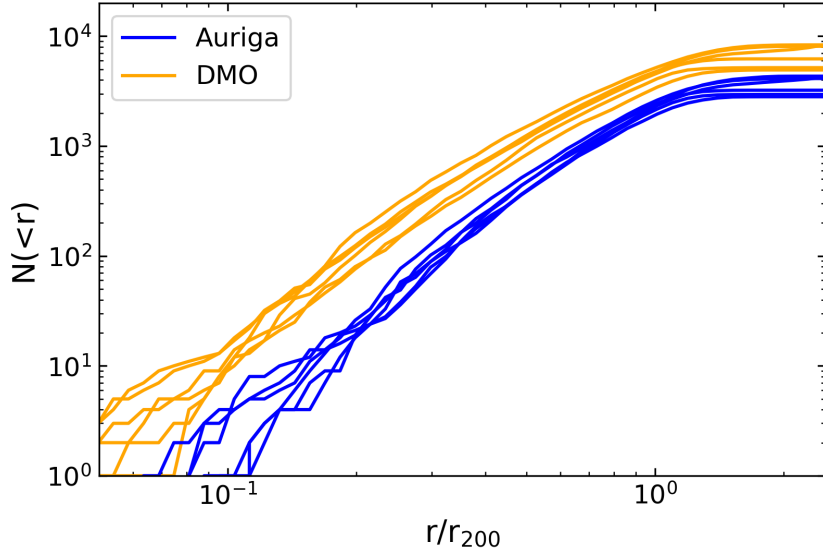
Figure 3.1: The cumulative number of subhalos enclosed within a sphere of Galactocentric radius r for each Auriga halo (blue) and its DMO counterpart (orange). See table 2.1 for the virial radius, r_{200}, of each Auriga halo. Reprinted with permission from ref. [3].

ensuring that there is a minimum of 5 DM particles (for smaller subhalos) and a maximum of 200 DM particles (for larger subhalos) within each shell. For reasons discussed in section 3.2, we define large subhalos to have an angular size > 1 degree as viewed from the solar position, and small subhalos to have an angular size < 1 degree. We fit the DM density profile constructed from the data to an Einasto density profile

$$\rho = \rho_{-2} \exp\left(-\frac{2}{\alpha}\left[\left(\frac{r}{r_{-2}}\right)^\alpha - 1\right]\right), \tag{3.1}$$

where ρ_{-2} and r_{-2} are the density and radius at which $\rho(r) \propto r^{-2}$, and α is a parameter which specifies the curvature of the density profile. We set this parameter to $\alpha = 0.16$ [86]. In order to account for numerical resolution, we fit the Einasto density profile to the simulation data for radii larger than 2ϵ, where ϵ is the softening length defined in section 1.5. At large radii, we fit the profile up to a maximum radius of $2R_{\max}^{\text{SUBFIND}}$, where $R_{\max}^{\text{SUBFIND}}$ is the radius of maximum circular velocity derived from the SUBFIND algorithm [85]. Beyond $2R_{\max}^{\text{SUBFIND}}$, a large fraction
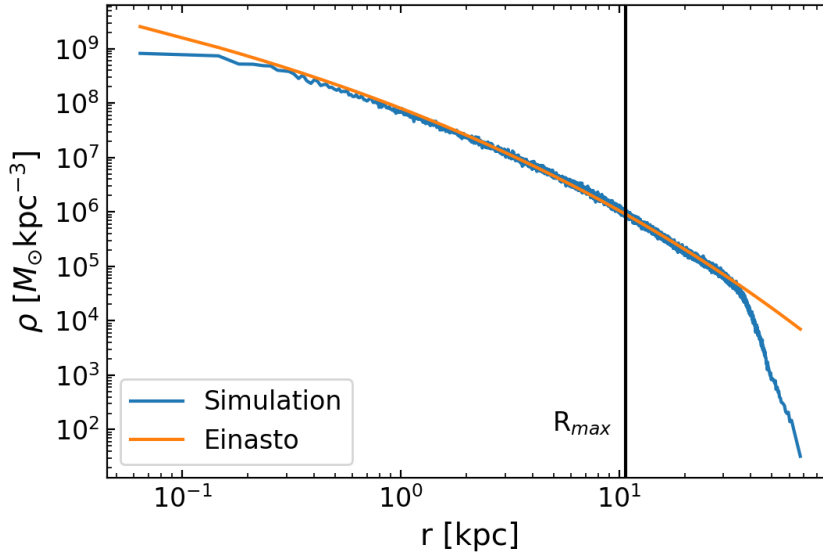
Figure 3.2: The DM density profile for a large subhalo in the Au6 simulation where r is the distance from the center of the subhalo. The results from the simulation data and the best-fit Einasto profile are shown in blue and orange, respectively. This subhalo has a stellar mass of 4×10^9 M$_\odot$, DM mass of 4×10^{10} M$_\odot$, and $V_{\mathrm{max}} = 75$ km/s at $R_{\mathrm{max}} = 10.7$ kpc, which is indicated by the vertical black line. For large subhalos in the sky maps in section 3.2, we use the local DM density as estimated by a Voronoi tessellation for distances larger than R_{max} and use the best-fit Einasto density profile to estimate the local DM density for distances within R_{max}. Reprinted with permission from ref. [3].

of subhalos have their density profiles tidally stripped, such that they fall off faster than an Einasto density profile.

We also calculate R_{max} and V_{max} for each subhalo from the particle distribution. For an individual DM subhalo, most of the annihilation signal comes from within R_{max}, the radius where the circular velocity $V_c(r)$ reaches a maximum, V_{max}. For each subhalo, we calculate the circular velocity curve $V_c(r) = \sqrt{GM(<r)/r}$, where $M(<r)$ is the total DM mass enclosed within a sphere of radius r centered on the subhalo. We find that our calculations of V_{max} and R_{max} are consistent with the values returned by SUBFIND. For internal consistency, we will use our calculations of V_{max} and R_{max} in this work. The V_{max} and R_{max} are used in section 3.2 to estimate the total annihilation luminosity within R_{max} for each subhalo.

Figure 3.2 shows the DM density profile of one example subhalo from Auriga halo Au6, along

with the best fit Einasto density profile for that subhalo. Also shown is the R_{max} value for the same subhalo. Due to the resolution limit of the simulation, the density profile calculated from the particle data underestimates the density in the central regions of the subhalos. For small subhalos in the sky maps in section 3.2, we will estimate the total DM annihilation luminosity using the calculated values of V_{max} and R_{max}. For large subhalos in the sky maps, we use the best fit Einasto density profile for particles within R_{max} and we use the local DM density estimated by a Voronoi tessellation of the DM particle distribution for particles beyond R_{max}. Following ref. [5], we apply a Voronoi tesselator to estimate the DM distribution in the outer radii of each subhalo, allowing the calculation of ρ_i from the DM particle mass and the cell volume surrounding the i-th DM particle. For these large radii, this approach provides a better localized measure of the DM density than other estimates which smooth over a particle's nearest neighbors [87].

3.1.2 Relative Velocity Distributions

We now discuss the DM relative velocity distributions of subhalos using the notation established in our previous work [2]. For each subhalo, we write the probability distribution of DM particles associated with only that subhalo as

$$P_{\mathbf{x}}(\mathbf{v}) = \frac{f(\mathbf{x}, \mathbf{v})}{\rho(\mathbf{x})}, \tag{3.2}$$

where $\mathbf{x}$ is the position vector, $\mathbf{v}$ is the velocity vector, and the DM density at a position $\mathbf{x}$ in the subhalo is normalized as

$$\rho(\mathbf{x}) = \int f(\mathbf{x}, \mathbf{v}) \mathrm{d}^3 \mathbf{v}. \tag{3.3}$$

The velocity vectors of the DM particles are determined with respect to the center of the main halo, whereas the position vectors are determined with respect to the center of the respective subhalo. This is appropriate as we are calculating the DM relative velocity distribution of particles within each subhalo, so that the bulk subhalo motion is subtracted out. Using spherical shells as defined in section 3.1.1, we resolve the velocity vectors into three components then subtract the components of the velocities in this basis, being careful to avoid double counting. We then take

31
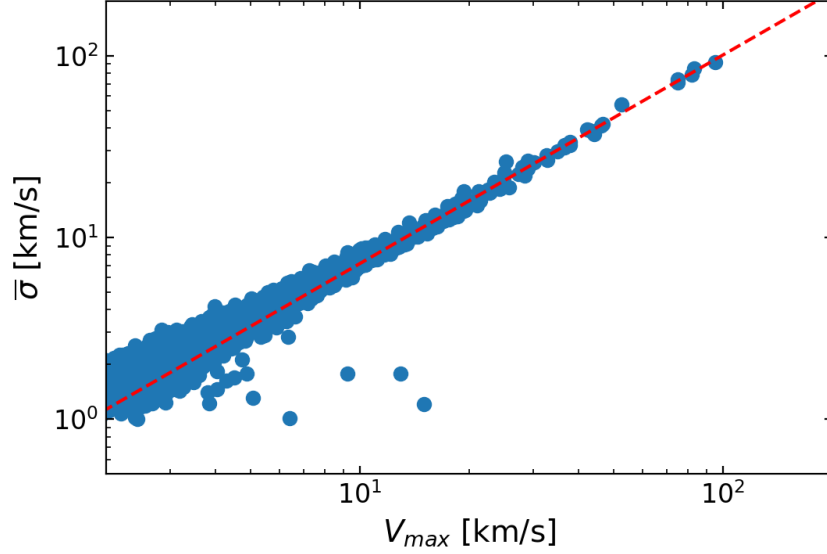
Figure 3.3: The distribution in $V_{\max} - \overline{\sigma}$ space of subhalos from all six Auriga halos within R_{200} of each respective halo. We find $\overline{\sigma}$ by calculating the DM relative velocity distribution in radial shells, fitting a Maxwell-Boltzmann curve to the distribution with a 1D velocity dispersion σ, and then taking the average of these σ values over all shells for each subhalo. The dashed red line indicates the best-fit power-law curve found to be $\overline{\sigma} = 0.51(V_{\max})^{1.15}$, which we will use to extrapolate to lower mass subhalos. A similar result is obtained from the DMO simulations, where $\overline{\sigma} = 0.55(V_{\max})^{1.10}$. Our results are consistent with the power law relation found in ref. [4]. Reprinted with permission from ref. [3].

the modulus of the components of the pairwise relative velocities, which provides an estimate of $P_{\mathbf{x}}(\mathbf{v}_{\rm rel})$. In each radial shell, $P_{\mathbf{x}}(|\mathbf{v}_{\rm rel}|)$ is normalized to unity, such that

$$\int P_{\mathbf{x}}(|\mathbf{v}_{\rm rel}|)\, dv_{\rm rel} = 1 \tag{3.4}$$

and therefore we have $\int P_{\mathbf{x}}(\mathbf{v}_{\rm rel})\, d^3\mathbf{v}_{\rm rel} = 1$.

Though there is some variation in the velocity distribution of subhalos, ref. [4] shows that for MW dwarf spheroidal analogues, $P_{\mathbf{x}}(|\mathbf{v}_{\rm rel}|)$ can be well approximated by a Maxwell-Boltzmann (MB) distribution,

$$P_{\rm MB}(|\mathbf{v}_{\rm rel}|) = \sqrt{\frac{2}{\pi}} \frac{v_{\rm rel}^2}{\sigma^3}\, \exp\left(-\frac{v_{\rm rel}^2}{2\sigma^2}\right), \tag{3.5}$$

where σ is the 1D relative velocity dispersion.

In the analysis of ref. [4], the best fit MB distribution is found in spherical shells at different radii from the center of the subhalo. Then the mean best fit peak speed of the MB distributions over all shells is calculated for each subhalo. Ref. [4] finds that velocity-dependent $\mathcal{J}$-factors can be accurately estimated using the mean best fit MB parameters in simulated MW dwarf spheroidal galaxies.

Following the same procedure as in ref. [4], we fit a MB distribution to the DM relative velocities in different spherical shells in each subhalo, and calculate the mean of the velocity dispersion, $\overline{\sigma}$, over all spherical shells in each subhalo. Figure 3.3 shows the relationship between the V_{max} of a given resolved subhalo and the $\overline{\sigma}$ of the best-fit Maxwellian. The dashed line indicates the best-fit power-law curve which we will use to extrapolate to low-mass subhalos.

3.2 Annihilation Luminosities

The annihilation luminosity from the DM particles is calculated from the DM density and the DM relative velocity distribution at each point within the halo. For the general case of velocity-dependent models, the annihilation luminosity from some region of space can be written as

$$L_n = \int \mathrm{d}^3 \mathbf{x} \int \mathrm{d}^3 \mathbf{v}_{\mathrm{rel}} P_{\mathbf{x}}(\mathbf{v}_{\mathrm{rel}}) \left(\frac{v_{\mathrm{rel}}}{c} \right)^n [\rho(x)]^2 . \tag{3.6}$$

For our velocity-dependent models, we examine the following possibilities: $n = -1$ (Sommerfeld-enhanced annihilation), $n = 0$ (s-wave annihilation), $n = 2$ (p-wave annihilation), and $n = 4$ (d-wave annihilation). The different cross section models correspond to different velocity moments of the relative velocity distribution [2],

$$\mu_n(\mathbf{x}) \equiv \int \mathrm{d}^3 \mathbf{v}_{\mathrm{rel}} P_{\mathbf{x}}(\mathbf{v}_{\mathrm{rel}}) v_{\mathrm{rel}}^n, \tag{3.7}$$

where $\mu_n(\mathbf{x})$ is the n-th moment of the relative velocity distribution $P_\mathbf{x}(\mathbf{v}_{\mathrm{rel}})$. In terms of the velocity moments, the annihilation luminosity can be written as

$$L_n = \int \mathrm{d}^3\mathbf{x} \, [\rho(x)]^2 \left(\frac{\mu_n(\mathbf{x})}{c^n} \right). \tag{3.8}$$

The annihilation luminosity has contributions from both the smooth halo and the subhalo components. We start by estimating the annihilation luminosity from the smooth component of the DM halo. Using the Voronoi tessellation method described above, we estimate the local DM density at the location of each DM particle. Then we calculate the relative velocity distribution at each point on a spherical grid, using the nearest 500 DM particles. The relative velocity distributions are then used in eq. (3.7) to obtain $\mu_n(\mathbf{x})$ for each annihilation model at each point. We interpolate these results to obtain the relative velocity moments at the location of each DM particle in the smooth halo. We then compute the integral in eq. (3.8) over each volume produced by the Voronoi Tessellation to obtain the annihilation luminosity produced by each DM particle in the smooth halo.

For the subhalo component, we calculate the annihilation luminosity by splitting up the contribution from large and small subhalos. As mentioned in section 3.1.1, we consider large subhalos to have an R_{max} which corresponds to an angular size > 1 degree as seen from the solar position of $8.0 \, \mathrm{kpc}$, whereas we consider small subhalos to have an R_{max} which corresponds to an angular size of < 1 degree. We use this angular size definition for large and small subhalos, because 1 degree corresponds to the approximate angular resolution scale for Fermi-LAT at the energies relevant for DM searches. For large subhalos in the simulations, we calculate the annihilation luminosity from each DM particle using methods similar to that of the smooth halo component. The only difference is that the relative velocity moments, $\mu_n(\mathbf{x})$, are calculated using a Maxwell-Boltzmann distribution with a dispersion set equal to the mean velocity dispersion, $\overline{\sigma}$, computed as described in section 3.1.2. We use the mean dispersion to estimate the relative velocity moment for all points within the subhalo, and therefore μ_n would be independent of the position vector in the subhalos.

For smaller subhalos in our simulations, whose R_{max} has an angular size less than 1.0 degree,

Sommerfeld

S-wave

P-wave

D-wave
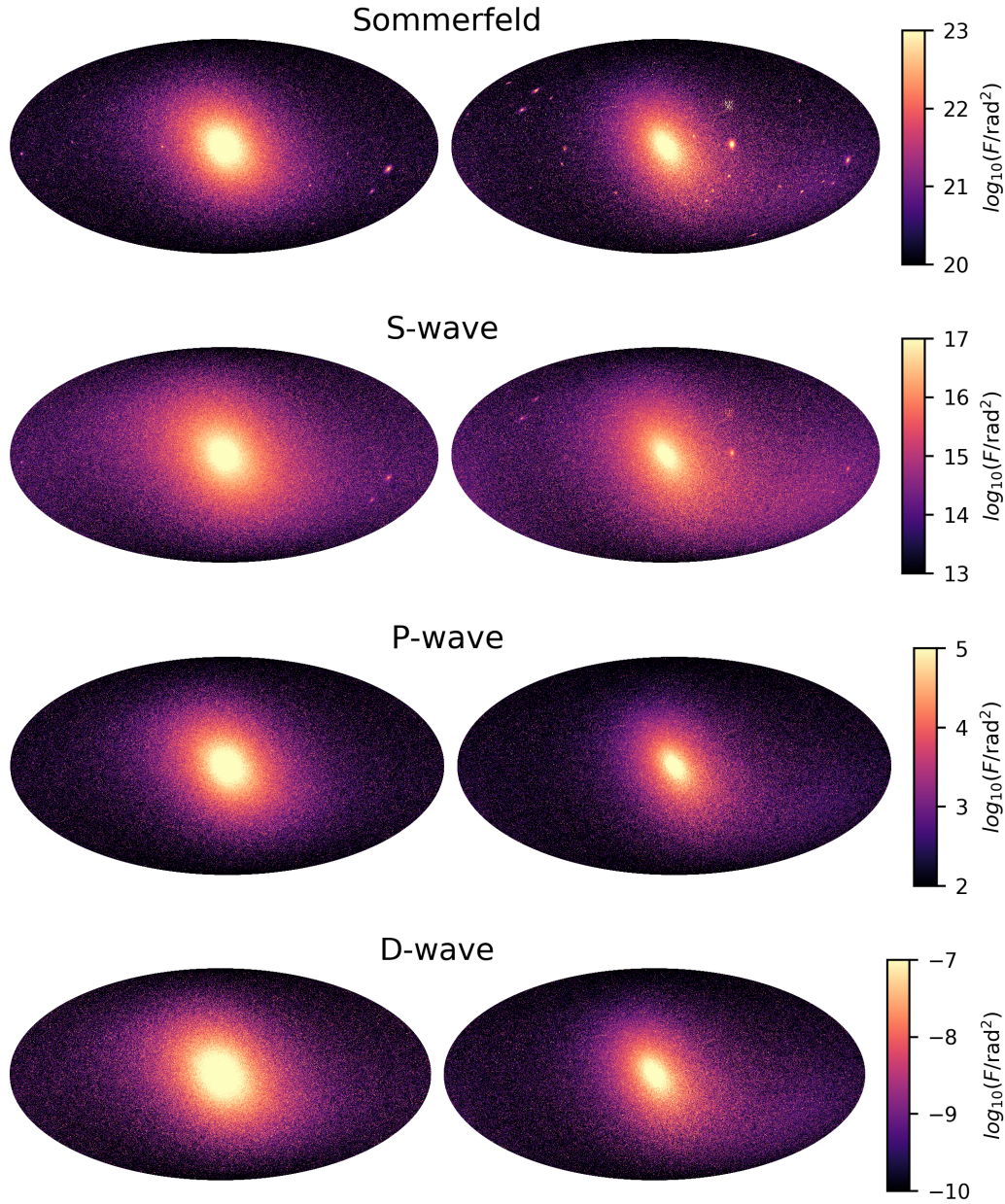
Figure 3.4: All-sky Mollweide projections of the DM annihilation flux density for each considered annihilation model as seen from the midplane of the stellar disc, 8.0 kpc from the Galactic center of the Au6 halo (left) and its DMO counterpart (right). The color bars to the right of each pair of sky maps show the approximate range of the annihilation flux density for each annihilation model. The DM annihilation fluxes from subhalos are clearly systematically fainter compared to the smooth halo component in all annihilation models than in the Sommerfeld model, with the faintest subhalos shown in the d-wave model. Reprinted with permission from ref. [3].

we estimate the total DM annihilation luminosity from a spherical region interior to $R_{\max}$ as

$$L_{\mathrm{sub}} = \frac{C_{\mathrm{Einasto}}V_{\max}^4}{G^2 R_{\max}}, \tag{3.9}$$

where G is the gravitational constant and $C_{\mathrm{Einasto}} = 1.87$ for an Einasto density profile with $\alpha = 0.16$ [5]. Since we have chosen a μ_n that is not dependent on position for subhalos, we can then rewrite eq. (3.8) as

$$
\begin{aligned}
L_{n,\mathrm{sub}} &= \left(\frac{\mu_n}{c^n}\right) \int \mathrm{d}^3\mathbf{x}\,[\rho(x)]^2 \\
&= \left(\frac{\mu_n}{c^n}\right) L_{\mathrm{sub}} \\
&= \left(\frac{\mu_n}{c^n}\right) \left(\frac{C_{\mathrm{Einasto}}V_{\max}^4}{G^2 R_{\max}}\right).
\end{aligned} \tag{3.10}
$$

Then including the contribution from the smooth component and the subhalos, we examine these luminosities from one solar position at 8.0 kpc from the Galactic center by calculating the annihilation flux as in ref. [5],

$$F = L/d^2, \tag{3.11}$$

where L is the luminosity of a subhalo or DM particle and d is the heliocentric distance of that subhalo or DM particle. We sum the annihilation flux from the smooth DM halo, large DM subhalos, and small DM subhalos in bins of equal angular size of 1.9×10^{-5} rad^2. The results of the flux density for each annihilation model are shown in figure 3.4. The all-sky Mollweide projection maps on the left are the results for Au6 and those on the right are for its DMO counterpart. For each annihilation model, we find that the smooth component of the DM halo is brighter and rounder in shape in the hydrodynamical simulations compared to their DMO counterparts. We also find that subhalo fluxes are systematically fainter in the hydrodynamical simulations than their DMO counterparts for each annihilation model, consistent with previous results that examined s-wave models [5]. When comparing the subhalo fluxes for different annihilation models in the same simulation, we find that the subhalo flux relative to the flux from the smooth halo component appears

to be largest for the Sommerfeld model. Subhalo fluxes are suppressed relative to the smooth halo in the p-wave and d-wave models, which we will quantify in section 3.3.

3.3 Results

In this section we present the primary results of our analysis. We begin by comparing the contribution to the luminosity from subhalos and the smooth halos in the simulations. We then characterize the contribution of the integrated subhalo luminosity due to subhalos across different luminosity scales. We also estimate the impact of extrapolating the luminosity function of subhalos below the lowest mass ($\sim 10^6$ M$_\odot$) subhalos resolved in the simulations.

3.3.1 Luminosities of the Smooth Halos and Resolved Subhalos

Figure 3.5 shows the DM annihilation luminosities of six Auriga halos within a distance r/r_{200}, where r is the radial distance from the Galactic center and r_{200} is the virial radius of each halo. Shown are both the contributions from the smooth DM halo and from the subhalos for each of the six Auriga halos (left four panels) and the results for their DMO counterparts (right four panels). The gray lines indicate the luminosity from the smooth DM halo of each simulated Auriga halo for each annihilation model, while the thin blue, yellow, green, and red lines show the luminosity from all subhalos within an Auriga halo for the s-wave, p-wave, d-wave, and Sommerfeld models, respectively. For each model, the thick lines of the same color show the average total subhalo luminosity across all six halos. The purple lines show the total mass of the smooth component within radius r for each halo.

We compare the results for the average total subhalo luminosity to the total smooth halo luminosity. For the Auriga halos, we find that the luminosity from the smooth DM halo dominates over the average luminosity from subhalos in all annihilation models except for the Sommerfeld model, where the subhalo luminosity dominates at $r/r_{200} > 0.74$. For the DMO halos, we find that the luminosity from the smooth DM halo dominates for p-wave and d-wave annihilation, but the average luminosity from subhalos surpasses that of the smooth DM component at $r/r_{200} > 1.2$ for the s-wave model and at $r/r_{200} > 0.17$ for Sommerfeld.
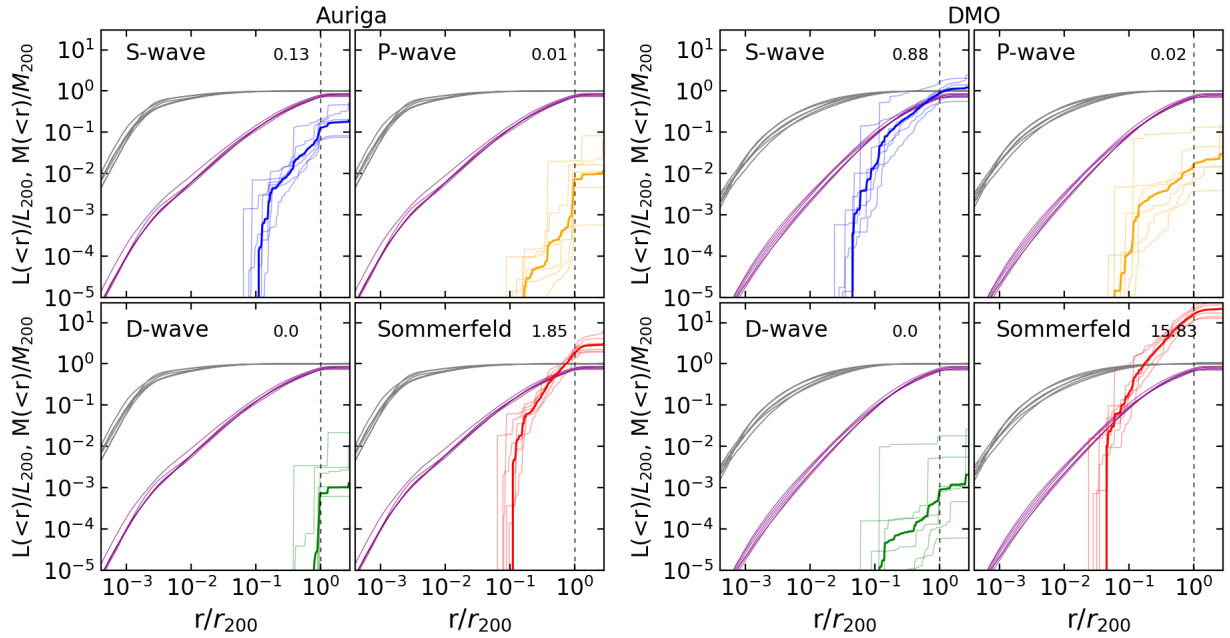
Figure 3.5: The total DM annihilation luminosity within some Galactocentric radius, r, as a function of that radius for the Auriga halos (left four panels) and their DMO counterparts (right four panels). The gray lines are the results from the smooth DM halo component of the six Auriga halos. The results for the resolved DM subhalos in each halo are shown as thin blue (s-wave), yellow (p-wave), green (d-wave), and red (Sommerfeld) lines. The thick lines of the same color correspond to the average total luminosity of resolved subhalos across all six Auriga halos. In each panel, the number in the upper right indicates the average total luminosity from subhalos within r_{200}. Both luminosities from the smooth halo component and the subhalos have been normalized by the total luminosity, L_{200}, within r_{200} for the corresponding smooth halo component for each annihilation model. The purple lines indicate the total smooth mass within r for each halo, normalized by the total mass, M_{200}, within r_{200}. The dashed vertical lines indicate r_{200} for all halos. The luminosities from the velocity-independent s-wave annihilation model agree with the results of ref. [5]. Reprinted with permission from ref. [3].

Next we compare the results from the Auriga halos to that of their DMO counterparts. Examining the smooth halo components, we see that the luminosities of the Auriga halos approach L_{200} more rapidly at smaller radii than their DMO counterparts, which is also illustrated by the brighter central regions in the sky maps in figure 3.4. This effect is a result of the contraction of the central regions of the smooth DM halos due to the presence of baryons. For a given annihilation model, we find that the subhalo luminosities in the DMO simulations typically have a larger value at the same distance r/r_{200}. This is due to baryonic processes in which the baryonic disc preferentially
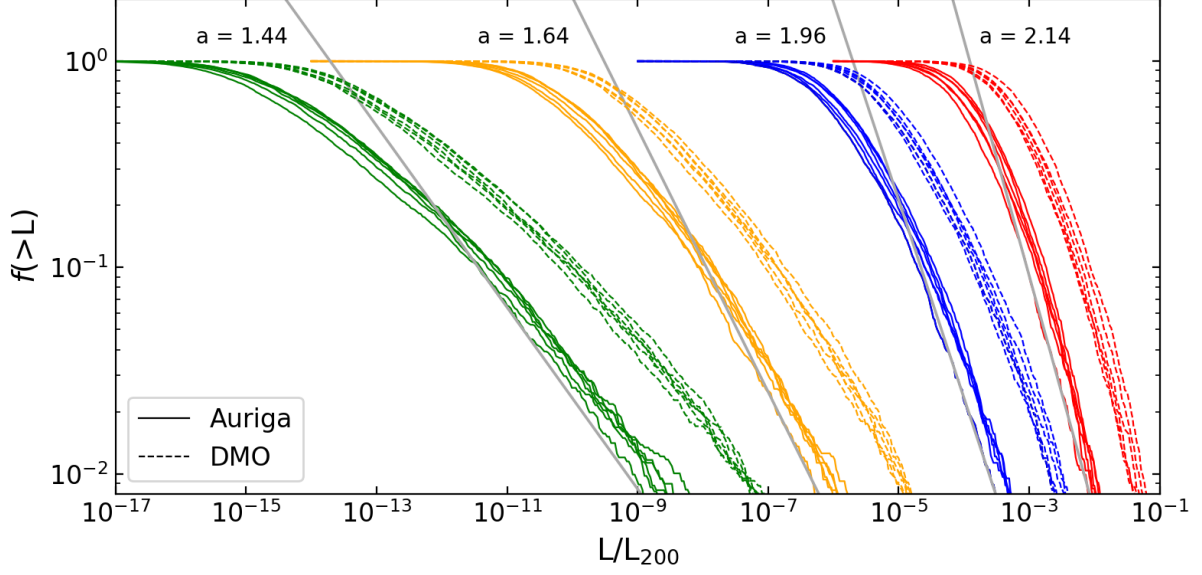
Figure 3.6: The fraction of subhalos with luminosity greater than some luminosity, L, relative to the total luminosity, L_{200}, within r_{200} of each smooth halo component. For s-wave (blue), p-wave (yellow), d-wave (green), and Sommerfeld (red) annihilation models we show the results for both the Auriga halos and their DMO counterparts in solid and dashed lines, respectively. The gray lines indicate the best fit power law for Au6 over the range of luminosities associated with subhalos with $20\,\mathrm{km/s} \leq V_{\mathrm{max}} \leq 60\,\mathrm{km/s}$. The best fit values of a from eq. (3.13) for Au6 are listed next to the corresponding gray line. Reprinted with permission from ref. [3].

destroys nearby subhalos.

3.3.2 Subhalo Luminosity Functions

We now move on to analyze the subhalo differential luminosity functions, dN/dL, where N is the number of subhalos with luminosity L, for each of our annihilation models. From this defini-tion of the differential luminosity function, we construct the fraction of subhalos with luminosity greater than L/L_{200} within each simulation for each DM annihilation model,

$$f(> L) \equiv \frac{\int_{L}^{L_{max}} L' \frac{dN}{dL'} dL'}{\int_{L_{min}}^{L_{max}} L' \frac{dN}{dL'} dL'}. \tag{3.12}$$

To provide a physical interpretation for the cumulative luminosity function, we compare to a

power law defined as

$$f(> L) \propto L^{-(a-1)}. \tag{3.13}$$

Defined in this manner, the subhalo luminosity function is dominated by the highest (lowest) luminosity subhalos for $a < 2$ ($a > 2$). In order to conservatively avoid the impact of numerical resolution, we calculate this quantity over the range of L calculated from subhalos with $20 \, \mathrm{km/s} \leq V_{\mathrm{max}} \leq 60 \, \mathrm{km/s}$ for each simulation.

Figure 3.6 shows the cumulative luminosity function, $f(> L)$, within each simulated halo for each DM annihilation model. S-wave (blue), p-wave (yellow), d-wave (green), and Sommerfeld (red) annihilation models are shown for the Auriga halos (solid lines) and their DMO counterparts (dashed lines). The gray lines and corresponding a values indicate the best fit parameters of eq. (3.13) for Au6. For the Auriga halos we find the range of a values to be $[1.80 - 2.07]$ for s-wave, $[1.45 - 1.66]$ for p-wave, $[1.38 - 1.49]$ for d-wave, and $[2.10 - 2.43]$ for the Sommerfeld model. For the DMO counterparts we find the range of a values to be $[1.75 - 1.99]$ for s-wave, $[1.50 - 1.61]$ for p-wave, $[1.35 - 1.44]$ for d-wave, and $[1.94 - 2.34]$ for the Sommerfeld model.

These fit results indicate that for the case of the Sommerfeld model, the integrated subhalo luminosity is dominated by the least luminous subhalos, while for s, p and d-wave models, the luminosity is dominated by the most luminous subhalos. Going from s to d to p-wave, the high luminosity subhalos become more and more significant as a fraction of the total subhalo emission, even though similarly going from s to d to p-wave, the total luminosity contribution from subhalos becomes progressively smaller as compared to the smooth halo.

To further examine the contributions to the luminosity from different subhalo mass intervals, the four panels on the left side of Figure 3.7 show the contribution to the subhalo luminosity from Au6 for different DM mass ranges and the four panels on the right side show the results for the DMO counterpart. We consider the luminosities of all subhalos with DM masses above a minimum mass of 10^6, 10^7, 10^8, 10^9, and 10^{10} $\mathrm{M_\odot}$. We calculate the total luminosity from subhalos within r_{200} and above a minimum mass of 10^8 $\mathrm{M_\odot}$ as a fraction of the total luminosity from resolved subhalos within r_{200}. For Au6 we find the luminosity fraction to be 0.689 for s-wave,
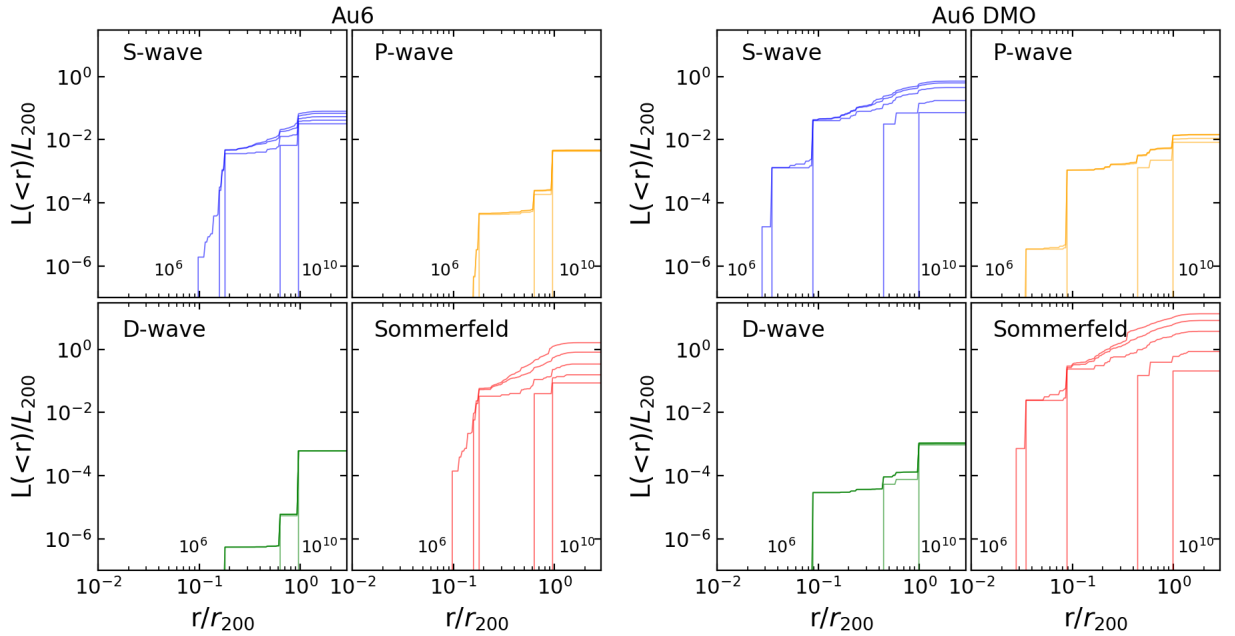
Figure 3.7: The luminosity contribution from Au6 subhalos for each annihilation model for various lower limits of the subhalo DM mass. Each line corresponds to a minimum DM mass of $10^6, 10^7, 10^8, 10^9$, or 10^{10} M$_\odot$. The lines corresponding to higher mass subhalos trend to the right side of each panel. This shows that most of the total subhalo luminosity is due to large subhalos in the s-wave, p-wave, and d-wave annihilation models. However, in the case of Sommerfeld annihilation there is a notable fraction of luminosity from low-mass subhalos. We find similar results for all six halos. Reprinted with permission from ref. [3].

0.996 for p-wave, 1.000 for d-wave, and 0.177 for Sommerfeld. For the DMO counterpart we find the luminosity fraction to be 0.626 for s-wave, 0.977 for p-wave, 0.999 for d-wave, and 0.264 for Sommerfeld. For s-wave, p-wave, and d-wave annihilation models, a large part of the total luminosity is due to high-mass subhalos. Whereas in the case of the Sommerfeld model we find that there is a large contribution to the total subhalo luminosity from low-mass subhalos.

3.3.3 Low-Mass Subhalo Extrapolation

As discussed above, the Auriga simulations resolve DM subhalo masses down to $\sim 10^6$ M$_\odot$. However, this is plausibly still much larger than the cut-off mass in cold DM, which may be as small as Earth mass [88]. It is interesting to estimate the effects that an extrapolation down to mass scales below the Aurgia resolution would have on our results.

In this analysis, for computational convenience we extrapolate DM subhalos down to $\sim 10^0\,\mathrm{M}_\odot$. To estimate the abundance of these low-mass subhalos below the resolution scale, we follow the work of ref. [5]. For each halo, we estimate the overall abundance of subhalos in the range $0.1\,\mathrm{km/s} \leq V_{\mathrm{max}} \leq 10\,\mathrm{km/s}$, with a subhalo of maximum circular velocity $0.1\,\mathrm{km/s}$ corresponding approximately to a subhalo of mass $10^0\,\mathrm{M}_\odot$. We assign a V_{max} value to each of the extrapolated subhalos using the differential V_{max} function in ref. [5]. The subhalo is then assigned an R_{max} value using the median $R_{\mathrm{max}} - V_{\mathrm{max}}$ relation shown in ref. [5] and derived from ref. [89] for extrapolation to lower subhalo masses. These values for V_{max} and R_{max} are then used in eq. (3.9) to estimate the velocity-independent s-wave annihilation luminosity for extrapolated subhalos.

Figure 3.3 above shows the relationship between the V_{max} of a given resolved subhalo and the $\overline{\sigma}$ value associated with that subhalo as discussed in section 3.1.2. The dashed line indicates the best-fit power-law curve which we will use to extrapolate to low-mass subhalos. The extrapolated $\overline{\sigma}$ values are used to produce a Maxwellian distribution, which is then used in eq. (3.7) as the probability distribution, $P_{\mathbf{x}}$, to calculate the velocity moment, μ_n, for each of the velocity-dependent annihilation models. The extrapolated velocity moments, along with the V_{max} and R_{max} calculated above, are then used in eq. (3.8) to estimate the velocity-dependent annihilation luminosity for extrapolated subhalos.

Given the structural properties of the extrapolated subhalos, we then must assign them a position within the halo. To assign the position, we start from a spherically symmetric number density distribution that is generated from the resolved subhalos with $10\,\mathrm{km/s} < V_{\mathrm{max}} < 30\,\mathrm{km/s}$. We then fit a power-law curve to this number density profile, which we use to radially distribute the subhalos. These objects are then distributed randomly in the angular coordinates, which produces a spherically symmetric distribution of subhalos.

The effects of the addition of extrapolated subhalos on the total luminosity for all six Auriga halos are depicted in the left four panels of figure 3.8 and the results for their DMO counterparts are shown in the right four panels. For the Auriga halos, we still find that the luminosity from the smooth DM halo dominates over the average luminosity from subhalos in all models except for
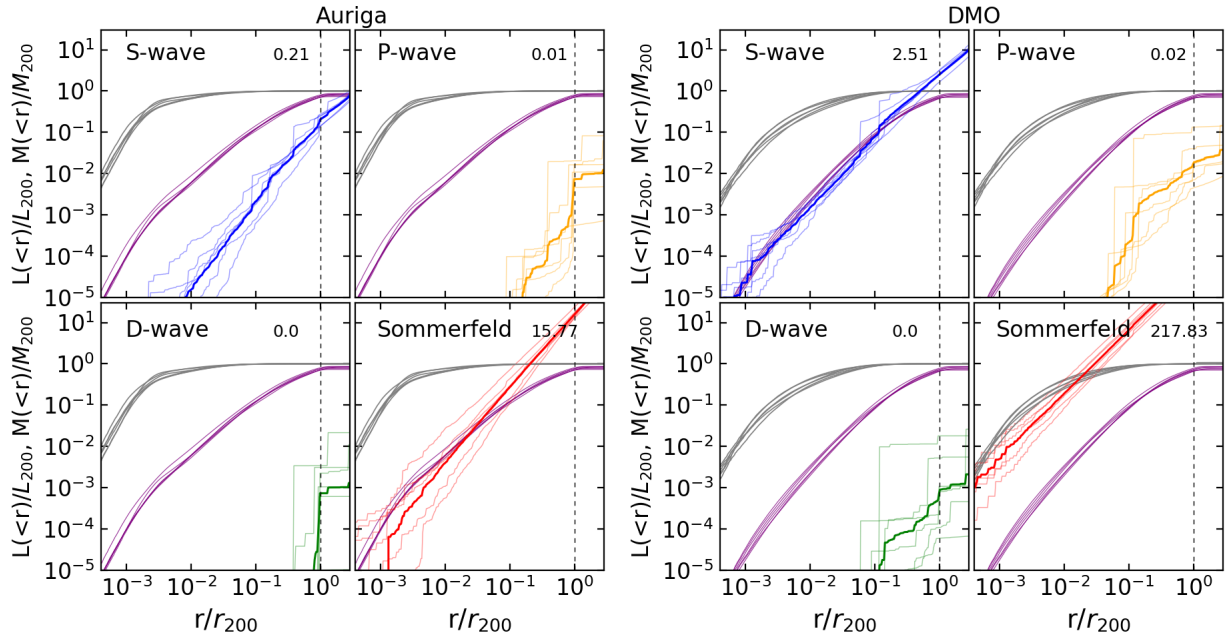
Figure 3.8: Same as figure 3.5, but including the results for extrapolated subhalos with $0.1 \text{ km/s} \leq V_{\text{max}} \leq 10 \text{ km/s}$. In each panel, the number in the upper right indicates the average total luminosity due to resolved and extrapolated subhalos within r_{200}, normalized by L_{200}. Reprinted with permission from ref. [3].

Sommerfeld annihilation, which now dominates at $r/r_{200} > 0.2$ rather than at $r/r_{200} > 0.74$ in the case of only resolved subhalos. For the DMO counterparts, we find that the average luminosity from subhalos now dominates for the s-wave model at $r/r_{200} > 0.5$ and for the Sommerfeld model at $r/r_{200} > 0.03$.

3.4 Discussion and Conclusions

We have used the Auriga simulations of Milky Way-like galaxies to determine the contribution of halo substructure to the signal from DM annihilation. We consider the general case of velocity-dependent DM annihilation, examining Sommerfeld, s-wave, p-wave, and d-wave models. We find that substructure is the most significant in Sommerfeld models, while it is the least significant in d-wave models. In the Sommerfeld models, the substructure contribution to the DM annihilation signal dominates that of the smooth component beyond $\sim 0.74 r_{200}$, while for all other models the substructure contribution is sub-dominant at all radii as compared to the smooth halo.

43

Examining the luminosity functions of substructure, we find that in Sommerfeld models, the luminosity function is dominated by the least massive subhalos that are resolved. On the other hand, for d-wave models, the luminosity function is dominated by the most massive subhalos that are resolved. So extrapolating to lower subhalo mass scales may still increase the luminosity contribution from subhalos in Sommerfeld models, though it will not affect the luminosity contribution from subhalos in the case of d-wave models.

Systematic uncertainties in the results can also arise from the uncertainty in the number of subhalos, due to a different treatment of baryonic effects. We do not expect these uncertainties to affect our results for the d-wave model, since the luminosities are not centrally concentrated in that case. However, they can introduce additional uncertainties in our results for the Sommerfeld model. Studying the $\mathcal{J}$-factors in an even larger sample of simulations is important to quantify such uncertainties.

Another source of systematic uncertainty can arise from the assumed DM density profile of the subhalos. In our analysis, we have assumed the shape of the DM density profile interior to R_{max} to be an Einasto density profile, and we have estimated the total luminosity of each subhalo using $C_{\mathrm{Einasto}} = 1.87$ in eq. 3.10. Since V_{max}, R_{max}, and μ_n are calculated directly from the simulation data, the total luminosity may be sensitive to the choice of DM density profile. To examine the systematic arising from the assumed profile, we consider simply how our results change when assuming an NFW profile instead of an Einasto profile. For the NFW case, we can estimate the total luminosity from a subhalo using an NFW profile with $C_{\mathrm{NFW}} = 1.23$ [78]. This implies that using an NFW profile instead of an Einasto profile would simply scale our results by $\gtrsim 30\%$, $L_{\mathrm{sub}}^{\mathrm{NFW}} = 0.66\, L_{\mathrm{sub}}^{\mathrm{Einasto}}$, for all annihilation models.

The results of our analysis have interesting implications for gamma-ray emission observed by Fermi-LAT. For example, the Galactic Center Excess (GCE) does not yet have a clear explanation, and may be consistent with particle DM annihilation [90]. However, it is possible that this emission is inconsistent with limits obtained from dwarf galaxies [91]. Including the full effect of baryonic physics, the morphology of the GCE [92] is consistent with the signal from the smooth

component of the DM distribution [87]. Since the morphology of the smooth emission component is similar for Sommerfeld, s-wave, p-wave, and d-wave models, the GCE would similarly be well fit by the smooth component of any of these velocity-dependent models. The bounds on the cross section would simply scale with the ratio of the $\mathcal{J}$-factors, in a manner similar to that discussed in Ref. [32]. However, one caveat to this statement is that the simulations that we have considered resolve subhalos down to mass scales of $\gtrsim 10^6$ M$_\odot$. This may be far larger than the actual minimum subhalo mass, and an extrapolation down to lower subhalo masses may be particularly important for Sommerfeld models, in which case the subhalo component may eventually dominate over the smooth halo emission.

Another galaxy that our results may be considered in the context of is M31. Fermi-LAT has previously detected emission from the central regions of M31, which may be explained via cosmic-ray interactions in the central stellar disk [93]. More recently, there has been an indication of an extended emission from the region surrounding M31, which may be explained by emission from its more extended DM halo [94]. The M31 system is a unique target for DM annihilation, because halo substructure is expected to contribute to the emission in the outermost regions. Our results indicate that, even in the context of the full physics simulations, substructure emission is significant for Sommerfeld models, and even in the case of s-wave models the total emission from subhalos nears that of the smooth component around r_{200}. However, for p and d-wave models, the smooth component is dominant at all radii, and no emission from substructure would be identified. This shows that M31 provides a unique system for DM annihilation and substructure analysis, and we defer its detailed study to future work.

4. VELOCITY-DEPENDENT $\mathcal{J}$-FACTORS FOR MILKY WAY DWARF SPHEROIDAL ANALOGUES IN COSMOLOGICAL SIMULATIONS*

We extract the DM density and relative velocity distributions of the MW's dSphs from the APOSTLE Level 1 hydrodynamical simulations [37, 38], and compute the $\mathcal{J}$-factors for the simulated dSphs for the s-wave, p-wave, d-wave, and Sommerfeld models. To extract the relative velocity distributions, we first identify analogues of MW satellite galaxies in the APOSTLE simulations by matching observed properties such as the circular velocity at the half-light radius and stellar mass to the corresponding subhalos in the simulation. From these best analogue candidates, we extract the DM relative velocity distribution, and thereby the $\mathcal{J}$-factors for the MW analogue subhalos. As an additional key component of our analysis, we compare the DM relative velocity distributions from the subhalos to MB distributions, from which we ascertain how well the MB distribution works over the entire range of resolved subhalo mass scale in APOSTLE.

4.1 dSph Galaxy Analogues

In this section, we discuss the properties of the dSph analogues that we identify in our simulations. We begin by defining a broad matching criteria to map dSphs onto subhalos in the APOSTLE simulations, and then move onto characterizing the density profiles of these systems, and finally determine the DM velocity distributions in the analogues.

4.1.1 Selection of dSph Analogues

The selection of specific dSph analogues was performed using two matching criteria. The first criterion involves matching the observed circular velocity at the half-light radius of the dSphs [11]. For each subhalo, we first calculate the circular velocity, $V_c(r) = \sqrt{GM(<r)/r}$, where $M(<r)$ is the total mass enclosed within a sphere of radius r centered on the subhalo. We then compute $V_c(r_{1/2})$, or $V_{1/2}$, where $r_{1/2}$ is the 3D half-light radius for each of our dSph counterparts [95].

Most generally, we require that our dSph analogues have a circular velocity at the half-light radius within 2σ of the observed value, where σ is the uncertainty from observations, which is typically a few km/s for the dSphs that we consider. The only exception is for the Draco analogues, which, as described below, we require it to be within 3σ of the observed value, due to the difficulty in identifying a matching analogue.

As our second criterion, we require that the subhalos have a stellar mass that is consistent with the measured stellar mass of its observed counterpart [11]. Further, considering that typical stellar mass-to-light ratios for dSph stellar populations are in the range $\sim 1 - 3$, and extending this range by 50% to increase the number of matching analogues, we take the range of dSph stellar masses that we consider to be within the range $0.5 - 4.5$ of the measured stellar mass of the dSph.

Given the relatively small sample of satellites in our simulations, and the precise measurements of the stellar mass and circular velocity, it is expected that our matching criteria will not produce exact dSph analogues. This is particularly true when considering the distance to the dSph. In the cases in which we find a matching circular velocity and stellar mass, but there is a significant difference between the distance to the observed satellite and the distance to the simulated satellite, we simply shift the simulated satellite to a distance corresponding to that of the observed satellite [96]. We choose this approach because we are most interested in the $\mathcal{J}$-factors below, which are a sensitive function of the dSph distance.

With our criteria we identify 126 unique subhalos in AP-L1 as dSph analogues. We further refine our selection of dSph analogues based on the modeling of their DM density profiles, as discussed in section 4.1.2. This reduces our number of unique subhalos in AP-L1 to 100 subhalos. The results of our search for analogues are shown in table 4.1. For each dSph, the number of subhalos identified as analogues, N, is given in the second column of this table. Note that N may contain subhalos that are analogues of multiple dSphs. For each dSph, we also show the top two best matching analogues based on their s-wave $\mathcal{J}$-factor being closest to those of ref. [6] (also shown in figure 4.7 in section 4.3), as well as several properties for each analogue. In several instances, for example with Sculptor, Carina, and Sextans, we find good matches between a

dSph Analogue	N	$M_\star^{\text{obs}}$ [M$_\odot$]	$M_\star$ [M$_\odot$]	$V_{1/2}^{\text{obs}}$ [km/s]	$V_{1/2}$ [km/s]	V_{max} [km/s]	$\log_{10}(\widetilde{\mathcal{J}}_{\text{s}})$ [GeV^2 cm^{-5}]
Canes Venatici I (1)	21	2.3×10^5	5.66×10^5	13.2	14.56	15.39	17.42
Canes Venatici I (2)			2.50×10^5		14.79	16.05	17.44
Carina (1)	17	4.3×10^5	2.38×10^5	11.1	11.30	13.14	18.52
Carina (2)			9.30×10^5		11.37	22.89	18.15
Draco (1)	4	2.2×10^5	8.91×10^5	17.5	14.92	24.32	18.81
Draco (2)			8.89×10^5		15.28	29.01	18.82
Fornax (1)	4	1.7×10^7	1.36×10^7	18.5	18.79	20.38	18.01
Fornax (2)			1.20×10^7		18.36	21.96	17.87
Leo I (1)	19	5.0×10^6	3.27×10^6	15.6	15.24	20.37	17.63
Leo I (2)			3.52×10^6		15.15	24.81	17.64
Leo II (1)	47	7.8×10^5	1.45×10^6	11.4	12.15	20.13	17.66
Leo II (2)			6.86×10^5		10.58	21.90	17.66
Sculptor (1)	9	2.5×10^6	1.40×10^6	15.6	14.97	26.11	18.58
Sculptor (2)			5.52×10^6		15.81	27.73	18.61
Sextans (1)	3	5.9×10^5	3.89×10^5	12.3	12.77	12.79	17.88
Sextans (2)			3.88×10^6		11.61	11.70	17.91
Ursa Minor (1)	23	3.9×10^5	4.61×10^5	19.9	19.13	25.52	18.76
Ursa Minor (2)			8.91×10^5		19.28	24.32	18.74

Table 4.1: The number of subhalos identified as dSph analogues, N, stellar mass, $M_\star$, the circular velocity at the half-light radius, $V_{1/2}$, the maximum circular velocity, V_{max}, and the s-wave $\mathcal{J}$-factors of our selected dSph analogues in AP-L1. The observed stellar mass, $M_\star^{\text{obs}}$, and the observed circular velocity at the half-light radius, $V_{1/2}^{\text{obs}}$ of the dSphs are also given in the table. Note that a given subhalo may be identified as being more than one dSph analogue. Reprinted with permission from ref. [4].

simulated satellite and the observed system. On the other hand, as alluded to above, for Draco we are unable to locate reasonable analogues using the matching criterion of 2σ uncertainty for $V_{1/2}$. This is similar to what has been found in previous similar studies [36], as Draco is less dense than is predicted given its best matching analogues in simulations. Allowing up to 3σ uncertainty for $V_{1/2}$, we do obtain four Draco analogues across the ten simulated halos.

4.1.2 DM Density Profiles

We now move on to characterizing the DM density profiles of the subhalos. Characterizing the density profiles are important since they enter into the calculation of the DM annihilation rate through the $\mathcal{J}$-factor. We follow the typical assumption that the particle distributions in the
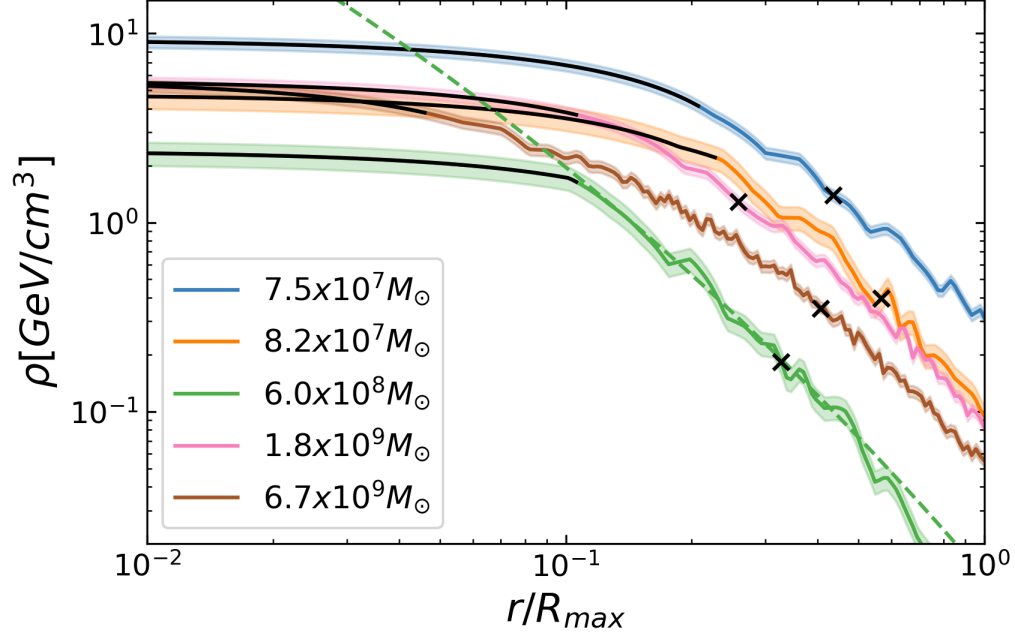
Figure 4.1: Spherically-averaged DM density profiles for a subset of five subhalos in the AP-L1 simulations, with masses in the range of $7 \times [10^7 - 10^9]$ M$_\odot$. The black portion of each curve represents the density at radii smaller than 268 pc, i.e. twice the gravitational softening length. The lighter shaded region represents the 1σ error, found using Poisson statistics. The dashed green line shows the best fit Einasto profile for the 6.0×10^8 M$_\odot$ subhalo. The black cross on each curve specifies the radius containing half the stellar mass of each subhalo. Reprinted with permission from ref. [4].

subhalos are spherically symmetric, which has been shown to be a good assumption for simulated dwarf galaxies in APOSTLE [97].

In figure 4.1 we show the spherically-averaged DM density profiles of five example subhalos of different masses. For each simulated subhalo, the DM density is obtained from the DM mass in spherical shells of width ranging from $[0.1 - 1.0]$ kpc, and plotted as a function of r/R_{max}, where r is the distance from the subhalo center, which is identified as the center of potential of that subhalo, and R_{max} is the radius at which the rotation curve of the subhalo reaches its maximum value. The bin width of the spherical shells was chosen such that there is a minimum of 10 particles per shell.

As is shown in figure 4.1, the density profiles start to flatten towards the inner regions of the subhalos. This is due to the resolution limit of the simulations, which is determined by the gravitational softening length, $\epsilon = 134$ pc. In figure 4.1, the black portion of the curves represent

the density profiles at radii less than twice the softening length. The black cross on each curve specifies the radius containing half of the stellar mass of each subhalo. An important question regarding the flattening of the density profiles is whether it can be a result of the baryonic feedback prescription used in the simulations. However, we note that this is not the case in our simulations. In particular, refs. [98] and [99] showed that the EAGLE baryonic feedback model, which is also used by APOSTLE, does not create cores in dwarf galaxies.

We model the DM density profile of the simulated subhalos by the Einasto profile,

$$\rho = \rho_{-2} \exp \left(-\frac{2}{\alpha} \left[\left(\frac{r}{r_{-2}} \right)^{\alpha} - 1 \right] \right), \tag{4.1}$$

where ρ_{-2} and r_{-2} are the density and radius at which $\rho(r) \propto r^{-2}$, and α is a parameter which specifies the curvature of the density profile. We set this parameter to $\alpha = 0.16$ [86], so only the two parameters ρ_{-2} and r_{-2} are varied. For each subhalo, we find the best fit Einasto profile in the range of $2\epsilon < r < 2R_{\mathrm{max}}$, using 2ϵ rather than ϵ to be conservative and avoid resolution issues. As an example, in figure 4.1 the dashed green line shows the best fit Einasto profile for the 6.0×10^8 M$_\odot$ subhalo. It is clear that the central region of the simulated subhalos are under-dense compared to what is expected from the Einasto fit, which is typically true throughout all the simulated subhalos examined.

We note that for some of the more massive subhalos, the density profiles show a flattening even for radii larger than 2ϵ. To take this into account, we also find the best fit Einasto profiles in the range of $3\epsilon < r < 2R_{\mathrm{max}}$. To ensure that our results are robust with respect to the specific range used for fitting the density profiles, we proceed as follows. We calculate the $\mathcal{J}$-factors of our dSph analogues using the best fit Einasto profile in the range of $2\epsilon < r < 2R_{\mathrm{max}}$ and compare the results to the $\mathcal{J}$-factors calculated using a best fit Einasto profile in the range of $3\epsilon < r < 2R_{\mathrm{max}}$. We then compute the ratio of these two $\mathcal{J}$-factors and remove any dSph candidate that has a $\mathcal{J}$-factor ratio which exceeds by more than 1σ from the mean $\mathcal{J}$-factor ratio. This cut reduces our number of analogues from 126 to 100, as mentioned previously.

4.1.3 Relative Velocity Distributions

For velocity-dependent annihilation models, the $\mathcal{J}$-factors depend not only on the DM density profile, but also on the DM pair-wise, or relative velocity distribution in the subhalo. We now describe how we extract the DM relative velocity distributions in radial shells in each subhalo.

We first extract the position vector, $\mathbf{x}$, and the velocity vector, $\mathbf{v}$, of the simulation particles belonging to each subhalo, with respect to the center of that subhalo. Following the notation used in ref. [2], we define $f(\mathbf{x}, \mathbf{v})$ such that $f(\mathbf{x}, \mathbf{v})\, d^3\mathbf{x}\, d^3\mathbf{v}$ is the number of DM particles within a phase space volume $\mathbf{x} + d^3\mathbf{x}$ and $\mathbf{v} + d^3\mathbf{v}$. The probability distribution of DM velocities at a position $\mathbf{x}$ can be written as

$$P_{\mathbf{x}}(\mathbf{v}) = \frac{f(\mathbf{x}, \mathbf{v})}{\rho(\mathbf{x})}, \tag{4.2}$$

where the DM density at $\mathbf{x}$ is given by

$$\rho(\mathbf{x}) = \int f(\mathbf{x}, \mathbf{v}) d^3\mathbf{v}. \tag{4.3}$$

For a given pair of DM particles with velocities $\mathbf{v}_1$ and $\mathbf{v}_2$, we can write the individual velocities in terms of the center-of-mass velocity, $\mathbf{v}_{\mathrm{cm}}$, and the relative velocity, $\mathbf{v}_{\mathrm{rel}} \equiv \mathbf{v}_2 - \mathbf{v}_1$, as $\mathbf{v}_1 = \mathbf{v}_{\mathrm{cm}} + \mathbf{v}_{\mathrm{rel}}/2$ and $\mathbf{v}_2 = \mathbf{v}_{\mathrm{cm}} - \mathbf{v}_{\mathrm{rel}}/2$. We can then write a general expression for the distribution of relative velocities at a position $\mathbf{x}$,

$$P_{\mathbf{x}}(\mathbf{v}_{\mathrm{rel}}) = \int P_{\mathbf{x}}(\mathbf{v}_1 = \mathbf{v}_{\mathrm{cm}} + \mathbf{v}_{\mathrm{rel}}/2) P_{\mathbf{x}}(\mathbf{v}_2 = \mathbf{v}_{\mathrm{cm}} - \mathbf{v}_{\mathrm{rel}}/2)\, d^3\mathbf{v}_{\mathrm{cm}}. \tag{4.4}$$

The DM relative velocity modulus distribution, $P_{\mathbf{x}}(|\mathbf{v}_{\mathrm{rel}}|)$, is related to the relative velocity distribution, $P_{\mathbf{x}}(\mathbf{v}_{\mathrm{rel}})$ by

$$P_{\mathbf{x}}(|\mathbf{v}_{\mathrm{rel}}|) = v_{\mathrm{rel}}^2 \int P_{\mathbf{x}}(\mathbf{v}_{\mathrm{rel}})\, d\Omega_{\mathbf{v}_{\mathrm{rel}}}, \tag{4.5}$$

where $d\Omega_{\mathbf{v}_{\mathrm{rel}}}$ is an infinitesimal solid angle along the direction $\mathbf{v}_{\mathrm{rel}}$. It is normalized to unity, such that $\int P_{\mathbf{x}}(|\mathbf{v}_{\mathrm{rel}}|) dv_{\mathrm{rel}} = 1$.

To extract the relative velocity modulus distributions for each subhalo, we define spherical shells of width ranging from $[0.1 - 1.0]$ kpc, progressing radially outward from the subhalo center. In each shell, we extract the three components of the velocity vectors, and find the modulus of the pairwise relative velocity distributions for all DM particles in the shell. The bin width of the spherical shells was chosen such that there are at least 10 particles in each shell.

Figure 4.2 shows the DM relative velocity modulus distributions for an example subhalo. The speed distributions are shown in spherical shells of 1 kpc width[1] at different radii from the center of the subhalo, starting from a shell enclosed within $1 < r < 2$ kpc from the subhalo center, and going to a shell with $5 < r < 6$ kpc from the center. The bottom right panel of the figure shows the DM relative speed distribution for all particles in the subhalo. The purple shaded bands specify the 1σ Poisson error in the speed distributions.

Next, we compare the DM relative speed distributions with a MB distribution. In the Standard Halo Model [74], the DM velocity distribution is an isotropic MB distribution with a most probable speed of $\sqrt{2}\sigma$, where σ is the one dimensional velocity dispersion. In this model, the relative velocity distribution $P_{\mathbf{x}}(\mathbf{v}_{\mathrm{rel}})$ is also a MB distribution, but with a one dimensional relative velocity dispersion of $\sqrt{2}\sigma$ [25]. For each subhalo, we find the best-fit MB relative speed distribution,

$$P_{\mathrm{MB}}(|\mathbf{v}_{\mathrm{rel}}|) = \frac{4v_{\mathrm{rel}}^2}{\sqrt{\pi}v_p^3} \, \exp\left(-\frac{v_{\mathrm{rel}}^2}{v_p^2}\right), \tag{4.6}$$

where v_p is the best fit peak speed, i.e. the most probable speed of the DM particles.

Once we have the empirical $P_{\mathbf{x}}(|\mathbf{v}_{\mathrm{rel}}|)$ for each spherical shell in a subhalo, we can find the best fit peak speed, v_p, in eq. (4.6) for each subhalo, by fitting the DM relative speed distributions in each shell to the MB distribution. In figure 4.2 we show the best fit MB speed distribution for each of the six 1 kpc shells as solid black lines. As it is clear from the figure, the MB distribution provides a good fit to the DM relative speed distribution of the simulated subhalo at all radii. Notice that the data shown in figure 4.2 is for a "typical" subhalo analogue and is representative of the

---

[1]We use spherical shells of 1 kpc width in figure 4.2 for clarity of presentation, while in the analysis of the J-factors we use shells of width ranging from $[0.1 - 1.0]$ kpc.
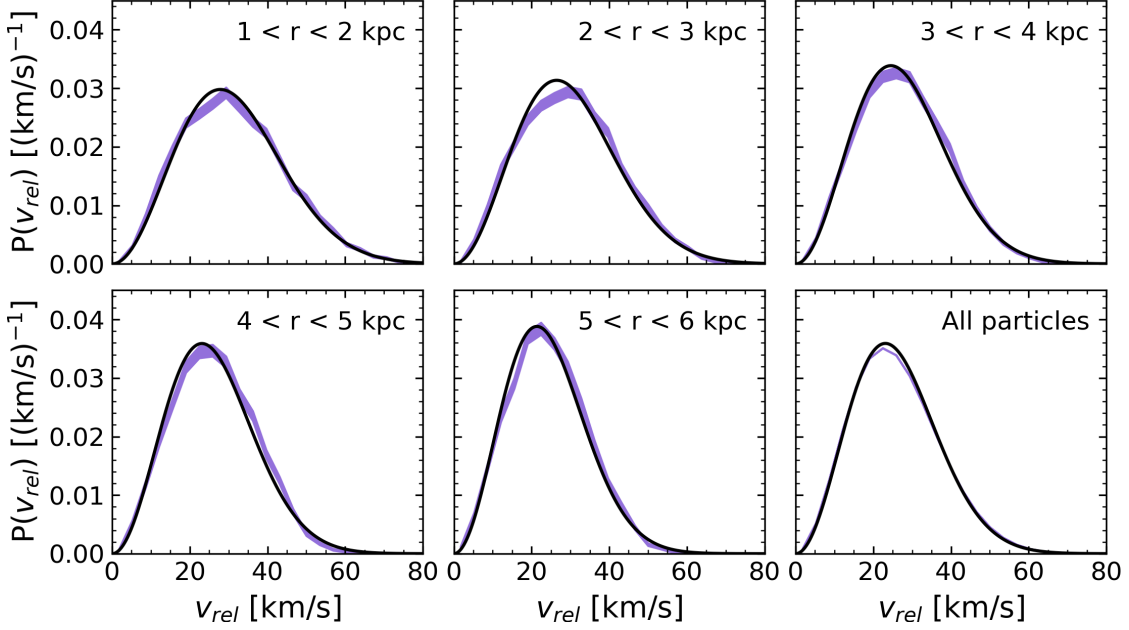
Figure 4.2: The DM relative velocity modulus distribution in 1 kpc shells for a typical subhalo of mass 7.0×10^9 M$_\odot$. The different panels show five different 1 kpc shells, starting from the shell closest to the subhalo center in the upper left, and continuing to the shell furthest from the center in the bottom center panel. The bottom right panel shows the DM relative velocity modulus distribution of all particles in the subhalo. The purple shaded bands specify the 1σ Poisson error in the speed distributions, while the black solid lines show the best fit MB distribution in each case. Reprinted with permission from ref. [4].

DM relative speed distributions of the other simulated subhalos studied in this work.

Another method to determine the best fit peak speed of the MB distribution for each subhalo is to fit the relative speed distribution of all DM particles in the subhalo, instead of dividing it by shells. This process is much more computationally intensive, but provides an excellent check when compared to the mean peak speed found from the results of dividing the subhalo into different shells. Both of these methods lead to a power law relation between the best fit peak speed of the MB distribution and the maximum circular velocity, V_{max}, of the subhalo,

$$v_p = (1.057 \pm 0.016) \left(V_{\mathrm{max}}\right)^{1.052 \pm 0.004} , \qquad (4.7)$$

where v_p and V_{max} are in units of km s^{-1}, and the errors here represent the 1σ error on each fit
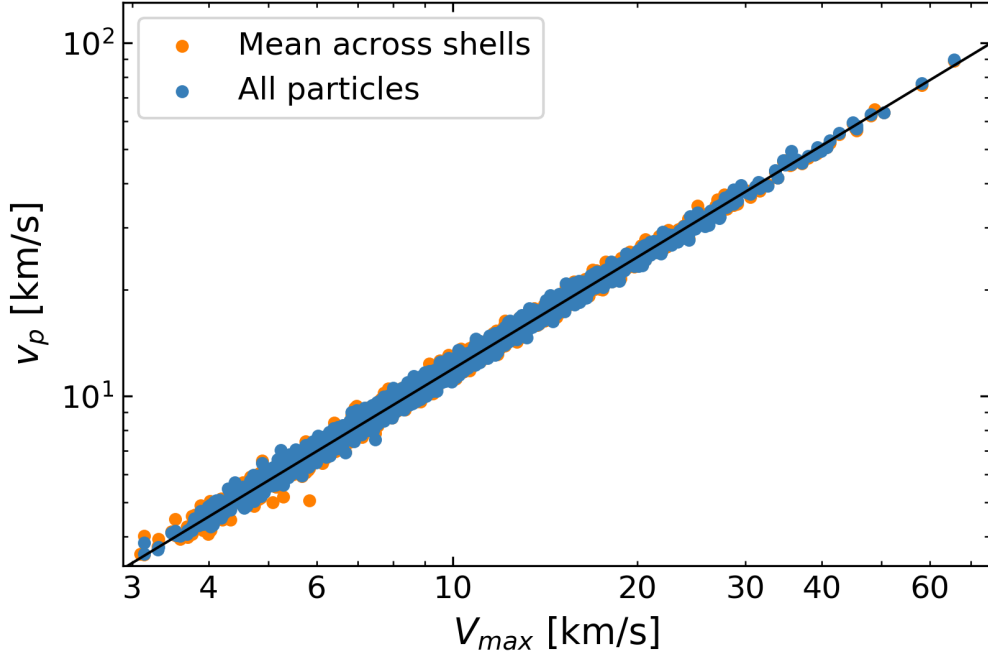
Figure 4.3: The best fit peak speed, v_p, of the MB distribution as a function of the maximum circular velocity, V_{max}, for all selected subhalos in AP-L1 determined by finding the best fit peak speed in different radial shells and taking the mean across all shells (orange dots), or by using a single MB fit across all particles in a subhalo (blue dots). The best fit power law (eq. 4.7) using the orange points is shown as a solid black line. Reprinted with permission from ref. [4].

parameter returned by the LMFIT package for Python.

Figure 4.3 shows the relation between the best fit peak speed of the MB distribution and the maximum circular velocity of the subhalos in AP-L1 using the two methods for determining v_p. The blue points are computed using all the DM particles in the subhalos, and the orange points are computed by first finding the best fit peak speed for different shells, and then taking the mean of the peak speeds across all shells. Also shown in the plot is the best fit power law using the mean of the peak speed shown as a solid line, and quantified in eq. (4.7). The two methods of obtaining the best fit peak speed agree within their 1σ errors.

4.2 $\mathcal{J}$-factors

With the DM density profiles and relative velocity distributions now determined, we can move on to calculating the velocity-dependent $\mathcal{J}$-factors. Here we lay out the formalism for the $\mathcal{J}$-factor

calculation for each of the annihilation cross section models that we consider. The notation closely follows ref. [2].

The DM annihilation cross section, σ_A, averaged over the relative velocity distribution at a spatial location, $\mathbf{x}$, is given by

$$\langle \sigma_A v_{\mathrm{rel}} \rangle(\mathbf{x}) = \int d^3 \mathbf{v}_{\mathrm{rel}} P_{\mathbf{x}}(\mathbf{v}_{\mathrm{rel}})(\sigma_A v_{\mathrm{rel}}). \tag{4.8}$$

In the usual s-wave annihilation, $\sigma_A v_{\mathrm{rel}}$ is independent of the relative velocity. However, for velocity-dependent annihilation models, $\sigma_A v_{\mathrm{rel}}$ depends on the relative velocity and can be parametrized as $\sigma_A v_{\mathrm{rel}} = (\sigma_A v_{\mathrm{rel}})_0 (v_{\mathrm{rel}}/c)^n$. Here $(\sigma_A v_{\mathrm{rel}})_0$ is the velocity-independent component of the annihilation cross section, and n depends on the specific DM annihilation model. We consider the following cases: $n = 0$ (s-wave annihilation), $n = 2$ (p-wave annihilation), $n = 4$ (d-wave annihilation), and $n = -1$ (Sommerfeld-enhanced annihilation).

For the general velocity-dependent annihilation, the expected gamma-ray flux from DM annihilation can then be written as

$$\frac{d\Phi_\gamma}{dE} = \frac{(\sigma_A v_{\mathrm{rel}})_0}{8\pi m_\chi^2} \frac{dN_\gamma}{dE} \mathcal{J}_s, \tag{4.9}$$

where m_χ is the DM particle mass, dN_γ/dE is the gamma-ray energy spectrum produced per annihilation, and $\mathcal{J}_s$ is the effective $\mathcal{J}$-factor defined as [31, 2],

$$\begin{aligned} \mathcal{J}_s(\theta) &= \int d\ell \, \frac{\langle \sigma_A v_{\mathrm{rel}} \rangle}{(\sigma_A v_{\mathrm{rel}})_0} \, [\rho(r(\ell, \theta))]^2 \\ &= \int d\ell \int d^3 \mathbf{v}_{\mathrm{rel}} P_{\mathbf{x}}(\mathbf{v}_{\mathrm{rel}}) \left(\frac{v_{\mathrm{rel}}}{c} \right)^n [\rho(r(\ell, \theta))]^2 . \end{aligned} \tag{4.10}$$

Here ℓ is the distance from the Sun to a point in the dSph (i.e. line of sight), θ is the opening angle between the line of sight ℓ and the distance D from the Sun to the center of the dSph, and $r^2(\ell, \theta) = \ell^2 + D^2 - 2\ell D \cos\theta$ is the square of the radial distance measured from the center of the dSph. This is with the assumption that the dSph is spherically symmetric. The $\mathcal{J}_s$-factor integrated

55

over solid angle is then given by

$$\widetilde{\mathcal{J}}_s(\theta) = 2\pi \int_0^\theta \mathcal{J}_s(\theta') \sin\theta' d\theta'. \tag{4.11}$$

4.3 Results

In this section we present the $\widetilde{\mathcal{J}}_s$-factors of the dSph analogues in AP-L1 for the different velocity-dependent annihilation models. We also quantify the errors introduced in the $\widetilde{\mathcal{J}}_s$-factors if we model the DM relative velocity distribution of the dSph as a MB distribution.

In figures 4.4 and 4.5 we show the $\widetilde{\mathcal{J}}_s$-factors as a function of the opening angle, θ, for a subset of simulated dSphs selected to be analogues of Carina and Sculptor, based on the criteria discussed in section 4.1.1. The four panels of the figures show the $\widetilde{\mathcal{J}}_s$-factors for the four annihilation models. In the s-wave panel, the results are shown using two methods of computing the DM density profiles. In one method the density profiles are directly computed from the simulation data, and in the other method an Einasto fit to the density profiles is used. In the p-wave, d-wave, and Sommerfeld panels, the best fit Einasto density profiles are used, while two methods are employed to compute the DM relative velocity distributions. In one method the velocity distributions are extracted from the simulation data directly, and in the other method the power law relation in eq. (4.7) is used to find the MB peak speed for each dSph analogue from its maximum circular velocity.

We can clearly see from the s-wave panel of figures 4.4 and 4.5 that the $\widetilde{\mathcal{J}}_s$-factors are larger when the best fit Einasto density profile is used. This is due to the empirical density profiles being under-dense in the inner regions of the dSph analogues, which results in smaller $\widetilde{\mathcal{J}}_s$-factors obtained from the simulation data compared to those obtained from the Einasto profile. It is also clear from the other panels of the figures that modelling the DM relative velocity distribution using a MB distribution introduces a degree of error into the $\widetilde{\mathcal{J}}_s$-factors in all three velocity-dependent models, which depends on the specific model. Nevertheless, for all three velocity-dependent models, the errors introduced in the $\widetilde{\mathcal{J}}_s$-factors due to the MB modelling of the velocity distributions are much smaller than the errors introduced due to using the under-dense empirical density profiles.
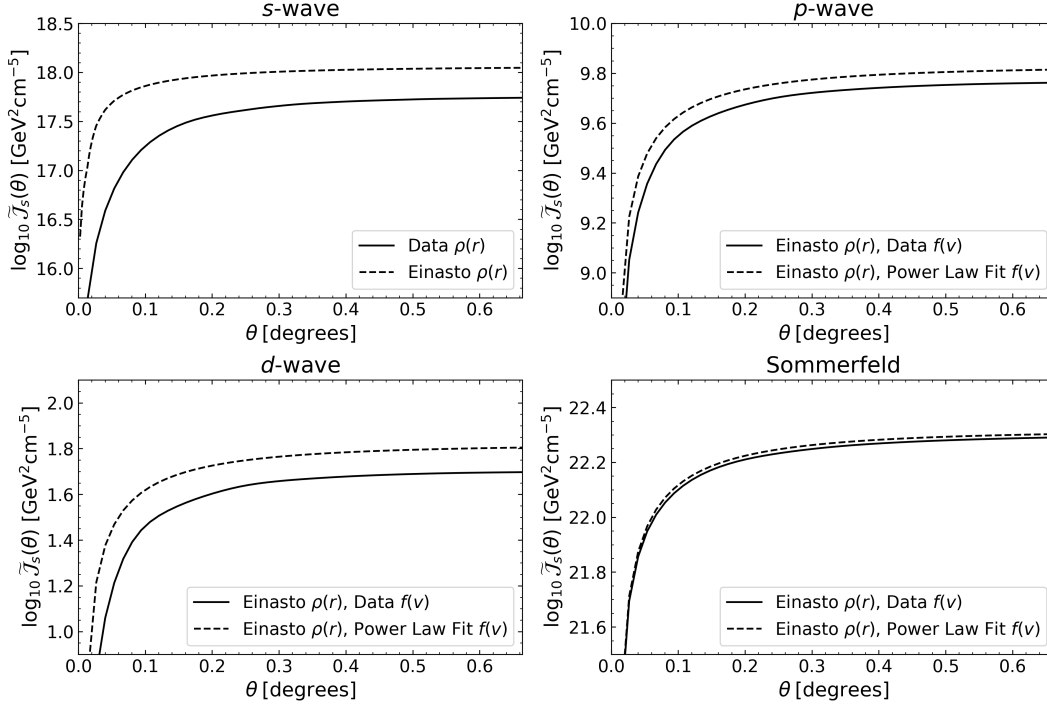
Figure 4.4: $\widetilde{\mathcal{J}}_s$-factor for one Carina dSph analogue in AP-L1 for the s-wave (top left), p-wave (top right), d-wave (bottom left), and Sommerfeld (bottom right) annihilation models. In the s-wave panel, the solid and dashed lines represent using the empirical and an Einasto fit to the DM density profile, respectively, for the $\widetilde{\mathcal{J}}_s$-factor calculation. In the p-wave, d-wave, and Sommerfeld panels, the solid and dashed lines represent using the empirical DM relative velocity distribution and a MB distribution with a peak speed determined from the power law relation in eq. (4.7), respectively. Reprinted with permission from ref. [4].

We can quantify more precisely the error introduced in the $\widetilde{\mathcal{J}}_s$-factors if we model the relative velocity distribution of the dSph as a MB distribution. For this, we compare the $\widetilde{\mathcal{J}}_s$-factor of all subhalos using the DM relative velocity distributions extracted from the simulation data with those computed using (a) the best fit MB velocity distribution in different radial shells, (b) the best fit MB distribution for all particles in the subhalo, (c) a MB distribution with a peak speed set to the mean of the best fit MB peak speeds across all radial shells, and (d) a MB distribution with a peak speed found using eq. (4.7). The ratios of the $\widetilde{\mathcal{J}}_s$-factors obtained directly from the simulation data to those computed from a MB velocity distribution, $\widetilde{\mathcal{J}}_s^{\mathrm{MB}}$, using each of the above methods are shown in figure 4.6 for the p-wave, d-wave, and Sommerfeld models.

We can see from figure 4.6 that fitting a MB distribution in each radial shell minimizes the
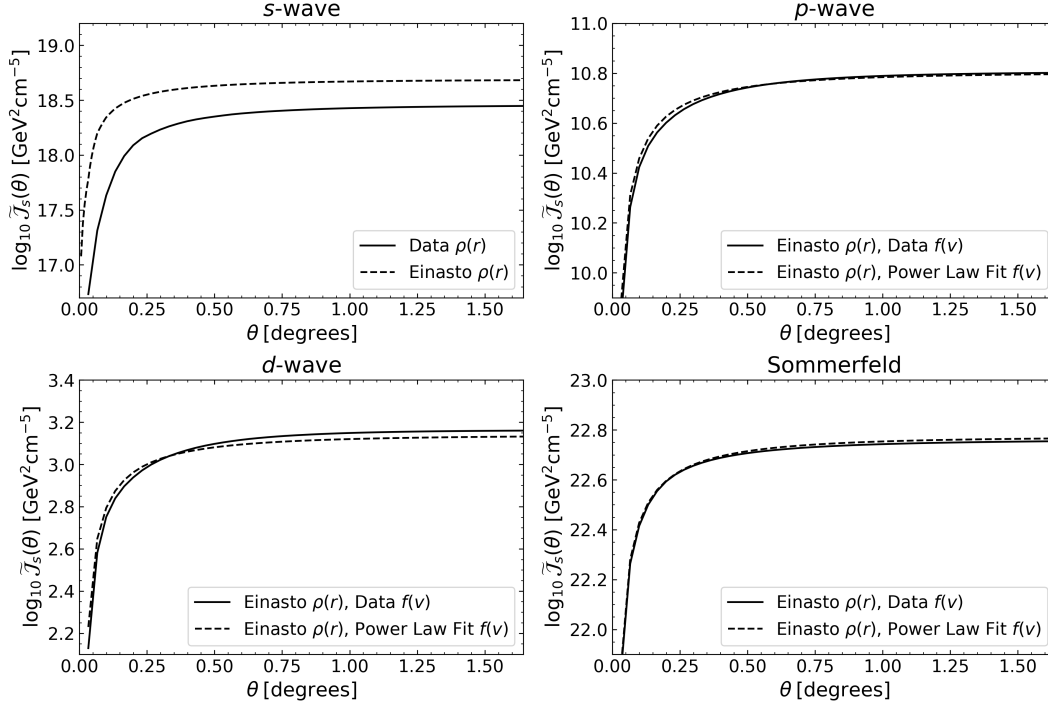
Figure 4.5: Same as figure 4.4 but for one Sculptor dSph analogue in AP-L1. Reprinted with permission from ref. [4].

error for all annihilation models. The errors introduced by the other three methods are similar to each other, especially for the p-wave and Sommerfeld models. In table 4.2, we quantify the errors introduced in the $\widetilde{\mathcal{J}}_s$-factors using all four methods for computing the velocity distribution. At high V_{max}, we find that fitting a MB distribution in each radial shell introduces an average error of 1.06-1.70%, using the best fit MB distribution for all particles in a subhalo introduces an average error of 2.17-6.50%, using the mean of MB fits across all radial shells introduces an average error of 2.45-5.91%, and using a MB distribution from eq. (4.7) introduces an average error of 2.93-14.86% for the velocity-dependent annihilation models. We find that the average percent error increases at lower V_{max} for all annihilation models. We also find that the average percent errors are generally smaller for the Sommerfeld model in each method of calculation.

We note that the computational time saved using a MB distribution with a peak speed found from the power law fit (eq. (3.7)) to model the relative velocity distribution rather than extracting it from the simulation data directly is substantial. In particular, we found that for our subset of

58
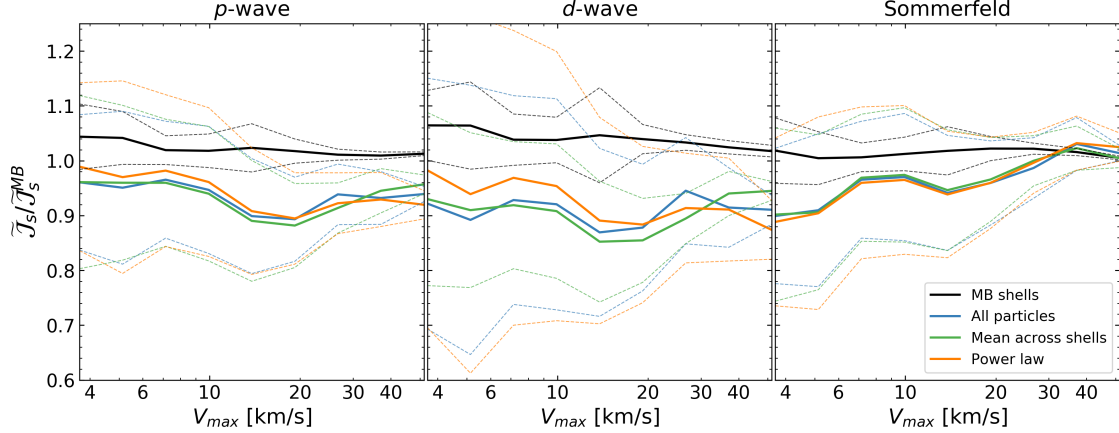
Figure 4.6: The ratio of the $\widetilde{\mathcal{J}}_s$-factors obtained from the empirical DM relative velocity distributions and those found from fitting a MB distribution: in different radial shells (black), to all particles in the dSph (blue), using the mean peak speed found from the best fit MB peak speeds across all shells (green), and using the peak speed found from eq. (4.7) (orange). The solid lines show the mean ratios as a function of the dSph's maximum circular velocity, while the dashed lines show the upper and lower 1σ uncertainties. The left, middle, and right panels show the results for the p-wave, d-wave, and Sommerfeld models, respectively. Reprinted with permission from ref. [4].

subhalos selected from the AP-L1 simulations, the time it takes to compute the $\widetilde{\mathcal{J}}_s$-factors using the empirical data is $\sim 20,000$ times longer than the time it takes to compute them using the MB distribution.

Next, we compare our $\widetilde{\mathcal{J}}_s$-factor results to those recently found in the literature for specific dSphs [6]. In figure 4.7, we show the comparison of our $\widetilde{\mathcal{J}}_s$-factors for nine dSph analogues obtained using the simulation data directly and using a MB velocity distribution with a peak speed obtained from the power law fit, with those presented in figure 1 of ref. [6]. The $\widetilde{\mathcal{J}}_s$-factors in ref. [6] are calculated using eq. (4.10), integrated over cones with various opening half-angles. We choose to compare to the $\widetilde{\mathcal{J}}_s$-factors integrated over a cone with an opening half-angle of $0.5°$, simply because all the dSph analogues are extended out at minimum to $0.5°$, but not to the the next data point of $10°$. Furthermore, to compare our results to those of ref. [6], we compute our $\widetilde{\mathcal{J}}_s$-factors by positioning the simulated dSph analogues at the same galactocentric distance as their observed dSph counterparts, obtained from ref. [96].

	MB Shells	All particles	Mean across shells	Power law
p-wave	[4.14, 1.25]	[11.24, 6.50]	[12.16, 4.54]	[13.25, 8.82]
d-wave	[5.99, 1.70]	[24.04, 9.92]	[25.30, 5.91]	[26.38, 14.86]
Sommerfeld	[2.00, 1.06]	[12.90, 2.17]	[13.90, 2.45]	[14.43, 2.93]

Table 4.2: The average percent error of the $\widetilde{\mathcal{J}}$-factors of each method of calculation for the velocity-dependent annihilation models. Shown are the average percent errors for subhalos with $3.09 \leq V_{\max} \leq 4.30$ km/s (left numbers in the intervals) and subhalos with $43.16 \leq V_{\max} \leq 60.0$ km/s (right numbers in the intervals). Reprinted with permission from ref. [4].

In ref. [6] a Navarro-Frenk-White (NFW) profile was used to model the density profiles of the dSphs, and the DM velocity distributions were assumed to be related to the density profiles by the Eddington inversion formula [100]. This approach assumes that the DM halo is in equilibrium with a spherically symmetric potential, and that the DM has isotropic orbits. For comparison, in this work, we use the best fit Einasto density profiles for the simulated dSphs. The DM relative velocity distributions are obtained directly from the cosmological simulations, and we also compare the results to those obtained from modeling the velocity distributions as a MB distribution. These represent the primary differences in our approach and the approach used in ref. [6]. In appendix C, we also present the $\widetilde{\mathcal{J}}_s$-factors for the nine dSph analogues using their best fit NFW density profiles, and compare them to the results of ref. [6].

As we can see in figure 4.7, our results generally agree with ref. [6]. In particular, for each of the observed dSphs shown in figure 4.7, the average $\widetilde{\mathcal{J}}_s$-factor over the different simulated dSph analogues is roughly on the same order of magnitude as those of ref. [6] for each annihilation model, and show no systematic trends when compared to ref. [6]. We also see that in general the subhalo-to-subhalo scatter is largest for d-wave and smallest for the Sommerfeld model. This trend is similar to the results obtained for the smooth halo in ref. [2].

4.4 Discussion and Conclusions

In this dissertation we have presented a systematic study of the velocity-dependent DM annihilation signals from dwarf spheroidal galaxy analogues in the APOSTLE cosmological simulations. We extract the DM density and pair-wise relative velocity distributions of the simulated dwarf
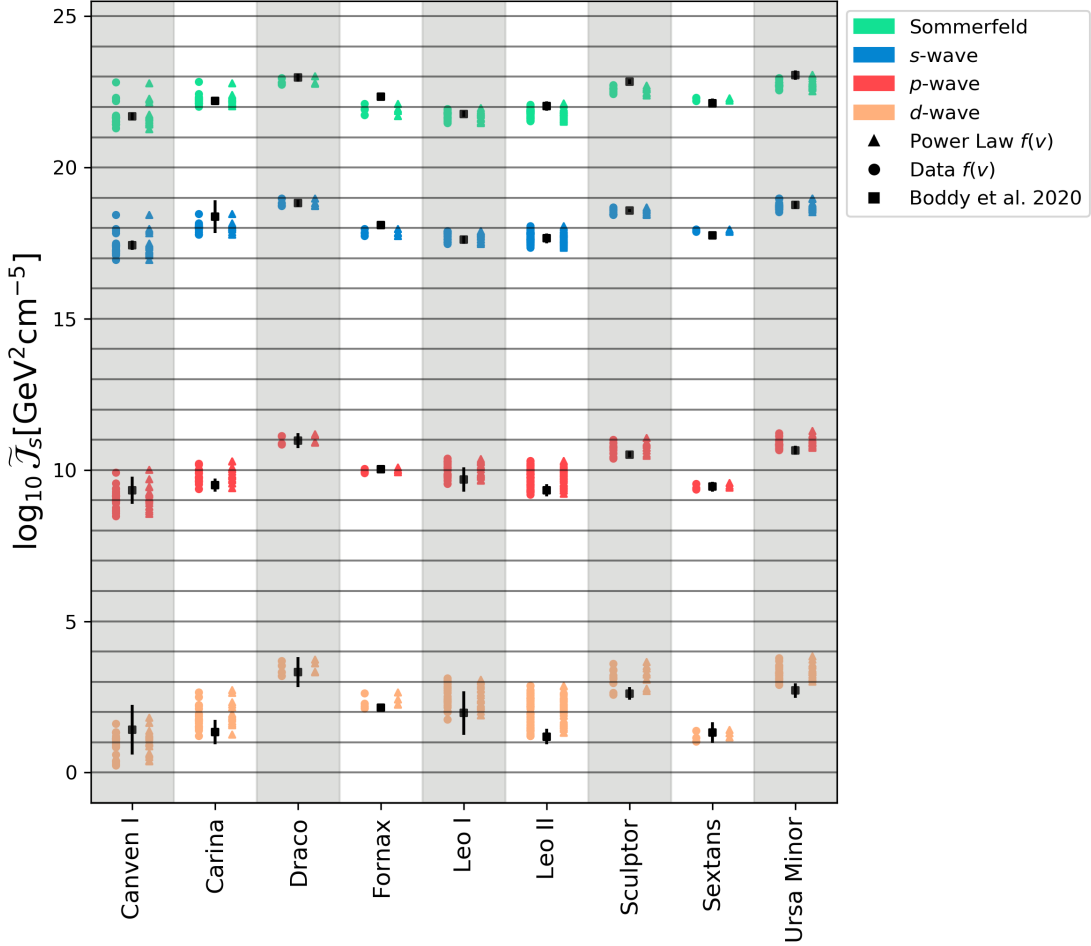
Figure 4.7: Integrated $\widetilde{\mathcal{J}}_s$-factors over cones with opening half-angles of $0.5°$ for nine dSph analogues for the s-wave (blue), p-wave (red), d-wave (orange), and Sommerfeld (green) models. The the $\mathcal{J}$-factors are calculated using the DM relative velocity distributions found empirically (circle), using a MB distribution with a peak speed from the power law in eq. (4.7) (triangle), and comparing to the data in ref. [6] (square). Reprinted with permission from ref. [4].

spheroidal analogues to compute the $\mathcal{J}$-factors in the s-wave, p-wave, d-wave, and Sommerfeld annihilation models. We also quantify the error introduced in the $\mathcal{J}$-factors if we model the DM relative velocity distribution as a Maxwell-Boltzmann distribution.

We find a good agreement between the DM relative velocity distributions of the dwarf spheroidal analogues extracted from the simulations and their best fit Maxwellian distribution at all radii. As a result, the error introduced in the $\mathcal{J}$-factors from using the best fit Maxwellian distributions in different radial shells within a dwarf spheroidal analogue is on average 2.7% for the three velocity-

dependent models. This error increases to 10.7% if we use a Maxwellian distribution with a peak speed set to the mean of the best fit Maxwellian peak speeds across all radial shells in a dwarf spheroidal analogue. If instead, we use all the DM particles in a dwarf spheroidal analogue to find the best fit Maxwellian distribution, the error is slightly increased to 11.1%. We also find that the latter two methods of determining the best fit peak speed of the Maxwellian distribution by using either all the DM particles in the dwarf spheroidal analogue or by finding the mean of the best fit peak speeds at different radii, lead to a power law relation between the best fit peak speed and the maximum circular velocity of the dwarf spheroidal analogue (i.e. eq. (4.7)). Using this power law to compute the $\mathcal{J}$-factors substantially reduces the computation time, and introduces on average a 13.4% error.

We have investigated the effects of modelling the DM density profile of the dwarf spheroidal analogues using an Einasto profile. We find that the difference between the $\mathcal{J}$-factors calculated directly from the simulation data and those calculated from the best fit Einasto profiles is much larger than the error introduced in the calculations due to modeling the DM relative velocity distributions with a Maxwell-Boltzmann distribution. The large differences in the two density profiles originate from the resolution of the simulations which results in the empirical density profiles being under-dense in the inner regions of the dwarf spheroidal analogues compared to the Einasto profile.

We also find that the systematic uncertainties introduced in the integrated $\mathcal{J}$-factors by using different analogues of the same observed dwarf spheroidal in the simulations is in general larger than the error introduced by modeling the relative DM velocity distributions as a Maxwell-Boltzmann distribution. Additional systematic uncertainties can also be introduced by using different models for the DM density profiles, such as the NFW profile and its cored versions, or by breaking the assumption of spherically symmetric profiles. Also, it may be necessary to include substructure within the dSph analogues, and quantify the difference in their contributions for the different velocity-dependent models. This mass function for these sub-subhalos has been quantified in the higher resolution DMO Aquarius simulations [101], but not for the simulations

considered in this analysis. At this stage, a detailed analysis of such uncertainties is beyond the scope of this work.

Finally, we compare our results to those found in the literature for specific dwarf spheroidal galaxies. We find that our integrated $\mathcal{J}$-factors are generally in good agreement with those presented in previous work, which uses simplified models for the DM velocity distributions of the dwarf spheroidals [6]. The simulations we use in this dissertation do not force strict model assumptions on the velocity distribution. As a result, we specifically show that the halo-to-halo scatter in the $\mathcal{J}$-factors dominate the astrophysical uncertainties, with the largest scatter for the d-wave models and the smallest for the Sommerfeld models. Such a scatter is likely to have important implications for bounds on the DM annihilation cross section that have been obtained in previous studies [18].

5. VELOCITY-DEPENDENT $\mathcal{J}$-FACTORS FOR M31 IN COSMOLOGICAL SIMULATIONS

At the time of publication of this dissertation, the work discussed in this chapter is currently in progress. Please see more a recent publication by Vienneau et al. for the most updated figures and results.

In this work, we extract the DM density and relative velocity distributions of M31 from the APOSTLE Level 1 hydrodynamical simulations [37, 38], and compute the $\mathcal{J}$-factors for the simulated M31 galaxies for the s-wave, p-wave, d-wave, and Sommerfeld models. We compare the results to the $\mathcal{J}$-factors for the MW foreground and external sources.

5.1 Selection of M31-Like Galaxies

We use APOSTLE Level 1 volumes to examine M31-like analogues. Each APOSTLE volume contains two main galaxies, a MW-like and an M31-like galaxy. In this work, we consider both main halos in each of the five Level 1 volumes, to give us a total of 10 M31-like analogues.

In each volume, we define the Solar position at 8.0 kpc from the galactic center of one of the main halos, making sure that the other main halo appears at the galactic longitude and latitude values of the observed M31. To include the contributions from foreground and background dwarf galaxies, we do not impose any distance restrictions on the DM particles in which we consider.

5.2 Properties of the Simulated Volumes

In this section, we discuss the dynamical properties of the DM halos that are most important for our analysis. We focus specifically on the DM density profiles and the relative DM velocity distributions. These properties are then used in the subsequent sections to calculate the $\mathcal{J}$-factors.

As in section 3.2, we separate our $\mathcal{J}$-factor calculations into contributions from the smooth DM halo and contributions from DM subhalos. Also, for the purposes of our analysis, we further separate the contributions from M31, the MW foreground, and other external sources.

5.2.1 DM Density Profiles

We now move on to characterizing the DM density profiles of the halos. Characterizing the density profiles is important since they enter into the calculation of the DM annihilation rate through the $\mathcal{J}$-factor.

Unlike in our previous studies of DM annihilation in simulations, we assume that the DM density profile is not spherically symmetric. This is because M31 is an extended source on the sky and contains a non-uniform distribution of substructure. Following ref. [5], we apply a Voronoi tesselator to estimate the DM distribution in the entire volume, allowing the calculation of ρ_i from the DM particle mass and the cell volume surrounding the i-th DM particle. This approach provides a better localized measure of the DM density than other estimates which smooth over a particle's nearest neighbors [87], as discussed in previous sections. We can use the local DM density profile in our calculations for the $\mathcal{J}$-factors.

5.2.2 Relative Velocity Distribution

For velocity-dependent annihilation models, the $\mathcal{J}$-factors depend not only on the DM density profile, but also on the DM pair-wise, or relative velocity distribution of the DM particles. We now describe how we extract the DM relative velocity distributions at the location of each DM particle.

Previously, we assumed the relative velocity distributions to be spherically symmetric, and thus we calculated the relative velocity distributions in spherical shells. Now, we will not assume spherical symmetry due to the reasons discussed above. At the location of each DM particle, we take the nearest 500 DM particles and calculate the pair-wise relative velocity of each particle. We find that the local DM relative velocity distribution can still be well approximated by a MB distribution. The relative velocity distributions are then used in eq. (3.7) to obtain $\mu_n(\mathbf{x})$ for each annihilation model at the location of each DM particle. We can now use the velocity moments to calculate the $\mathcal{J}$-factors.

5.3 Results

To calculate the $\mathcal{J}$-factors, we need the DM density and the DM relative velocity distribution. Using the Voronoi tessellation method described above, we estimate the local DM density at the location of each DM particle. Then we calculate the relative velocity distribution at the location of each DM particle, and obtain $\mu_n(\mathbf{x})$ for each annihilation model. We then compute the integral in eq. (3.8) over each volume produced by the Voronoi Tessellation, normalized by the angular size, to obtain the $\mathcal{J}$-factors.

5.3.1 $\mathcal{J}$-factors

In this section we present the preliminary results of our analysis. We begin by comparing the contribution to the $\mathcal{J}$-factors from DM subhalos to that of the DM smooth halo in the simulations. We then compare the contribution to the $\mathcal{J}$-factors from the MW foreground and external sources to that from M31. Additionally we compare our results of the s-wave annihilation radiation from M31 to the analytic models in ref. [94].

Figure 5.1 shows the results for one M31-like galaxy for each considered annihilation model as seen from the Solar position. The extended emission from the smooth DM halo is noticeable in all annihilation models. The contribution from subhalos is greatest for the Sommerfeld and s-wave annihilation models. As found in ref. [3], the DM annihilation radiation from subhalos is not significant in p-wave and d-wave annihilation models.

Figure 5.2 shows the ratio of $\mathcal{J}$-factors from M31 to that of the combined contribution from MW foreground and external sources for the same M31-like galaxy shown in figure 5.1 for each considered annihilation model as seen from the Solar position. The extended emission from the smooth DM halo of M31 is dominant in all annihilation models. In the case of Sommerfeld and s-wave annihilation models, we find that the annihilation radiation from DM subhalos dominate over that of the smooth DM halo component.

Figure 5.3 shows the $\mathcal{J}$-factors for all 10 M31-like halos for Sommerfeld (red), s-wave (blue), p-wave (yellow), and d-wave (green) annihilation models. The solid lines show the annihilation
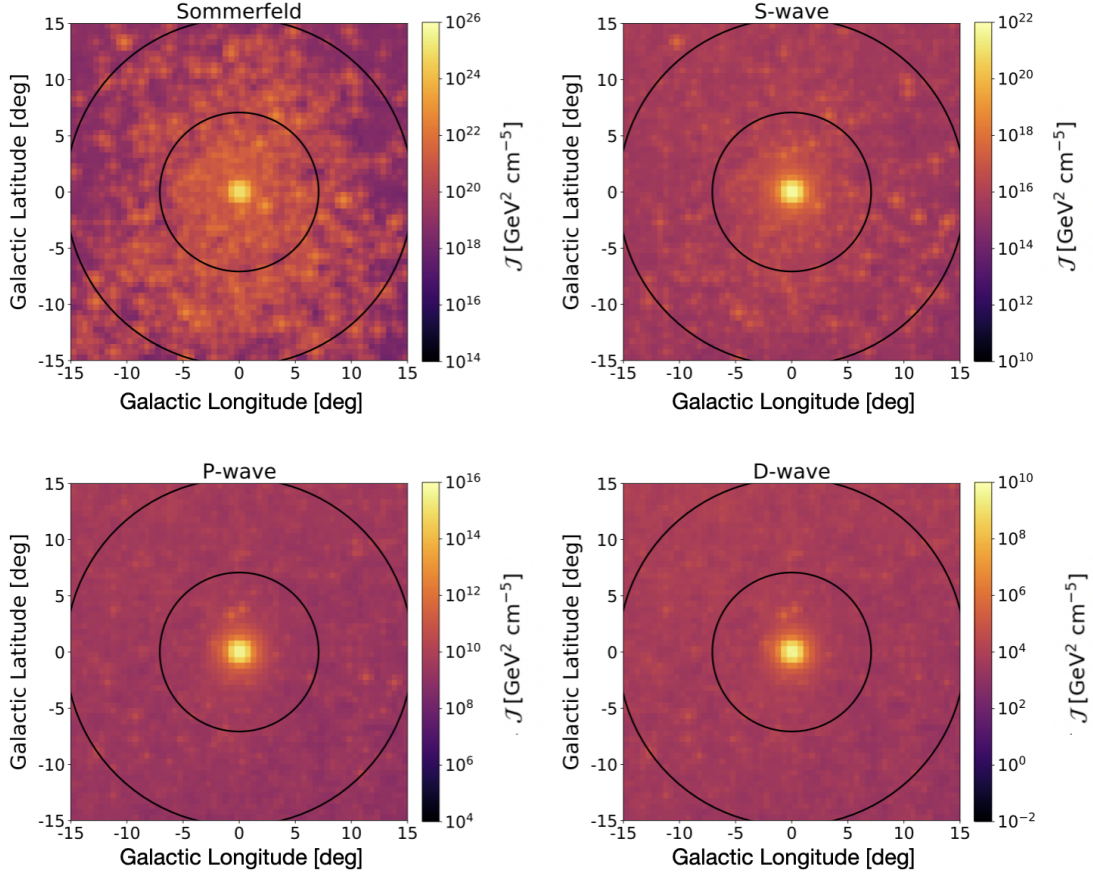
Figure 5.1: $\mathcal{J}$-factors for one M31-like galaxy for each considered annihilation model as seen from the Solar position. The concentric black circles represent r_{200} and $2r_{200}$ of the halo. The extended emission from the smooth DM halo is noticeable in all annihilation models. The contribution from subhalos is greatest for the Sommerfeld and s-wave annihilation models.

radiation from M31 while the dashed lines show the MW foreground annihilation. The horizontal axis shows the angle from the center of M31 for the line-of-sight. At each angle we spherically average the $\mathcal{J}$-factors, so that we can include the contribution from DM subhalos. We find that in the case of s-wave annihilation, our results agree with that of ref. [7].

5.3.2 Fermi Analysis

We are currently working to implement our $\mathcal{J}$-factor results from DM simulations into Fermi modeling software. we perform a binned likelihood analysis assuming an extended spatial profile
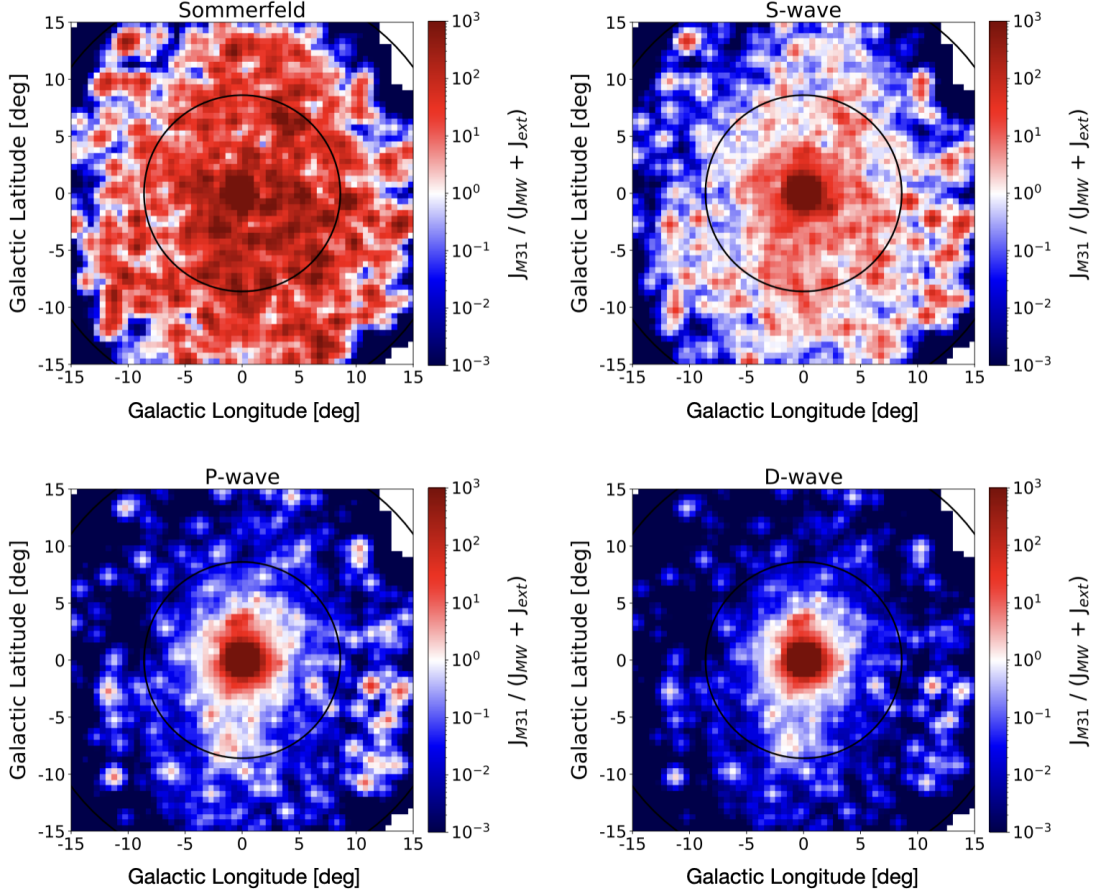
Figure 5.2: The ratio of $\mathcal{J}$-factors from M31 to that of the combined contribution from MW foreground and external sources for one M31-like galaxy for each considered annihilation model as seen from the Solar position. The concentric black circles represent r_{200} and $2r_{200}$ of the halo. The extended emission from the smooth DM halo of M31 is dominant in all annihilation models. In the case of Sommerfeld and s-wave annihilation models, we find that subhalos dominate over the smooth component.

for the source based on our templates, centered on M31, using the Fermitools 2.0.8.[1] We utilize FermiPy [102], which is a Python-based software package that automates the tools for Fermi-LAT source analysis.

We consider the $30° \times 30°$ region of interest (ROI) centered on M31 as shown in figure 5.1. We input a background source model using the MW foreground annihilation signals from each simulation. Each of the ten instances of the simulations and each of the four annihilation models

---

[1]https://github.com/fermi-lat/Fermitools-conda/wiki
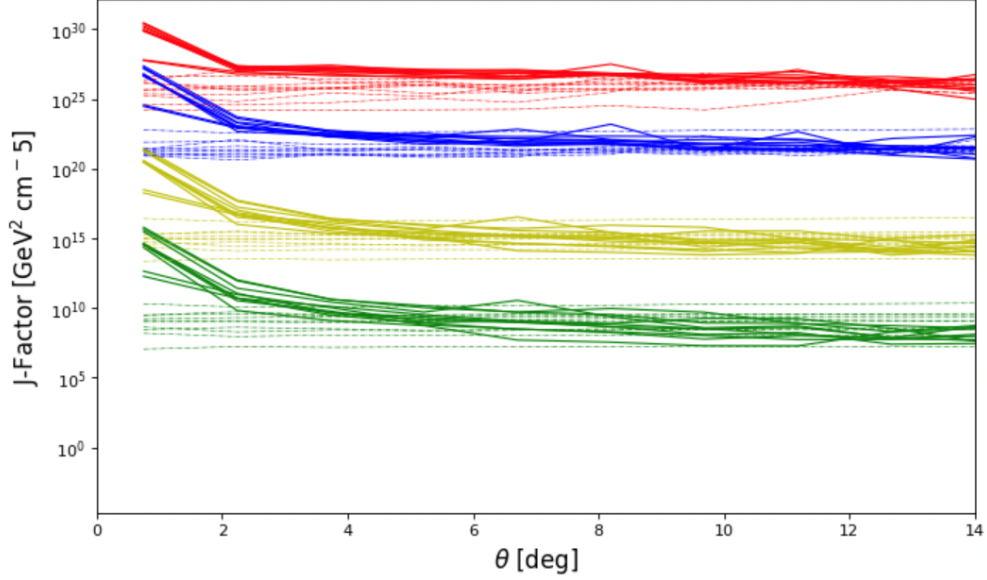
Figure 5.3: The $\mathcal{J}$-factors for all 10 M31-like halos for Sommerfeld (red), s-wave (blue), p-wave (yellow), and d-wave (green) annihilation models. The solid lines show the annihilation radiation from M31 while the dashed lines show the MW foreground annihilation. The horizontal axis shows the angle that the line-of-sight makes from the center of M31. At each angle we spherically average the $\mathcal{J}$-factors. We find that in the case of s-wave annihilation, our results agree with that of ref. [7].

are considered separately in this analysis.

In a general FermiPy analysis, one defines the model sources within the ROI and then performs multiple likelihood tests to determine the best-fitting parameters of the model sources. Following ref. [103], we define the Test Statistic (TS) as $\mathrm{TS} = -2\ln(\mathcal{L}_0/\mathcal{L}_1)$ where $\mathcal{L}_0$ represents the likelihood of the null hypothesis and $\mathcal{L}_1$ represents the likelihood of the alternative.

We have not yet obtained definitive results from the FermiPy analysis, but we anticipate that the results will show a significant annihilation signal from the smooth DM component of M31 in all annihilation models. We expect to see a significant contribution to the DM annihilation signals in the Sommerfeld and s-wave annihilation models. We also expect that the results of the analysis will provide strict limits on the annihilation cross section of DM particles in the simulations.

5.4 Discussion and Conclusions

In this dissertation we have presented a systematic study of the velocity-dependent DM annihilation signals from M31 analogues in the APOSTLE cosmological simulations. We extract the local DM density and the pair-wise relative velocity distributions of M31, the MW foreground, and external sources to compute the $\mathcal{J}$-factors in the s-wave, p-wave, d-wave, and Sommerfeld annihilation models. We find that the extended emission from the smooth DM halo dominates over the emission from the MW foreground and external sources in all annihilation models. As in section 3.4, we find that substructure is the most significant in Sommerfeld and s-wave models, while it is the least significant in p-wave and d-wave models.

We compare our results to that of ref. [7], which utilizes a spherically-symmetric analytic approach to the calculation of the $\mathcal{J}$-factors. We find that for the s-wave DM annihilation model, the $\mathcal{J}$-factors from M31 and the MW foreground in simulations are in good agreement with the analytic estimations. We note that the halo-to-halo scatter for M31 $\mathcal{J}$-factors is smallest in the Sommerfeld and largest in the d-wave annihilation model.

Currently we are working to implement the velocity-dependent $\mathcal{J}$-factors of M31 in a FermiPy analysis.

The work in this chapter is still currently in progress by Evan Vienneau, Addy Evans, Louis Strigari, and Nassim Bozorgnia.

6. 3D MODELING OF THE INTERSTELLAR MEDIUM OF THE MILKY WAY

At the time of publication of this dissertation, the work discussed in this chapter is currently in progress. Please see more a recent publication for the most updated figures and results.

6.1 Motivation

The objective of this project is to provide a cohesive "big picture" view of the dynamical interactions between CRs and the other parts of the diffuse ISM through developing detailed data-driven models of the interstellar gas, radiation and magnetic fields, and CRs in the MW. These models will be used to investigate the deep connections between important properties related to the evolving ISM: the CR heating and pressure, the radio/IR/γ-ray relation, the spatial distribution of the diffuse ultraviolet (UV) through far-IR (FIR) radiation (the interstellar radiation field – (ISRF)), and the spatial distribution of CO and its relationship to H_2 through the often used X_{CO} parameter.

The ISRF modeling uses empirical luminosity functions (LFs) and density profiles for the stellar spectral content of the different geometric components (disk, arms, etc.). Because we are not studying the dynamical and stellar evolutionary history this is the most practical approach for characterizing the stellar populations at the present day.

Of particular importance is the LF and profile of OB stars, because these stars provide heating of dust nanograins that emit prominently in the mid-infrared, and the OB stars are candidates for tracing the CR sources, if not actual sources themselves [104, 105]. Dust heating from the strong UV from these stars produces warmer emissions, so better characterization of their spatial distribution enables the most accurate separation of the warm and cooler FIR-emitting dust; the latter is mainly due to heating by the longer wavelength component of the ISRF in the ISM.

Density profiles for late-type stars have been measured by several authors over the years [106, 107], and most recently using *Tycho-Gaia Astrometric Solution* (TGAS)/*Gaia* DR1 [108]. However, the density for OB stars has not been studied in great detail. The LFs for these stars for the

R12/F98 ISRF models are based on limited statistics, from studies in the 1980/90s [109, 110, 111] and Hipparcos observations [112, 113].

A catalog of approximately 5000 OB stars has been compiled using *Gaia* DR2 [114]. Combined with the Hipparcos data we intend to utilize this sample of OB stars with a Bayesian analysis [115] to tightly constrain the OB-star distribution vertical scale height. Ref. [108] finds from TGAS the scale height for A-type stars is ~ 50 pc, increasing to ~ 100 pc for later types. A direct empirical estimate of the OB star scale height will be an important input also into our CR source models.

Determining the OB star number density requires a measurement of the selection function in order to correct for incompleteness. Using DR1 [108] estimates the selection function for late-type stars by cross-matching TGAS with the 2MASS catalog. For DR2, we are also able to compare to 2MASS to estimate the selection function [116]. In addition to the OB star number density we will be able to better determine the number density for all other stellar types, providing the most tightly constrained LFs and corresponding improved accuracy of the ISRF over all wavelengths.

The outcome will be an optimized 3D ISRF model with self-consistently determined structural parameters for the major stellar and dust components. Our work will provide the best model of the full 3D spectral intensity spatial distribution from UV-to-FIR for the MW, which is necessary for accurate calculation of CR electron/positron energy losses and the IC γ-ray production from the interstellar emissions. Our new model will also provide the most detailed description for the IR photon density and dust temperature distribution across the Galaxy over different spatial scales.

6.2   Selection of OB Stars in *Gaia* DR3

Gaia DR3 has astrometry and photometry for an incredible 1,811,709,771 sources. However, we are only interested in a subset of these stars to include in the calculations for our model. In this section we will discuss the selection of O and B stars in *Gaia* DR3.

For our completeness model, we select stars which have been reliably detected by *Gaia* [1]. We only consider stars which satisfy the following quality cuts: PHOT_G_MEAN_MAG $<= 20$, ASTROMETRIC_MATCHED_TRANSITS $>= 5$, ASTROMETRIC_EXCESS_NOISE $<= 20$,

72

PARALLAX_OVER_ERROR >= 10. See appendix D for the query used to select O and B stars from the *Gaia* catalogue. We further reduce our subset of stars by performing a parallax cut, so that we only consider stars within a distance of 4.2 kpc. This ensures that our entire region of interest for the 3D ISRF model will be encompassed by the 3D completeness model. This process gives us 966,707 B type and 170,660 O type stars to consider.

6.3   Completeness Model

Comparing model predictions to observations from an astronomical catalogue requires knowledge of the selection effects and incompleteness affecting the observed objects. Knowing what we could not observe is as important as knowing what we could observe, especially for creating a model based on our observations.

A catalogue selection function describes the probability of an object to be included in an astronomical catalogue. This selection function represents the combined the effects of data collection and data processing. The most common approach to estimate a catalogue selection function of a sample is to compare to a more complete catalogue [117, 108, 118]. This approach is easy to understand and implement, but does require that the comparison catalogue truly is complete.

To calculate the completeness of the *Gaia* catalogue you would need a different method of calculation because there currently is no catalogue which is more complete than the *Gaia* catalogue. Ref. [1] provides empirical calculations of the completeness function of the *Gaia* catalogue. This approach requires modeling each step of the *Gaia* processing, from the scanning law and onboard filtering to the astrometric processing. We use the Gaiaverse[1] selection function established in ref. [1] to estimate the completeness of our sample of OB stars.

6.4   Results

Once we have obtained the subset of OB stars that satisfy the conditions outlined in section 6.2, we then calculate a 2D and 3D completeness model. Utilizing the Gaiaverse selection function Python package [1], we estimate the completeness of O and B type stars separately. We query

---

[1]https://github.com/gaiaverse/selectionfunctions
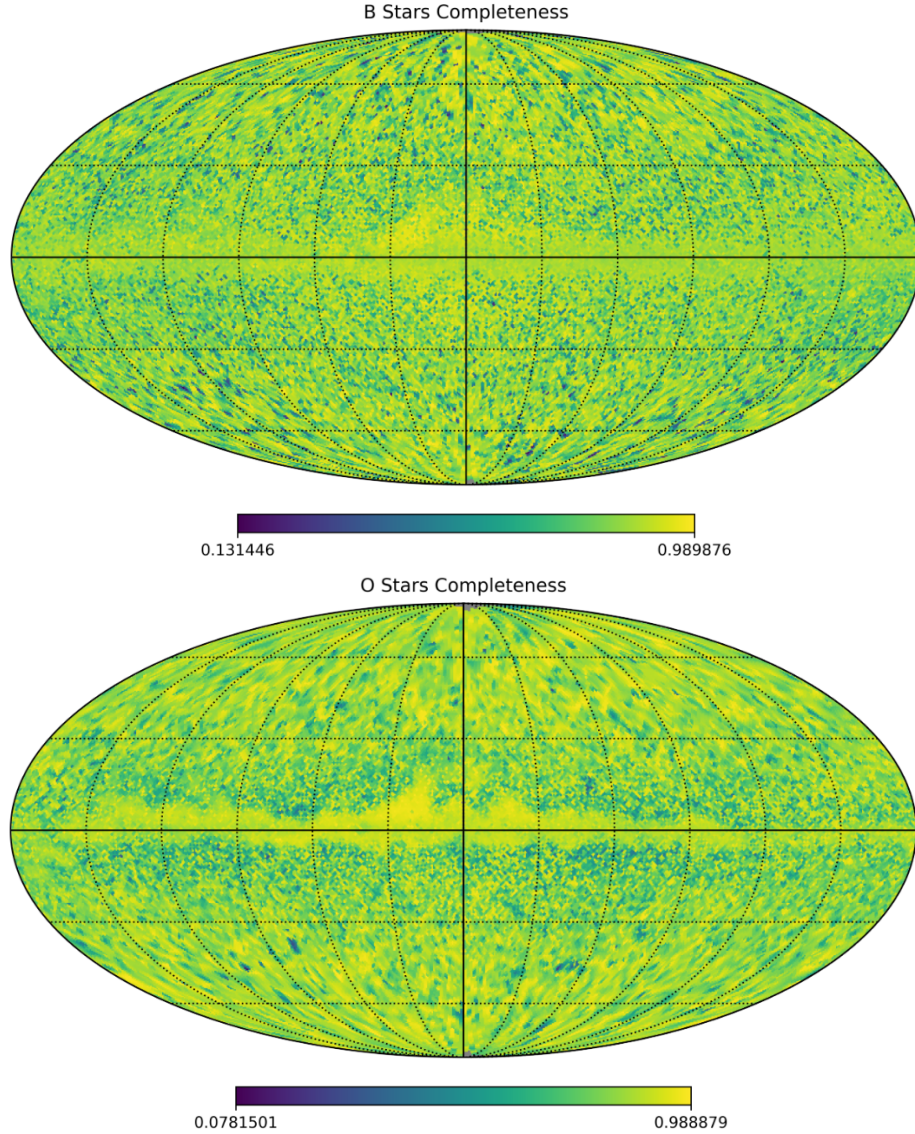
Figure 6.1: All-sky map of the average completeness of B stars (top) and O stars (bottom) along the line of sight out to 4.2 kpc.

the selection function with only one type of star, which provides an estimate for the completeness at the location of each star. Using HEALPix to establish bin locations on the sky, we sort the stars into corresponding bins. To create a 2D completeness model on the sky, we average the completeness of O stars and B stars separately in a given HEALPix bin. We then extend our completeness model to 3D by utilizing the parallaxes assigned by *Gaia*, which is why we require precise parallax measurements of our OB sample. For O and B stars separately, we calculate the
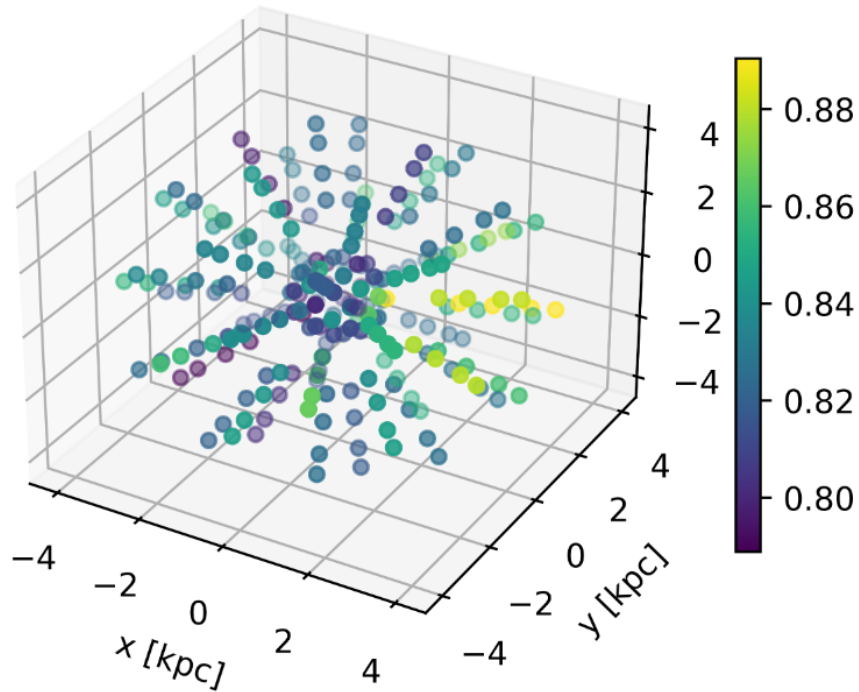
Figure 6.2: The 3D completeness model for B stars. This shows a sample of points at different distances from the Sun and using HEALPix with nside = 2 to query the 3D completeness model. The results are similar for O stars.

average completeness in a HEALPix bin from the Sun out to a certain distance. This provides the average total 3D completeness for OB stars, and ensures that at a distance of 4.2 kpc our 2D and 3D completeness models coincide.

Figure 6.1 shows the average 2D completeness of B stars (top) and O stars (bottom) along the line of sight out to 4.2 kpc. The color bar indicates the completeness, where a completeness of 0 indicates the sample is incomplete in that region and a completeness of 1 indicates that all stars were successfully detected in that region. In these 2D completeness models, we find that there are some structural components of the MW visible in the all-sky map of completeness for B stars. However, we can clearly see the structure of the dust component of the MW disk in the completeness map for O stars.

Figure 6.2 shows the average 3D completeness model for B stars. This depicts a sample of points at different distances from the Sun at HEALPix centers of nside = 2 to query the 3D completeness model. Each point represents the total average completeness out to that distance. The color bar indicates the completeness. The x, y, and z axes are given in rectangular Galactic coordinates and show the distance from the Sun in kpc. This 3D completeness model extends to 4.2 kpc in all directions such that it contains the entire region of interest for our 3D ISRF model. The 3D completeness model matches figure 6.1 at a distance of 4.2 kpc from the Sun.

6.5 Discussion and Conclusions

We are working to create an optimized 3D ISRF model with self-consistently determined structural parameters for the major stellar and dust components. Our work will provide the best model of the full 3D spectral intensity spatial distribution from UV-to-FIR for the MW, which is necessary for accurate calculation of CR electron/positron energy losses and the IC γ-ray production from the interstellar emissions. Our new model will also provide the most detailed description for the IR photon density and dust temperature distribution across the Galaxy over different spatial scales.

My contribution to this project is the creation of the 3D completeness model of OB stars in *Gaia* DR3. We have obtained OB stars from the *Gaia* DR3 catalogue which satisfy our quality cuts. Utilizing the Gaiaverse selection function, we calculate the completeness of our sample of O and B stars separately. This 3D completeness model can then be used to estimate the density profile and luminosity profile of OB stars in our 3D ISRF model.

The work in this chapter is still currently in progress by Louis Strigari and Troy Porter.

7. CONCLUSIONS

During the course of my dissertation work, I have published three papers, as discussed in chapters 2–4, and have contributed to two additional ongoing projects, as discussed in chapters 5 and 6. In this chapter I will summarize the conclusions from this dissertation.

In chapter 2 we have performed the first study of the DM relative velocity distribution of Milky Way-like halos, using the Auriga and APOSTLE cosmological simulations. We find that the DM pair-wise relative velocity distribution at nearly all radii in the halos is consistent with the Maxwell-Boltzmann distribution. This agreement is particularly good for the simulations that include baryons. For the corresponding DMO-simulations, the agreement with the Maxwell-Boltzmann distribution is good, though there are some notable deviations, particularly at small radii as the center of the halo is approached.

We have explored the implications for velocity-dependent DM annihilation, focusing on the Sommerfeld ($1/v$), s-wave (v^0), p-wave (v^2), and d-wave (v^4) models. We generally show that the $\mathcal{J}$-factors scale as the moments of the relative velocity distribution, and that the halo-to-halo scatter is largest for d-wave, and smallest for Sommerfeld models.

Our results indicate that in velocity-dependent models, the $\mathcal{J}$-factor is strongly correlated with the DM density in the halo, and is very weakly correlated with the velocity dispersion. This implies that if the DM density in the Milky Way can be robustly determined, one can accurately predict the DM annihilation signal, without the need to identify the DM velocity distribution in the Galaxy.

In chapter 3 we have used the high-resolution Auriga simulations of Milky Way-like galaxies to determine the contribution of halo substructure to the signal from DM annihilation. We consider the general case of velocity-dependent DM annihilation, examining Sommerfeld, s-wave, p-wave, and d-wave models. We find that substructure is the most significant in Sommerfeld models, while it is the least significant in d-wave models. In the Sommerfeld models, the total substructure contribution to the DM annihilation signal dominates that of the smooth component beyond $\sim 0.74 r_{200}$, while for all other models the substructure contribution is sub-dominant at all radii as

77

compared to the smooth halo.

Examining the luminosity functions of substructure, we find that in Sommerfeld models, the luminosity function is dominated by the least massive subhalos that are resolved. On the other hand, for d-wave models, the luminosity function is dominated by the most massive subhalos that are resolved. So extrapolating to lower subhalo mass scales may still increase the luminosity contribution from subhalos in Sommerfeld models, though it will not affect the luminosity contribution from subhalos in the case of d-wave models.

In chapter 4 we have presented a systematic study of the velocity-dependent DM annihilation signals from dwarf spheroidal galaxy analogues in the high-resolution APOSTLE cosmological simulations. We extract the DM density and pair-wise relative velocity distributions of the simulated dwarf spheroidal analogues to compute the $\mathcal{J}$-factors in the s-wave, p-wave, d-wave, and Sommerfeld annihilation models. We also quantify the error introduced in the $\mathcal{J}$-factors if we model the DM relative velocity distribution as a Maxwell-Boltzmann distribution.

We find a good agreement between the DM relative velocity distributions of the dwarf spheroidal analogues extracted from the simulations and their best fit Maxwellian distribution at all radii. As a result, the error introduced in the $\mathcal{J}$-factors from using the best fit Maxwellian distributions in different radial shells within a dwarf spheroidal analogue is on average 2.7% for the three velocity-dependent models.

Additionally, we compare our results to those found in the literature for specific dwarf spheroidal galaxies. We find that our effective $\mathcal{J}$-factors are generally in good agreement with those presented in previous work, which uses simplified models for the DM velocity distributions of the dwarf spheroidals [6]. The simulations we use in this dissertation do not force strict model assumptions on the velocity distribution.

In chapter 5 we have presented a systematic study of the velocity-dependent DM annihilation signals from M31 analogues in the high-resolution APOSTLE cosmological simulations. We extract the local DM density and the pair-wise relative velocity distributions of M31, the MW foreground, and external sources to compute the $\mathcal{J}$-factors in the s-wave, p-wave, d-wave, and

Sommerfeld annihilation models. We find that the extended emission from the smooth DM halo dominates over the emission from the MW foreground and external sources in all annihilation models. As in section 3.4, we find that substructure is the most significant in Sommerfeld and s-wave models, while it is the least significant in p-wave and d-wave models. Additionally, we find that the s-wave $\mathcal{J}$-factors for M31 and the MW foreground generally agree with the results of ref. [7].

In chapter 6 we are working to create an optimized 3D ISRF model with self-consistently determined structural parameters for the major stellar and dust components. Our work will provide the best model of the full 3D spectral intensity spatial distribution from UV-to-FIR for the MW, which is necessary for accurate calculation of CR electron/positron energy losses and the IC γ-ray production from the interstellar emissions. Our new model will also provide the most detailed description for the IR photon density and dust temperature distribution across the Galaxy over different spatial scales.

My contribution to this project is the creation of the 3D completeness model of OB stars in *Gaia* DR3. We have obtained OB stars from the *Gaia* DR3 catalogue which satisfy our quality cuts. Utilizing the Gaiaverse selection function, we calculate the completeness of our sample of O and B stars separately. This 3D completeness model can then be used to estimate the density profile and luminosity profile of OB stars in our 3D ISRF model.

REFERENCES

[1] D. Boubert and A. Everall, "Completeness of the gaia verse II: what are the odds that a star is missing from gaia DR2?," *Monthly Notices of the Royal Astronomical Society*, vol. 497, pp. 4246–4261, aug 2020.

[2] E. Board, N. Bozorgnia, L. E. Strigari, R. J. J. Grand, A. Fattahi, C. S. Frenk, F. Marinacci, J. F. Navarro, and K. A. Oman, "Velocity-dependent J-factors for annihilation radiation from cosmological simulations," *JCAP*, vol. 04, p. 070, 2021.

[3] E. Piccirillo, K. Blanchette, N. Bozorgnia, L. E. Strigari, C. S. Frenk, R. J. J. Grand, and F. Marinacci, "Velocity-dependent annihilation radiation from dark matter subhalos in cosmological simulations," *JCAP*, vol. 05, p. 058, 2022.

[4] K. Blanchette, E. Piccirillo, N. Bozorgnia, L. E. Strigari, A. Fattahi, C. S. Frenk, J. F. Navarro, and T. Sawala, "Velocity-dependent j-factors for milky way dwarf spheroidal analogues in cosmological simulations," *JCAP*, vol. 03, p. 021, 2023.

[5] R. Grand and S. White, "Baryonic effects on the detectability of annihilation radiation from dark matter subhaloes around the milky way," *Monthly Notices of the Royal Astronomical Society*, vol. 501, 2020.

[6] Boddy, Kimberly K. and Kumar, Jason and Pace, Andrew B. and Runburg, Jack and Strigari, Louis E., "Effective J-factors for Milky Way dwarf spheroidal galaxies with velocity-dependent annihilation," *Phys. Rev. D*, vol. 102, no. 2, p. 023029, 2020.

[7] C. M. Karwin, S. Murgia, I. V. Moskalenko, S. P. Fillingham, A.-K. Burns, and M. Fieg, "Dark matter interpretation of the fermi-lat observations toward the outer halo of m31," *Physical Review D*, vol. 103, jan 2021.

[8] R. J. J. Grand, A. J. Deason, S. D. M. White, C. M. Simpson, F. A. Gó mez, F. Marinacci, and R. Pakmor, "The effects of dynamical substructure on milky way mass estimates from

the high-velocity tail of the local stellar halo," *Monthly Notices of the Royal Astronomical Society: Letters*, vol. 487, pp. L72–L76, jun 2019.

[9] P. R. Kafle, S. Sharma, G. F. Lewis, and J. Bland-Hawthorn, "On the shoulders of giants: properties of the stellar halo and the milky way mass distribution," vol. 794, p. 59, sep 2014.

[10] J. F. Navarro, C. S. Frenk, and S. D. M. White, "The structure of cold dark matter halos," *The Astrophysical Journal*, vol. 462, p. 563, may 1996.

[11] T. Sawala *et al.*, "The APOSTLE simulations: solutions to the Local Group's cosmic puzzles," *Mon. Not. Roy. Astron. Soc.*, vol. 457, no. 2, pp. 1931–1943, 2016.

[12] H. W. Babcock, "The rotation of the Andromeda Nebula," *Lick Observatory Bulletin*, vol. 498, pp. 41–51, Jan. 1939.

[13] M. S. Roberts and R. N. Whitehurst, "The rotation curve and geometry of M31 at large galactocentric distances.," *apj*, vol. 201, pp. 327–346, Oct. 1975.

[14] M. Lisanti, S. Mishra-Sharma, N. L. Rodd, and B. R. Safdi, "Search for dark matter annihilation in galaxy groups," *Physical Review Letters*, vol. 120, mar 2018.

[15] M. Lisanti, S. Mishra-Sharma, N. L. Rodd, B. R. Safdi, and R. H. Wechsler, "Mapping extragalactic dark matter annihilation with galaxy surveys: A systematic study of stacked group searches," *Physical Review D*, vol. 97, mar 2018.

[16] M. Ahnen *et al.*, "Limits to Dark Matter Annihilation Cross-Section from a Combined Analysis of MAGIC and Fermi-LAT Observations of Dwarf Satellite Galaxies," *JCAP*, vol. 02, p. 039, 2016.

[17] M. Ackermann *et al.*, "Searching for Dark Matter Annihilation from Milky Way Dwarf Spheroidal Galaxies with Six Years of Fermi Large Area Telescope Data," *Phys. Rev. Lett.*, vol. 115, no. 23, p. 231301, 2015.

[18] A. Albert *et al.*, "Searching for Dark Matter Annihilation in Recently Discovered Milky Way Satellites with Fermi-LAT," *Astrophys. J.*, vol. 834, no. 2, p. 110, 2017.

[19] H. Abdallah *et al.*, "Search for dark matter signals towards a selection of recently detected DES dwarf galaxy satellites of the Milky Way with H.E.S.S.," *Phys. Rev. D*, vol. 102, no. 6, p. 062001, 2020.

[20] A. Albert *et al.*, "Dark Matter Limits From Dwarf Spheroidal Galaxies with The HAWC Gamma-Ray Observatory," *Astrophys. J.*, vol. 853, no. 2, p. 154, 2018.

[21] R. K. Leane, "Indirect Detection of Dark Matter in the Galaxy," in *3rd World Summit on Exploring the Dark Side of the Universe*, 5 2020.

[22] J. D. March-Russell and S. M. West, "WIMPonium and Boost Factors for Indirect Dark Matter Detection," *Phys. Lett. B*, vol. 676, pp. 133–139, 2009.

[23] J. March-Russell, S. M. West, D. Cumberbatch, and D. Hooper, "Heavy Dark Matter Through the Higgs Portal," *JHEP*, vol. 07, p. 058, 2008.

[24] B. Robertson and A. Zentner, "Dark Matter Annihilation Rates with Velocity-Dependent Annihilation Cross Sections," *Phys. Rev. D*, vol. 79, p. 083525, 2009.

[25] F. Ferrer and D. R. Hunter, "The impact of the phase-space density on the indirect detection of dark matter," *JCAP*, vol. 09, p. 005, 2013.

[26] K. K. Boddy, J. Kumar, L. E. Strigari, and M.-Y. Wang, "Sommerfeld-Enhanced J-Factors For Dwarf Spheroidal Galaxies," *Phys. Rev.*, vol. D95, no. 12, p. 123008, 2017.

[27] Y. Zhao, X.-J. Bi, P.-F. Yin, and X. Zhang, "Constraint on the velocity dependent dark matter annihilation cross section from gamma-ray and kinematic observations of ultrafaint dwarf galaxies," *Phys. Rev. D*, vol. 97, no. 6, p. 063013, 2018.

[28] M. Petac, P. Ullio, and M. Valli, "On velocity-dependent dark matter annihilations in dwarf satellites," *JCAP*, vol. 12, p. 039, 2018.

[29] K. K. Boddy, J. Kumar, and L. E. Strigari, "Effective J -factor of the Galactic Center for velocity-dependent dark matter annihilation," *Phys. Rev.*, vol. D98, no. 6, p. 063012, 2018.

[30] T. Lacroix, M. Stref, and J. Lavalle, "Anatomy of Eddington-like inversion methods in the context of dark matter searches," *JCAP*, vol. 09, p. 040, 2018.

[31] K. K. Boddy, J. Kumar, J. Runburg, and L. E. Strigari, "Angular distribution of gamma-ray emission from velocity-dependent dark matter annihilation in subhalos," *Phys. Rev.*, vol. D100, no. 6, p. 063019, 2019.

[32] D. McKeown, J. S. Bullock, F. J. Mercado, Z. Hafen, M. Boylan-Kolchin, A. Wetzel, L. Necib, P. F. Hopkins, and S. Yu, "Amplified j-factors in the galactic centre for velocity-dependent dark matter annihilation in FIRE simulations," *Monthly Notices of the Royal Astronomical Society*, vol. 513, pp. 55–70, apr 2022.

[33] J. Hisano, M. Kawasaki, K. Kohri, T. Moroi, K. Nakayama, and T. Sekiguchi, "Cosmological constraints on dark matter models with velocity-dependent annihilation cross section," *Phys. Rev. D*, vol. 83, p. 123511, 2011.

[34] C. Johnson, R. Caputo, C. Karwin, S. Murgia, S. Ritz, and J. Shelton, "Search for gamma-ray emission from p-wave dark matter annihilation in the Galactic Center," *Phys. Rev. D*, vol. 99, no. 10, p. 103007, 2019.

[35] R. J. J. Grand, F. A. Gómez, F. Marinacci, R. Pakmor, V. Springel, D. J. R. Campbell, C. S. Frenk, A. Jenkins, and S. D. M. White, "The Auriga Project: the properties and formation mechanisms of disc galaxies across cosmic time," *Mon. Not. Roy. Astron. Soc.*, vol. 467, no. 1, pp. 179–207, 2017.

[36] T. Sawala, C. S. Frenk, A. Fattahi, J. F. Navarro, R. G. Bower, R. A. Crain, C. Dalla Vecchia, M. Furlong, A. Jenkins, I. G. McCarthy, Y. Qu, M. Schaller, J. Schaye, and T. Theuns, "Bent by baryons: the low-mass galaxy-halo relation," *MNRAS*, vol. 448, pp. 2941–2947, Apr. 2015.

[37] A. Fattahi, J. Navarro, T. Sawala, C. Frenk, K. Oman, R. Crain, M. Furlong, M. Schaller, J. Schaye, T. Theuns, and A. Jenkins, "The apostle project: Local group kinematic mass

constraints and simulation candidate selection," *Monthly Notices of the Royal Astronomical Society*, vol. 457, 07 2015.

[38] T. Sawala, C. S. Frenk, A. Fattahi, J. F. Navarro, R. G. Bower, R. A. Crain, C. D. Vecchia, M. Furlong, J. C. Helly, A. Jenkins, K. A. Oman, M. Schaller, J. Schaye, T. Theuns, J. Trayford, and S. D. M. White, "Local group galaxies emerge from the dark," 2014.

[39] J. Schaye, R. A. Crain, R. G. Bower, M. Furlong, M. Schaller, T. Theuns, C. Dalla Vecchia, C. S. Frenk, I. G. McCarthy, J. C. Helly, A. Jenkins, Y. M. Rosas-Guevara, S. D. M. White, M. Baes, , and . more authors, "The EAGLE project: simulating the evolution and assembly of galaxies and their environments," *MNRAS*, vol. 446, pp. 521–554, 2015.

[40] R. A. Crain, J. Schaye, R. G. Bower, M. Furlong, M. Schaller, T. Theuns, C. Dalla Vecchia, C. S. Frenk, I. G. McCarthy, J. C. Helly, A. Jenkins, Y. M. Rosas-Guevara, S. D. M. White, and J. W. Trayford, "The EAGLE simulations of galaxy formation: calibration of subgrid physics and model variations," *MNRAS*, vol. 450, pp. 1937–1961, June 2015.

[41] V. Springel, "E pur si muove: Galilean-invariant cosmological hydrodynamical simulations on a moving mesh," *MNRAS*, vol. 401, pp. 791–851, Jan. 2010.

[42] Planck Collaboration, P. A. R. Ade, N. Aghanim, M. Arnaud, M. Ashdown, J. Aumont, C. Baccigalupi, A. J. Banday, R. B. Barreiro, J. G. Bartlett, and et al., "Planck 2015 results - xiii. cosmological parameters," *A&A*, vol. 594, p. A13, 2016.

[43] C. Power, J. F. Navarro, A. Jenkins, C. S. Frenk, S. D. M. White, V. Springel, J. Stadel, and T. R. Quinn, "The Inner structure of Lambda CDM halos. 1. A Numerical convergence study," *Mon. Not. Roy. Astron. Soc.*, vol. 338, pp. 14–34, 2003.

[44] A. Jenkins, "A new way of setting the phases for cosmological multiscale Gaussian initial conditions," *MNRAS*, vol. 434, pp. 2094–2120, Sept. 2013.

[45] V. Springel, J. Wang, M. Vogelsberger, A. Ludlow, A. Jenkins, A. Helmi, J. F. Navarro, C. S. Frenk, and S. D. M. White, "The Aquarius Project: the subhaloes of galactic haloes," *MNRAS*, vol. 391, pp. 1685–1711, 2008.

[46] M. Schaller, C. Dalla Vecchia, J. Schaye, R. G. Bower, T. Theuns, R. A. Crain, M. Furlong, and I. G. McCarthy, "The EAGLE simulations of galaxy formation: the importance of the hydrodynamics scheme," *MNRAS*, vol. 454, pp. 2277–2291, Dec. 2015.

[47] T. Buck, C. Pfrommer, R. Pakmor, R. J. J. Grand, and V. Springel, "The effects of cosmic rays on the formation of milky way-mass galaxies in a cosmological context," *Monthly Notices of the Royal Astronomical Society*, vol. 497, pp. 1712–1737, jul 2020.

[48] I. S. Butsky and T. R. Quinn, "The role of cosmic-ray transport in shaping the simulated circumgalactic medium," *The Astrophysical Journal*, vol. 868, p. 108, nov 2018.

[49] T. K. Chan, D. Kereš , P. F. Hopkins, E. Quataert, K.-Y. Su, C. C. Hayward, and C.-A. Faucher-Giguère, "Cosmic ray feedback in the fire simulations: constraining cosmic ray propagation with GeV gamma-ray emission," *Monthly Notices of the Royal Astronomical Society*, vol. 488, pp. 3716–3744, jul 2019.

[50] Y. Dubois, B. Commerçon, A. Marcowith, and L. Brahimi, "Shock-accelerated cosmic rays and streaming instability in the adaptive mesh refinement code ramses," *Astronomy & Astrophysics*, vol. 631, p. A121, nov 2019.

[51] P. Girichidis, T. Naab, M. Hanasz, and S. Walch, "Cooler and smoother – the impact of cosmic rays on the phase structure of galactic outflows," *Monthly Notices of the Royal Astronomical Society*, vol. 479, pp. 3042–3067, jun 2018.

[52] P. Girichidis, C. Pfrommer, M. Hanasz, and T. Naab, "Spectrally resolved cosmic ray hydrodynamics – i. spectral scheme," *Monthly Notices of the Royal Astronomical Society*, nov 2019.

[53] P. Girichidis, T. Naab, S. Walch, M. Hanasz, M.-M. M. Low, J. P. Ostriker, A. Gatto, T. Peters, R. Wünsch, S. C. O. Glover, R. S. Klessen, P. C. Clark, and C. Baczynski, "Launching cosmic-ray-driven outflows from the magnetized interstellar medium," vol. 816, p. L19, jan 2016.

[54] P. F. Hopkins, T. K. Chan, S. Garrison-Kimmel, S. Ji, K.-Y. Su, C. B. Hummels, D. Kereš, E. Quataert, and C.-A. Faucher-Giguère, "But what about...: cosmic rays, magnetic fields, conduction, and viscosity in galaxy formation," *Monthly Notices of the Royal Astronomical Society*, vol. 492, pp. 3465–3498, dec 2019.

[55] Fermi-LAT, "Gev observations of star-forming galaxies with fermi lat," *The Astrophysical Journal*, vol. 755, p. 164, aug 2012.

[56] N. Bozorgnia, F. Calore, M. Schaller, M. Lovell, G. Bertone, C. S. Frenk, R. A. Crain, J. F. Navarro, J. Schaye, and T. Theuns, "Simulated Milky Way analogues: implications for dark matter direct searches," *JCAP*, vol. 1605, no. 05, p. 024, 2016.

[57] N. Bozorgnia, A. Fattahi, C. S. Frenk, A. Cheek, D. G. Cerdeno, F. A. Gómez, R. J. Grand, and F. Marinacci, "The dark matter component of the Gaia radially anisotropic substructure," *JCAP*, vol. 07, p. 036, 2020.

[58] T. M. Callingham, M. Cautun, A. J. Deason, C. S. Frenk, W. Wang, F. A. Gómez, R. J. J. Grand, F. Marinacci, and R. Pakmor, "The mass of the Milky Way from satellite dynamics," *MNRAS*, vol. 484, pp. 5453–5467, Apr 2019.

[59] P. J. McMillan, "Mass models of the Milky Way," *Mon. Not. Roy. Astron. Soc.*, vol. 414, pp. 2446–2457, 2011.

[60] F. Iocco, M. Pato, and G. Bertone, "Evidence for dark matter in the inner Milky Way," *Nature Phys.*, vol. 11, pp. 245–248, 2015.

[61] J. Schaye, R. A. Crain, R. G. Bower, M. Furlong, M. Schaller, T. Theuns, C. Dalla Vecchia, C. S. Frenk, I. G. McCarthy, J. C. Helly, A. Jenkins, Y. M. Rosas-Guevara, S. D. M. White, M. Baes, C. M. Booth, P. Camps, J. F. Navarro, Y. Qu, A. Rahmati, T. Sawala, P. A. Thomas, and J. Trayford, "The EAGLE project: simulating the evolution and assembly of galaxies and their environments," *MNRAS*, vol. 446, pp. 521–554, Jan. 2015.

[62] N. Bozorgnia and G. Bertone, "Implications of hydrodynamical simulations for the interpretation of direct dark matter searches," *Int. J. Mod. Phys.*, vol. A32, no. 21, p. 1730016, 2017.

[63] C. Kelso, C. Savage, M. Valluri, K. Freese, G. S. Stinson, and J. Bailin, "The impact of baryons on the direct detection of dark matter," *JCAP*, vol. 1608, p. 071, 2016.

[64] J. D. Sloane, M. R. Buckley, A. M. Brooks, and F. Governato, "Assessing Astrophysical Uncertainties in Direct Detection with Galaxy Simulations," *Astrophys. J.*, vol. 831, p. 93, 2016.

[65] M. Schaller *et al.*, "Dark matter annihilation radiation in hydrodynamic simulations of Milky Way haloes," *Mon. Not. Roy. Astron. Soc.*, vol. 455, no. 4, pp. 4442–4451, 2016.

[66] J. Dubinski, "The Effect of dissipation on the shapes of dark halos," *Astrophys. J.*, vol. 431, pp. 617–624, 1994.

[67] M. G. Abadi, J. F. Navarro, M. Fardal, A. Babul, and M. Steinmetz, "Galaxy-Induced Transformation of Dark Matter Halos," *Mon. Not. Roy. Astron. Soc.*, vol. 407, pp. 435–446, 2010.

[68] S. Bryan, S. Kay, A. Duffy, J. Schaye, C. Vecchia, and C. Booth, "The impact of baryons on the spins and shapes of dark matter haloes," *Mon. Not. Roy. Astron. Soc.*, vol. 429, p. 3316, 2013.

[69] Q. Zhu, F. Marinacci, M. Maji, Y. Li, V. Springel, and L. Hernquist, "Baryonic impact on the dark matter distribution in Milky Way-sized galaxies and their satellites," *Mon. Not. Roy. Astron. Soc.*, vol. 458, no. 2, pp. 1559–1580, 2016.

[70] J. Prada, J. E. Forero-Romero, R. J. Grand, R. Pakmor, and V. Springel, "Dark matter halo shapes in the Auriga simulations," *Mon. Not. Roy. Astron. Soc.*, vol. 490, no. 4, pp. 4877–4888, 2019.

[71] M. Schaller, C. S. Frenk, R. G. Bower, T. Theuns, A. Jenkins, J. Schaye, R. A. Crain, M. Furlong, C. D. Vecchia, and I. McCarthy, "Baryon effects on the internal structure of

ΛCDM haloes in the EAGLE simulations," *Mon. Not. Roy. Astron. Soc.*, vol. 451, no. 2, pp. 1247–1267, 2015.

[72] M. Cautun, A. Benitez-Llambay, A. J. Deason, C. S. Frenk, A. Fattahi, F. A. Gómez, R. J. Grand, K. A. Oman, J. F. Navarro, and C. M. Simpson, "The Milky Way total mass profile as inferred from Gaia DR2," *Mon. Not. Roy. Astron. Soc.*, vol. 494, no. 3, pp. 4291–4313, 2020.

[73] T. M. Callingham, M. Cautun, A. J. Deason, C. S. Frenk, R. J. Grand, F. Marinacci, and R. Pakmor, "The orbital phase space of contracted dark matter haloes," *Mon. Not. Roy. Astron. Soc.*, vol. 495, no. 1, pp. 12–28, 2020.

[74] A. K. Drukier, K. Freese, and D. N. Spergel, "Detecting Cold Dark Matter Candidates," *Phys. Rev.*, vol. D33, pp. 3495–3508, 1986.

[75] S. Kazantzidis, J. Magorrian, and B. Moore, "Generating equilibrium dark matter halos: Inadequacies of the local Maxwellian approximation," *Astrophys. J.*, vol. 601, pp. 37–46, 2004.

[76] R. J. Grand and S. D. White, "Baryonic effects on the detectability of annihilation radiation from dark matter subhaloes around the Milky Way," 12 2020.

[77] M. Davis, G. Efstathiou, C. S. Frenk, and S. D. M. White, "The Evolution of Large Scale Structure in a Universe Dominated by Cold Dark Matter," *Astrophys. J.*, vol. 292, pp. 371–394, 1985.

[78] V. Springel, S. White, C. Frenk, J. Navarro, A. Jenkins, M. Vogelsberger, J. Wang, A. Ludlow, and A. Helmi, "Prospects for detecting supersymmetric dark matter in the Galactic halo," *Nature*, vol. 456N7218, pp. 73–80, 2008.

[79] J. Wang, S. Bose, C. S. Frenk, L. Gao, A. Jenkins, V. Springel, and S. D. M. White, "Universal structure of dark matter haloes over a mass range of 20 orders of magnitude," *Nature*, vol. 585, no. 7823, pp. 39–42, 2020.

[80] J. Kumar and D. Marfatia, "Matrix element analyses of dark matter scattering and annihilation," *Phys. Rev. D*, vol. 88, no. 1, p. 014035, 2013.

[81] F. Giacchino, L. Lopez-Honorez, and M. H. Tytgat, "Scalar Dark Matter Models with Significant Internal Bremsstrahlung," *JCAP*, vol. 10, p. 025, 2013.

[82] C. Han, H. M. Lee, M. Park, and V. Sanz, "The diphoton resonance as a gravity mediator of dark matter," *Phys. Lett. B*, vol. 755, pp. 371–379, 2016.

[83] R. Diamanti, L. Lopez-Honorez, O. Mena, S. Palomares-Ruiz, and A. C. Vincent, "Constraining Dark Matter Late-Time Energy Injection: Decays and P-Wave Annihilations," *JCAP*, vol. 02, p. 017, 2014.

[84] A. Das and B. Dasgupta, "Selection Rule for Enhanced Dark Matter Annihilation," *Phys. Rev. Lett.*, vol. 118, no. 25, p. 251101, 2017.

[85] V. Springel, S. D. M. White, G. Tormen, and G. Kauffmann, "Populating a cluster of galaxies. 1. Results at z = 0," *Mon. Not. Roy. Astron. Soc.*, vol. 328, p. 726, 2001.

[86] L. Gao, J. F. Navarro, S. Cole, C. Frenk, S. D. M. White, V. Springel, A. Jenkins, and A. F. Neto, "The redshift dependence of the structure of massive LCDM halos," *Mon. Not. Roy. Astron. Soc.*, vol. 387, p. 536, 2008.

[87] R. J. J. Grand and S. D. M. White, "Dark matter annihilation and the galactic centre excess," *Monthly Notices of the Royal Astronomical Society: Letters*, vol. 511, pp. L55–L59, feb 2022.

[88] C. Frenk and S. White, "Dark matter and cosmic structure," *Annalen der Physik*, vol. 524, p. 507–534, Sep 2012.

[89] J. Wang, S. Bose, C. S. Frenk, L. Gao, A. Jenkins, V. Springel, and S. D. M. White, "Universal structure of dark matter haloes over a mass range of 20 orders of magnitude," *Nature*, vol. 585, p. 39–42, Sep 2020.

[90] D. Hooper and L. Goodenough, "Dark Matter Annihilation in The Galactic Center As Seen by the Fermi Gamma Ray Space Telescope," *Phys. Lett. B*, vol. 697, pp. 412–428, 2011.

[91] S. Murgia, "The Fermi–LAT Galactic Center Excess: Evidence of Annihilating Dark Matter?," *Ann. Rev. Nucl. Part. Sci.*, vol. 70, pp. 455–483, 2020.

[92] M. Di Mauro, "Characteristics of the galactic center excess measured with 11 years of fermi -lat data," *Physical Review D*, vol. 103, Mar 2021.

[93] A. A. Abdo *et al.*, "Fermi Large Area Telescope observations of Local Group galaxies: Detection of M31 and search for M33," *Astron. Astrophys.*, vol. 523, p. L2, 2010.

[94] C. M. Karwin, S. Murgia, I. Moskalenko, S. Fillingham, A.-K. Burns, and M. Fieg, "Dark matter interpretation of the $Fermi$-LAT observations toward the outer halo of M31," *Phys. Rev. D*, vol. 103, no. 2, p. 023027, 2021.

[95] J. Wolf, G. D. Martinez, J. S. Bullock, M. Kaplinghat, M. Geha, R. R. Muñ oz, J. D. Simon, and F. F. Avedo, "Accurate masses for dispersion-supported galaxies," *Monthly Notices of the Royal Astronomical Society*, may 2010.

[96] A. W. McConnachie, "The observed properties of dwarf galaxies in and around the local group," *The Astronomical Journal*, vol. 144, p. 4, Jun 2012.

[97] A. Genina, J. I. Read, C. S. Frenk, S. Cole, A. Benitez-Llambay, A. D. Ludlow, J. F. Navarro, K. A. Oman, and A. Robertson, "To β or not to β: can higher order Jeans analysis break the mass–anisotropy degeneracy in simulated dwarfs?," *Mon. Not. Roy. Astron. Soc.*, vol. 498, no. 1, pp. 144–163, 2020.

[98] S. Bose *et al.*, "No cores in dark matter-dominated dwarf galaxies with bursty star formation histories," *Mon. Not. Roy. Astron. Soc.*, vol. 486, no. 4, pp. 4790–4804, 2019.

[99] A. Benítez-Llambay, C. S. Frenk, A. D. Ludlow, and J. F. Navarro, "Baryon-induced dark matter cores in the eagle simulations," *Mon. Not. Roy. Astron. Soc.*, vol. 488, no. 2, pp. 2387–2404, 2019.

[100] L. M. Widrow, "Distribution Functions for Cuspy Dark Matter Density Profiles," *apjs*, vol. 131, pp. 39–46, Nov. 2000.

[101] V. Springel, J. Wang, M. Vogelsberger, A. Ludlow, A. Jenkins, A. Helmi, J. F. Navarro, C. S. Frenk, and S. D. M. White, "The Aquarius Project: the subhalos of galactic halos," *Mon. Not. Roy. Astron. Soc.*, vol. 391, pp. 1685–1711, 2008.

[102] M. Wood, R. Caputo, E. Charles, M. Di Mauro, J. Magill, and J. S. Perkins, "Fermipy: An open-source Python package for analysis of Fermi-LAT Data," *PoS*, vol. ICRC2017, p. 824, 2017.

[103] A. J. Evans, L. E. Strigari, O. Svenborn, A. Albert, J. P. Harding, D. Hooper, T. Linden, and A. B. Pace, "On the gamma-ray emission from the core of the sagittarius dwarf galaxy," 2022.

[104] F. Aharonian, R.-Z. Yang, and E. Wilhelmi, "Massive stars as major factories of galactic cosmic rays," *Nature Astronomy*, vol. 3, 06 2019.

[105] R. zhi Yang, E. de Oñ a Wilhelmi, and F. Aharonian, "Diffuse γ-ray emission in the vicinity of young star cluster westerlund 2," *Astronomy & Astrophysics*, vol. 611, p. A77, mar 2018.

[106] J. N. Bahcall, "Star counts and galactic structure," *Annual Review of Astronomy and Astrophysics*, vol. 24, no. 1, pp. 577–611, 1986.

[107] M. Jurić , Ž. Ivezić, A. Brooks, R. H. Lupton, D. Schlegel, D. Finkbeiner, N. Padmanabhan, N. Bond, B. Sesar, C. M. Rockosi, G. R. Knapp, J. E. Gunn, T. Sumi, D. P. Schneider, J. C. Barentine, H. J. Brewington, J. Brinkmann, M. Fukugita, M. Harvanek, S. J. Kleinman, J. Krzesinski, D. Long, J. Eric H. Neilsen, A. Nitta, S. A. Snedden, and D. G. York, "The milky way tomography with SDSS. i. stellar number density distribution," *The Astrophysical Journal*, vol. 673, pp. 864–914, feb 2008.

[108] J. Bovy, "Stellar inventory of the solar neighbourhood using Gaia DR1," *Monthly Notices of the Royal Astronomical Society*, vol. 470, pp. 1360–1387, 05 2017.

[109] J. W. Bergstrom, R. D. Gehrz, and T. J. Jones, "Observations of the 2.2-μm emission from the halo of ngc 4244 at large galactocentric distances," *Publications of the Astronomical Society of the Pacific*, vol. 104, no. 678, pp. 695–699, 1992.

[110] A. J. Pickles, "A Stellar Spectral Flux Library: 1150-25000 Å," *pasp*, vol. 110, pp. 863–878, July 1998.

[111] R. J. Wainscoat, M. Cohen, K. Volk, H. J. Walker, and D. E. Schwartz, "A Model of the 8–25 Micron Point Source Infrared Sky," *apjs*, vol. 83, p. 111, Nov. 1992.

[112] P. T. de Zeeuw, R. Hoogerwerf, J. H. J. de Bruijne, A. G. A. Brown, and A. Blaauw, "A [ITAL]hipparcos[/ITAL] census of the nearby OB associations," *The Astronomical Journal*, vol. 117, pp. 354–399, jan 1999.

[113] F. van Leeuwen, "Validation of the new hipparcos reduction," *Astronomy & Astrophysics*, vol. 474, pp. 653–664, aug 2007.

[114] Y. Xu, S. B. Bian, M. J. Reid, J. J. Li, B. Zhang, Q. Z. Yan, T. M. Dame, K. M. Menten, Z. H. He, S. L. Liao, and Z. H. Tang, "A comparison of the local spiral structure from gaia DR2 and VLBI maser parallaxes," *Astronomy & Astrophysics*, vol. 616, p. L15, aug 2018.

[115] X. Luri, A. G. A. Brown, L. M. Sarro, F. Arenou, C. A. L. Bailer-Jones, A. Castro-Ginard, J. de Bruijne, T. Prusti, C. Babusiaux, and H. E. Delgado, "Gaia data release 2," *Astronomy & Astrophysics*, vol. 616, p. A9, aug 2018.

[116] J. Buch, S. C. J. Leung, and J. Fan, "Using gaia DR2 to constrain local dark matter density and thin dark disk," *Journal of Cosmology and Astroparticle Physics*, vol. 2019, pp. 026–026, apr 2019.

[117] J. Bovy *et al.*, "The apogee red-clump catalog: Precise distances, velocities, and high-resolution elemental abundances over a large area of the milky way's disk," *The Astrophysical Journal*, vol. 790, p. 127, jul 2014.

[118] T. Cantat-Gaudin, M. Fouesneau, H.-W. Rix, A. G. A. Brown, A. Castro-Ginard, Z. Kostrzewa-Rutkowska, R. Drimmel, D. W. Hogg, A. R. Casey, S. Khanna, S. Oh, A. M.

Price-Whelan, V. Belokurov, A. K. Saydjari, and G. Green, "An empirical model of the gaia dr3 selection function," *Astronomy & Astrophysics*, vol. 669, p. A55, jan 2023.

BEST FIT PARAMETERS FOR RELATIVE VELOCITY DISTRIBUTIONS[*]

In table A.1 we present the best fit peak speeds and reduced χ^2 values for the Maxwellian functional form to fit the DM relative velocity modulus distributions of the Auriga and APOSTLE MW-like halos. The best fit parameters are given for the DM particles in spherical shells at different radii from the center of the halo.

	$r = 2$ kpc		$r = 8$ kpc		$r = 20$ kpc		$r = 50$ kpc	
Halo Name	v_0 [km s^{-1}]	$\chi^2_{\rm red}$	v_0 [km s^{-1}]	$\chi^2_{\rm red}$	v_0 [km s^{-1}]	$\chi^2_{\rm red}$	v_0 [km s^{-1}]	$\chi^2_{\rm red}$
Au2	315.93	1.05	321.03	1.99	307.43	0.91	263.53	1.33
Au4	337.43	0.98	335.43	0.86	297.53	1.05	245.12	2.09
Au5	379.34	0.46	338.43	0.63	293.63	0.96	236.62	1.14
Au7	308.93	0.68	298.33	0.72	268.13	0.80	225.42	1.24
Au9	384.14	0.51	328.33	0.71	274.93	0.72	226.62	2.12
Au12	341.83	0.56	314.93	0.81	273.53	1.01	235.42	2.12
Au19	326.23	0.62	299.83	0.63	280.13	0.86	233.02	1.88
Au21	331.93	0.21	330.73	0.63	303.73	1.28	246.92	1.67
Au22	401.64	0.61	316.73	1.64	270.53	2.48	220.92	1.47
Au24	363.04	0.40	329.03	0.53	302.13	1.13	249.42	1.63
AP-V1-1-L2	309.58	0.89	312.75	0.49	299.72	0.73	267.15	1.55
AP-V6-1-L2	368.60	0.62	331.61	0.53	308.73	0.52	273.38	1.07
AP-S4-1-L2	297.77	0.62	295.07	0.42	271.10	0.64	243.93	0.92
AP-V4-1-L2	296.83	0.68	296.91	0.55	269.67	0.61	238.93	1.84
AP-V4-2-L2	298.68	0.92	244.91	0.90	229.59	0.66	198.06	1.17
AP-S6-1-L2	313.43	0.91	267.60	0.97	241.73	1.24	201.78	1.19

Table A.1: Best fit peak speed, v_0, and the reduced χ^2 values for the goodness of fit of the Maxwellian velocity distributions to the DM speed distributions of the Auriga and APOSTLE MW-like halos at different radii from the center of the halo. Reprinted with permission from ref. [2].

APPENDIX B

COMPONENTS OF THE RELATIVE VELOCITY DISTRIBUTIONS[*]

In figure B.1 we show the radial ($v_{\mathrm{rel},r}$), polar ($v_{\mathrm{rel},\theta}$), and azimuthal ($v_{\mathrm{rel},\phi}$) components of the DM relative velocity distributions for halos Au2 and Au22 at four different Galactocentric radii. The origin of our reference frame is at the Galactic center, and the z-axis is perpendicular to the stellar disk. The three components of the relative velocity distribution are individually normalized to unity, such that $\int dv_{\mathrm{rel},i} f(v_{\mathrm{rel},i}) = 1$ for $i = r, \theta, \phi$.

The three components of the relative velocity distribution are different at each radius, and there is a clear velocity anisotropy at all radii. The solid colored curves in each panel specify the best fit Gaussian distribution to each relative velocity component for the two halos.

To better understand the degree of anisotropy in the relative velocities, we compute the anisotropy parameter,

$$\beta = 1 - \frac{\sigma_\theta^2 + \sigma_\phi^2}{2\sigma_r^2}, \tag{B.1}$$

where σ_r, σ_θ, and σ_ϕ are the radial, polar, and azimuthal velocity dispersions, respectively. Notice that for an isotropic velocity distribution, $\beta = 0$. In figure B.2 we show the anisotropy parameter as a function of Galactocentric radius for the Auriga MW-like halos. We can see that at small radii, relative velocity distributions of all halos are close to isotropic, but become more anisotropic as we move further from the Galactic center.

To better compare halos Au2 and Au22, we can also study the shape of their halos. In section 2.2 we define the range of sphericities of all the Auriga MW-like halos at four different radii. For Au2 we have $s(2\ \mathrm{kpc}) = 0.66$, $s(8\ \mathrm{kpc}) = 0.72$, $s(20\ \mathrm{kpc}) = 0.71$, and $s(50\ \mathrm{kpc}) = 0.63$. For Au22 we have $s(2\ \mathrm{kpc}) = 0.82$, $s(8\ \mathrm{kpc}) = 0.86$, $s(20\ \mathrm{kpc}) = 0.88$, and $s(50\ \mathrm{kpc}) = 0.86$.

---

[*]Reprinted with permission from "Velocity-dependent J-factors for annihilation radiation from cosmological simulations" by Board et al., 2021. Journal of Cosmology and Astroparticle Physics, vol. 04, p. 070, Copyright [2021] by IOP Publishing Ltd and Sissa Medialab.

Deviations from sphericity can be described by the triaxiality parameter,

$$T = \frac{a^2 - b^2}{a^2 - c^2},$$
(B.2)

where $a \geq b \geq c$ are the three axes of the ellipsoid obtained from the inertia tensor. For very oblate systems, $T \approx 0$, whereas for very prolate systems, $T \approx 1$. For Au2 we have $T(2 \text{ kpc}) = 0.72$, $T(8 \text{ kpc}) = 0.46$, $T(20 \text{ kpc}) = 0.17$, and $T(50 \text{ kpc}) = 0.12$. For Au22 we have $T(2 \text{ kpc}) = 0.56$, $T(8 \text{ kpc}) = 0.30$, $T(20 \text{ kpc}) = 0.31$, and $T(50 \text{ kpc}) = 0.44$. Hence, Au2 has a larger deviation from sphericity and is more triaxial compared to Au22.
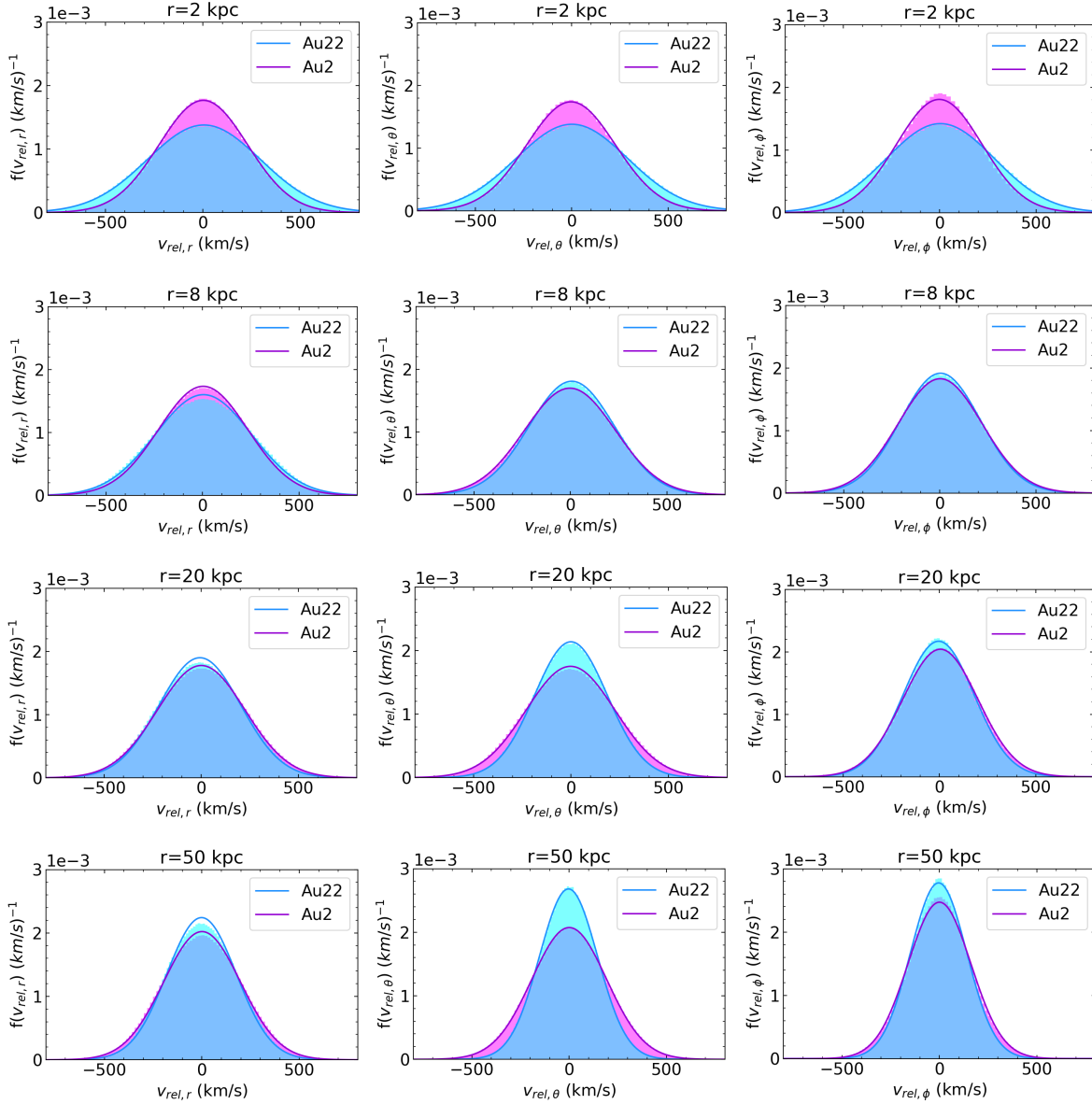
Figure B.1: The histograms show the radial (left panels), polar (middle panels) and azimuthal (right panels) components of the DM relative velocity distributions for halos Au2 (magenta) and Au22 (blue). From top to bottom the rows show the distributions in radial shells at 2 kpc, 8 kpc, 20 kpc, and 50 kpc from the Galactic center. The solid lines specify the best fit Gaussian distribution for each velocity component and each halo. Reprinted with permission from ref. [2].
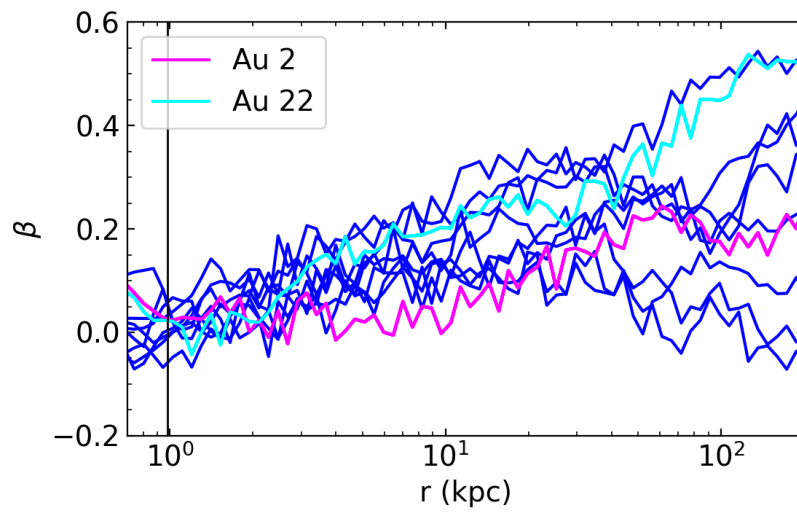
Figure B.2: Anisotropy parameter, β, as a function of Galactocentric radius for the 10 Auriga MW-like halos. The cyan and magenta curves specify the anisotropy parameter for halos Au2 and Au22, respectively. Reprinted with permission from ref. [2].

APPENDIX C

$\mathcal{J}$-FACTORS USING AN NFW PROFILE[*]

In this appendix, we present the $\widetilde{\mathcal{J}}_s$-factors for nine dSph analogues, using their best fit NFW density profiles. Figure C.1 shows a comparison of the results for the cases where the DM relative velocity distributions are obtained directly from the simulation data, when using a MB velocity distribution with a peak speed obtained from the power law fit, and the results presented in figure 1 of ref. [6]. Comparing figures C.1 and 4.7, we can see that the scatter in the $\widetilde{\mathcal{J}}_s$-factors is slightly larger when the best fit NFW density profiles are used, but there are no major systematic differences relative to the results using the Einasto model.
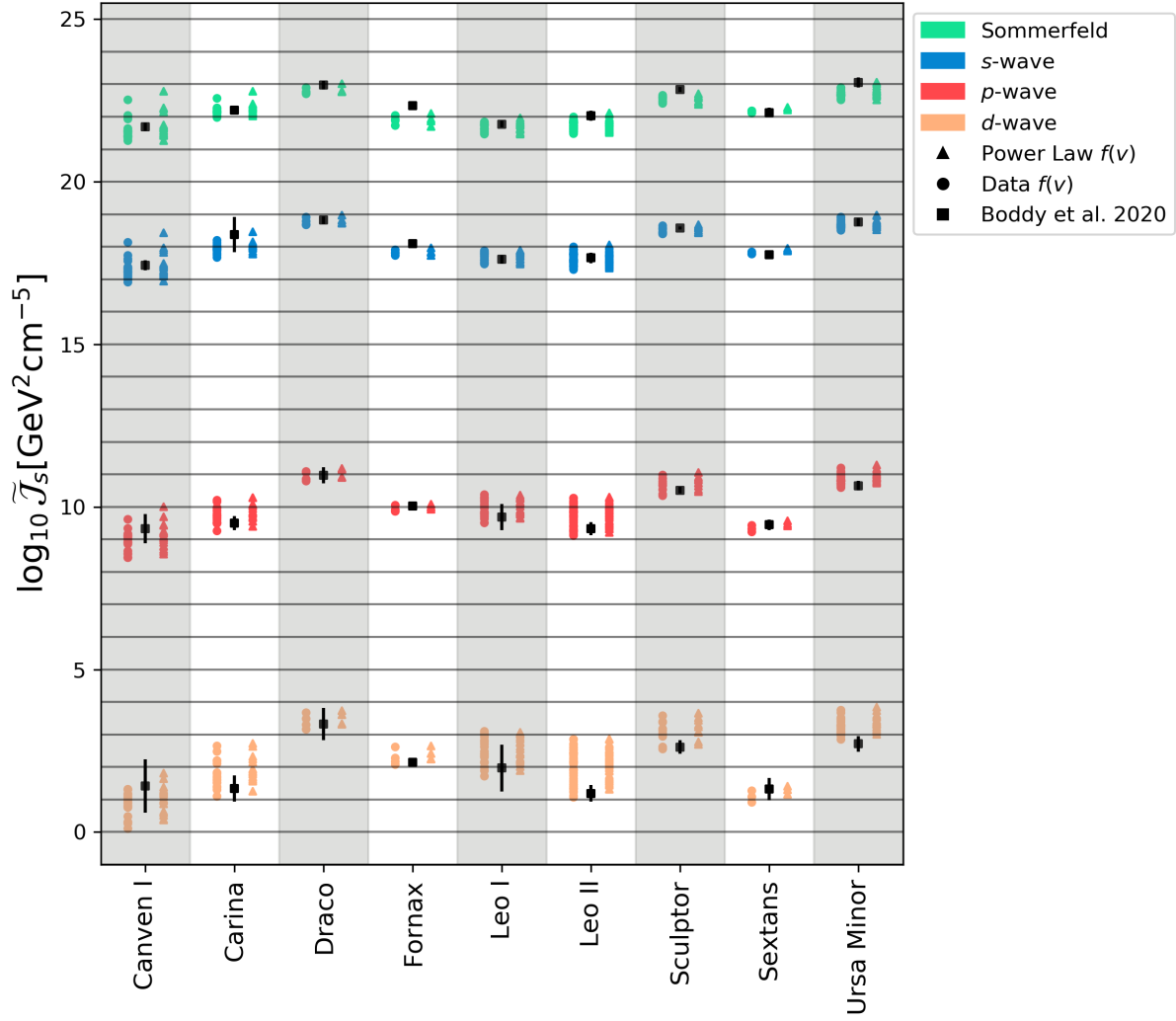

Figure C.1: Same as figure 4.7, but computed using the best fit NFW density profile for each dSph analogue instead of the Einasto density profile. Reprinted with permission from ref. [4].

APPENDIX D

GAIA QUERY

The following query was used to obtain the subset of O stars used to produce the 3D complete-ness models. The same query was used to obtain B stars by replacing ap.spectraltype_esphs = 'O' with ap.spectraltype_esphs = 'B'.

```
queryStringGaia = """SELECT g.l, g.b, g.ra, g.dec, g.parallax, g.parallax_over_error,
g.phot_g_mean_mag, g.phot_rp_mean_mag
FROM gaiadr3.gaia_source AS g
INNER JOIN gaiadr3.astrophysical_parameters AS ap
ON g.source_id = ap.source_id
WHERE (g.phot_g_mean_mag <= 20. AND ap.spectraltype_esphs = 'O'
AND g.astrometric_matched_transits >= 5 AND g.astrometric_excess_noise <= 20.
AND g.parallax_over_error >= 10.) """
```